UNIVERSITY OF
KWAZULU-NATAL

INYUVESI
YAKWAZULU-NATALI

N, N Bis (2-Pyridylmethyl)-1, 2-Ethylenediamine Tetrahydrochloride Stimulates Intrinsic Apoptosis Mediated by Oxidative and Nitrosative Stress Induction of the NF-κB/STAT3 Pathway in Human Hepatocellular Carcinoma (HepG2) Cells.

By

Nosipho Ntanzi
BSc., BMedSci. (Hons) (UKZN)

Submitted in fulfillment of the requirements for the degree of Master of Medical Science

Discipline of Medical Biochemistry
School of Laboratory Medicine and Medical Sciences
College of Health Sciences
University of Kwa-Zulu Natal

2022

DECLARATION

This dissertation contains the original work by the author and has not been submitted in any form to another university. The use of work by others has been duly acknowledged in the text. The research described in this study was carried out in the Discipline of Medical Biochemistry, School of Laboratory Medicine and Medical Science, College of Health Sciences, University of Kwa-Zulu Natal, Durban, under the supervision of Dr RB Khan, Dr HK Kumal,o and Dr L Shunmugam.

Nosipho Ntanzi

08 September 2022

Date

Signed: 

Dr RB Khan

ACKNOWLEDGEMENTS

First of all, I would like to thank God for His grace and provision. This wouldn't have been possible without Him. He has been so good and so kind. Every single need that I had, every wisdom and strength that I needed, has been graciously provided by God. May this work bring glory and praises to Him alone!

My mother, thank you for praying for me more than you pray for yourself. Thank you for your love, support, and encouragement. If it weren't for all the sacrifices that you have made for me, I would never have been able to be where I am today. I love you, and I appreciate everything that you have done for me.

Dr RB Khan, thank you for being so kind and patient with us. To be supervised by someone like you is an answer to my prayers. Thank you for your encouragement and wise advices throughout the course of this thesis.

Dr HK Kumalo, thank you for the opportunity you've given to me and the motivation to make my discoveries in the lab known to the world. Your support, guidance, and supervision is highly appreciated.

Dr L Shunmugam, thank you for your advice, corrections, suggestions and contributions to this thesis.

Miss Siphosethu Mndebele, Mr Mthokozisi Nxumalo and the rest of Masters Class of 2021/2022, I could never have asked for better colleagues to share my studies with. You have been very much supportive and dedicated to your work. In tough times we hoped for better days and encouraged each other, in good times we danced and praised God together. I'm grateful that I met you all, you made my life so easy.

Friends and family, thank you for your prayers, your encouragement and support. Thank you for always reminding me that God is sovereign and always good whenever I doubted his goodness upon my life and his sovereignty in the progress of this thesis. To all my friends, thank you for being a shoulder to cry on, thank you for always checking up on me and encouraging me. I thank God for you all and I truly appreciate your friendship.

Department of Medical Biochemistry, I would like to thank everyone in our department for their assistance, patience and support over the years.

University of KwaZulu-Natal College of Health Sciences and **National Research Foundation**, thank you for financially supporting me and providing laboratory expenses as a postgraduate student.

TABLE OF CONTENTS

LISTS OF ABBREVIATIONS

%	Percentage
8-oxoG	8-oxoguanine
µg	Microgram
µl	Microlitres
µm	Micrometre
µM	Micromolar
ADP	Adenosine diphosphate
Apaf-1	Activating factor of apoptotic protease–1
ATP	Adenosine triphosphate
Bax	Bcl-2-associated X protein
Bak	Bcl-2 homologous antagonist killer
BER	Base excision repair
BCA	Bicinchoninic acid
BCl-2	B-cell lymphoma-*2*
BH	Bcl-2 homology
BHT	Butylated hydroxytoluene
BSA	Bovine serum albumin
CA	California
$C_2H_4(NH_2)_2$	Ethylenediamine
CCM	Complete culture medium
CDK	Cyclin-dependent kinases
cDNA	Complementary DNA
CST	Cell Signalling Technology
cm	Centimetres

CO_2	Carbon dioxide
COOH	Carboxyl group
Cr	Chromium
Cu (II)	Copper
$CuSO_4$	Copper (II) sulfate
CYP2E1	Cytochrome P450 family 2 subfamily E member 1
CYP450	Cytochrome P450
dH_2O	Distilled Water
DISC	Death-inducing signaling complex
DMSO	Dimethyl sulphoxide
DNA	Deoxyribonucleic acid
DNase	Deoxyribonuclease
DNTP	Deoxynucleotide triphosphates
ds	Double-stranded
DTNB	5,5′-dithiol-bis (2-nitrobenzoic acid)
EDTA	Ethylenediamine
EMEM	Eagle's Minimum Essential Medium
ETC	Electron transport chain
ER	Endoplasmic reticulum
f-SWCNTs	Functionalized single-walled carbon nanotubes
FADD	Fas-associated protein with death domain
Fas	First apoptosis signal
FasL	Fas ligand
FC	Fold change
Fe	Iron
GAPDH	Glyceraldehyde 3-phosphate dehydrogenase

GCL	Glutamate-cysteine ligase
GPx	Glutathione peroxidase
GSSG	Glutathione disulphide
GSH	reduced Glutathione
h	Hours
H_2O_2	Hydrogen peroxide
H2pmen	N, N'-bis(2-pyridylmethyl)-ethylenediamine tetrahydrochloride
HALT-C	Hepatitis C antiviral long-term treatment against cirrhosis
HBV	Hepatitis B virus
HCC	Hepatocellular carcinoma
HCl	Hydrochloric acid
HCV	Hepatitis C virus
HDL	high-density lipoprotein
Hek293	human embryonic kidney cell line
HepG2	Hepatocellular carcinoma cell line
HRP	Horseradish peroxidase
IC_{50}	Half maximal inhibitory concentration
IL-6	Interleukin 6
Jhb	Johannesburg
IκBα	Nuclear factor of kappa light polypeptide gene enhancer in B-cells inhibitor, alpha
IKK	IκB kinase
iNOS	Inducible nitric oxide synthase
INT	Iodonitrotetrazolium
Kg	Kilograms
Keap1	Kelch-like ECH-associated protein 1
LDH	Lactate dehydrogenase

m	Meters
MCF-7	Michigan cancer foundation-*7*
MDA	Malondialdehyde
Mg^{2+}	Magnesium ion
mg	Milligram
ml	Millilitres
mRNA	Messenger RNA
MtMP	Mitochondrial membrane potential
MOMP	Mitochondrial outer membrane permeabilization
mtDNA	Mitochondrial DNA
MTT	3-(4, 5-Dimethyl-2-thiazolyl)-2, 5-diphenyl-2H-tetrazolium bromide
NAD^+	Nicotinamide adenine dinucleotide
NADH	Nicotinamide adenine dinucleotide
NADPH	Nicotinamide adenine dinucleotide phosphate hydrogen
NEDD	N-1-Naphthyl ethylenediamine dihydrochloride
NEMO	NF-$_K$B essential modulator
NF-κB	Nuclear factor kappa-light-chain-enhancer of activated B cells
NH_2	Amino group
nm	Nanometres
NO	Nitric oxide
NO_2^-	Nitrite
NO_3^-	Nitrate
NOS	Nitric oxide synthase
Nrf2	Nuclear factor erythroid 2-related factor 2
O_2^-	Superoxide radical
°C	Degrees Celsius

OD	Optical density
OGG1	8-Oxoguanine DNA Glycosylase 1
OH	Hydroxyl radical
ONOO−	Peroxynitrite
p53	Protein 53
PAR	Polymerization of ADP-ribose
PARP1	Poly (ADP-ribose) polymerase 1
PBS	Phosphate buffered saline
PCR	Polymerase chain reaction
pH	Potential hydrogen
PI	Propidium iodide
PS	Phosphatidylserine
pSTAT3	Phosphorylated STAT3
PUFAs	Polyunsaturated fatty acids
qPCR	Quantitative polymerase chain reaction
RFC	Relative fold change
RLU	Relative lights units
RBD	Relative band density
RNA	Ribonucleic acid
RNS	Reactive nitrogen species
ROS	Reactive oxygen species
RT	Room temperature
SA	South Africa
SDS	Sodium dodecyl sulphate
SOD2	Superoxide dismutase 2
ss	Single-stranded

SH	Thiol group
STAT3	Signal transducer and activator of transcription 3
SULF	Sulphanilamide
TEMED	Tetramethylethylenediamine
TBA	Thiobarbituric acid
TBARS	Thiobarbituric acid reactive substances
TNB	5′-thio-2-nitrobenzoic acid
TNF	Tumour necrosis factor
TPEN	N, N,N,N-Tetrakis (2-pyridylmethyl)-ethylenediamine
TTBS	Tween-Tris-buffered saline.
USA	United States of America
V	Voltage
VCl_3	vanadium chloride
VLDL	very-low-density lipoprotein
Zn (II)	Zinc
α	Alpha
β	Beta
γ	Gamma

LIST OF FIGURES

CHAPTER 2

CHAPTER 3

CHAPTER 4

CHAPTER 6

LISTS OF TABLES

ABSTRACT

Introduction: Hepatocellular carcinoma (HCC) is one of the leading causes of cancer-related deaths worldwide. Its incidence is rising, and this trend is expected to continue for decades. Several cancer therapeutics have already been discovered and are being used to treat HCC, however, most of them cause severe side effects which decrease the treatment's effectiveness. Metal chelators such as ethylenediaminetetraacetic acid (EDTA) have previously demonstrated anti-cancer potential. N, N-bis (2-pyridylmethyl)-ethylenediamine tetrahydrochloride (H2pmen) is a tetradentate ligand that forms stable complexes with Fe, Cr, Cu(II), and Zn (II), and it has been shown to be a potentially effective reagent for metal chelation. This study investigated the antiproliferative and cytotoxic effects of H2pmen in the HepG2 cell line.

Methods: The cell viability was determined by treating HepG2 cells with different concentrations (0–1000 μM) of H2pmen over 24h. MTT assay was used to obtain an IC_{50}, which was then used in all subsequent assays. The cells were then assayed for oxidative stress and membrane damage (TBARS, NOS, GSH, and LDH cytotoxicity), apoptotic induction (ATP assay, JC-10 assay, Annexin v, Caspases), cytochrome P450 3A4 activity (Luminometry). Protein expression of iNOS, SOD2, Bax, Caspase-2, and STAT3 were identified using western blot analysis. The gene expression of *GPx1*, *Nrf2*, *NF-κB*, *p53*, and *OGG1* was determined using qPCR.

Results: H2pmen induced a dose-dependent decrease in cell viability (IC_{50} of 209 μg/ml), a significant increase in CYP34A activity ($p \leq 0.05$ at IC_{20} and IC_{50}), a decrease in ATP production (at IC_{20} $p \leq 0.05$ and at IC_{50}), a significant decrease in $\Delta\Psi m$ ($p \leq 0.05$ at IC_{20} and at IC_{50}). The ROS-associated membrane was induced, indicated by an increase in lipid peroxidation ($p \leq 0.05$ at IC_{20} and $p \geq 0.05$ at IC_{50}), an increase in RNS production ($p \geq 0.05$ at IC_{20} and at IC_{50}), an upregulation in iNOS protein expression (at IC_{20} where $p \leq 0.05$ and at IC_{50}) and *NF-κB* gene expression (at IC_{20} where $p \leq 0.05$ and at IC_{50}). Oxidative stress occurred due to a decrease in GSH levels (at IC_{20} and $p \geq 0.05$ at IC_{50}), a significant downregulation in SOD2 protein expression, and upregulation in gene expression of *GPx-1* (at IC_{20} where $p \geq 0.05$ and at IC_{50}) and *Nrf2* (at IC_{20} and at IC_{50} where $p \leq 0.05$). H2pmen initiated caspase-dependent apoptosis that was indicated by a decrease in Caspase-2 ($p \leq 0.05$at IC_{20} and at IC_{50}), caspase-8 (at IC_{20} and $p \geq 0.05$ at IC_{50}), a slight insignificant decrease at IC_{20} and an increase at the IC_{50} in caspase-9, a significant upregulation in Bax ($p \leq 0.05$ at IC_{20} and at IC_{50}) protein expression and *p53* (at IC_{20} where $p \leq 0.05$ and at IC_{50}) gene expression. The significant increase in caspase-3/7 ($p \geq 0.05$ at IC_{20} and IC_{50}), Annexin V levels ($p \geq 0.05$ at IC_{20} and at IC_{50}), LDH ($p \geq 0.05$ at

IC_{20} and IC_{50}), STAT3 ($p \leq 0.05$at IC_{20} at IC_{50}), PARP1 ($p \leq 0.05$ at IC_{20} and at IC_{50}), and *OGG1* ($p \leq 0.05$ at IC_{20} and at IC_{50}) shows that apoptosis was executed by H2pmen in HepG2 cells.

Conclusion: H2pmen reduced cell viability of HepG2 cells, exerting a cytotoxic effect associated with decreased ΔΨm and ATP, and increased LDH leakage. The chelating properties of H2pmen was linked to the induction of oxidative and nitrosative stress that affected lipids and DNA. The HepG2 cells mounted an antioxidant defense involving *Nrf2* to counteract the depletion of SOD2 and GSH, with evidence of its effect associated with upregulation of *GPx*. The prevailing oxidative stress activated DNA repair enzymes (PARP1 and p53), while *NF-κB* and STAT3 pathways were also induced. Bax-induced MOMP and caspase-2 invoked VDAC triggered caspase-dependant apoptosis via the intrinsic pathway.

Keywords: H2pmen, HepG2 cells, cytotoxicity, oxidative stress, NF-κB, STAT3, apoptosis

CHAPTER 1: INTRODUCTION

1.1. Introduction

Cancer is the uncontrolled growth of abnormal cells anywhere in the body. Cancer arises when the body's natural control mechanism malfunctions (Hassanpour and Dehghani, 2017, Hegde and Chen, 2020). Abnormal cells can evade cell death by increasing or decreasing the expression of anti- or pro-apoptotic genes, thus leading to unregulated proliferation and dissemination throughout the body or isolated to one organ (Zhou *et al.*, 2021). These cancerous cells may accumulate to form a tumour (Hassanpour and Dehghani, 2017, Boedtkjer and Pedersen, 2020). Cancer can be classified into different categories depending on the location within the human body. Primary and secondary liver cancer are the two types of liver cancer. Primary liver cancer starts in the liver and spreads to other body parts (Petrick and McGlynn, 2019). Secondary liver cancer begins from another organ or other body parts and spreads to the liver (Emsen *et al.*, 2021). Types of primary liver cancer includes, angiosarcoma, hepatoblastoma, and carcinomas. Angiosarcoma is a rare type of liver cancer that forms in the lining of the blood vessels and lymph vessels, while hepatoblastoma is a rare tumor that originates in hepatocytes (Sun *et al* 2021). Carcinomas are the most common types of cancer and are classified as solid tumours (Beloribi-Djefaflia *et al.*, 2016, Kather *et al.*, 2018, Zhou *et al.*, 2021). Liver cancer is one of the examples of carcinoma cancer.

The liver is a vital organ that filters waste products and foreign substances from the bloodstreams, regulates blood sugar levels and produces necessary nutrients (Licata, 2016, Lada *et al*., 2020). The liver is crucial in the body for transforming and clearing xenobiotics ingested chemicals and foodstuffs, thus making it highly vulnerable to the toxicity exerted by these agents (Bischoff *et al*., 2018, Sun *et al* 2021). Many xenobiotics damage mitochondria, energy-producing intracellular organelles (Licata, 2016, Ferlay *et al*., 2021). Mitochondrial malfunction produces an excessive amount of oxidants, which may induce damage to hepatic cells (Bischoff *et al*., 2018).

Risk factors such as alcohol abuse and fat accumulation in the liver may result in cirrhosis, a form of internal scarring of the liver (Bischoff *et al*., 2018, Okeke *et al*., 2020). It usually occurs when the liver has been damaged for an extended period of time. When liver cells are damaged and die due to chronic liver infection, fibrous scar tissue can form to replace them, which often leads to liver cancer

(Kisseleva and Brenner, 2021). Liver cancer remains the fifth most common cancer in men and the eighth-most common cancer in women worldwide (Sun *et al*., 2021). In many developed countries, the incidence of primary liver cancer is rising, and this trend is expected to continue for decades (Valery *et al*., 2018). The HepG2 cells are well-differentiated HCC cell lines (Han *et al.*, 2019)

Liver cancer is generally treated by sectioning the affected parts, chemotherapy, and radiotherapy. However, the survival rates for most patients are very low due to poor prognosis caused by late diagnosis. The type of treatment a patient receives is determined by the type of cancer and its level of progression (Han *et al.*, 2019, Huang, 2021). In addition, some anti-cancer therapies such as chemotherapy and radiation are known to cause severe side effects such as nephrotoxicity, which decreases the treatment's effectiveness and impacts the patients' quality of life and survival (Santos *et al*., 2020). Therefore, there is a need to develop anti-cancer therapies, which are potently toxic to cancer but cause less or no damage in non-cancerous healthy cells of the body. There is a recent interest in researching ligands or metal-containing compounds such as cisplatin and *cis*-$[Pt^{II}(NH_3)_2Cl_2]$ as anti-cancer therapy due their toxicity and effectiveness in disease treatment (Ahmad, 2020).

There is thus, an increasing interest in the synthesis and characterization of polydentate ligands, which could be used as chelating agents in medicine (Tornesello *et al*., 2017). Recent literature has discovered that the tetradentate ligand, N, N'-bis(2-pyridylmethyl)-ethylenediamine tetrahydrochloride (H2pmen) forms stable complexes with iron [Fe], Chromium [Cr], Copper [Cu (II)] and zinc [Zn (II)]. It has been shown to be an effective reagent for metallic chelation, (Popov *et al*., 2019). H2pmen is a novel compound and therefore, the biochemical effects underlying it's mechanism of cytotoxicity on HepG2 cells has not yet been investigated. The cytotoxic effects of the metal complexes are mostly triggered by oxidative stress and they have a strong affinity for enzymes and proteins with thiol groups, which are involved in normal cellular defence mechanisms (Flora *et al.*, 2009, Patwa and Flora, 2020).

Oxidative stress represents an imbalance between the systemic expression of free radicals and the capacity of a biological system to detoxify the reactive intermediates or repair the damage resulting from them (Sies *et al*., 2017, Hayes *et al*., 2020). Free radicals can be reactive oxygen species (ROS) and reactive nitrogen species (RNS). Prominent ROS include hydrogen peroxide (H_2O_2), superoxide

(O_2^-), hydroxyl radical (OH^-) and others (Gandin *et al.*, 2018). In the presence of nitric oxide (NO), ROS gets converted to RNS that potentiate cellular damage (Gandin *et al.*, 2018). Disturbances in a cell's normal redox state that leads to increased free radicals can damage all of the cell's components including proteins, lipids and DNA (Birch-Machin and Bowman, 2016, Hayes *et al.*, 2020). If oxidative stress is uncontrolled, it can lead to lipid peroxidation and protein carbonylation (Gandin *et al.*, 2018). Nucleotide base damage and strand breaks in DNA are caused by oxidative stress from oxidative metabolism (Hayes *et al.*, 2020). According to recent research evidence, antioxidants such as reduced glutathione (GSH), superoxide dismutase 2 (SOD2) and glutathione peroxidase 1 (GPx1) can control oxidative stress by preventing the propagation or generation of free radicals (Siauciunaite *et al.,* 2019). The nuclear factor erythroid 2-related factor 2 (Nrf2) is a master antioxidant because it interacts with antioxidant response elements to stimulate the transcription of antioxidant and cytoprotective genes like SOD2 and GSH (He *et al.*, 2020). Failure of antioxidants to regulate oxidative stress can cause oxidative damage to the cells which leads to cell death if damage cannot be repaired (Hayes *et al.*, 2020).

Apoptosis can be defined as programmed cell death that occurs in multicellular organisms. Apoptosis is carried out through two main pathways: (1) intrinsic and (2) extrinsic pathways, both of which are mediated by caspases that trigger death by cleaving specific proteins in the cytoplasm and nucleus. Apoptosis has two distinct phases: initiation and execution (Su *et al.,* 2015). The initiation phase starts with various "stresses" from outside the cell or within the cell and culminates in activating the initiator caspase-8 and -9. The initiator caspases activate the process of execution by caspase-3/7 (Lopez and Tait, 2015). The execution process of apoptotic cell death includes the activation of specialized enzymes such as caspase-activated DNase and poly-ADP ribose polymerase, and others, which lead directly to cell death (Lopez and Tait, 2015). Phosphatidylserine (PS) release on the outer plasma membrane has long been thought to be a distinct characteristic of apoptotic cells (Segawa and Nagata, 2015, Naeini *et al.*, 2020). The PS exposure results to the removal of apoptotic cell by phagocytes (Naeini *et al.*, 2020).

Drugs that induce apoptosis are desirable as anti-cancer drugs. In literature, metal chelators have been shown to induce ROS-mediated apoptosis, DNA fragmentation, and a decrease in mitochondrial membrane potential (Hong *et al.*, 2015, Manikandamathavan *et al.*, 2017). To date, there is an evident lack of literature regarding the biochemical effects underlying the mechanism of H2pmen in HCC.

Therefore, the purpose of this study is to investigate the cytotoxic potential, the antiproliferative effect of H2pmen, and its effects on oxidative stress in HepG2 cells.

1.2. Problem Statement

Cancer is a major public health and economic concern, and its burden is set to spiral in the coming years. Cancer is the leading cause of death worldwide, with approximately 10 million deaths in 2020 (Ferlay *et al.*, 2021). Liver cancer remains the fifth most common cancer in men and the eighth-most common cancer in women, worldwide (Sun *et al*., 2021). In many developed countries, the incidence of primary liver cancer is rising, and this trend is expected to continue for decades (Valery *et al*., 2018). The need to develop safe and effective cancer treatment is obvious, particularly as number of people diagnosed with cancer continue to rise around the world. To date, there is no information about the biochemical effects underlying the mechanism of cytotoxicity of H2pmen on HepG2 cells.

1.3. Rationale

There are traditional and modern strategies used to fight cancer, as well as a range of treatments used to treat cancer, such as chemotherapy, radiation therapy, and surgery. However, they all have disadvantages in terms of side effects and toxicity. As the problem persists, new techniques to cancer control are required, particularly given the failure of traditional chemotherapeutic approaches. Currently, the most promising agents that can become clinically successful cancer treatments are synthetic compounds. Synthetic compounds are cheap, easily accessible alternative and they may be a viable, non-toxic treatment for HCC, however there is not enough known about them. A better understanding of the action and activity spectrum mechanisms of H2men may serve as a foundation for further investigations that could lead to clinically successful cancer treatments to curb this global threat.

1.4. Hypothesis

1.4.1 Null hypothesis

The null hypothesis of this study is that H2pmen does not have a cytotoxic and anti-proliferative effect on HepG2 cells following acute exposure of 24 hours (h).

1.4.2. Alternate hypothesis

The alternate hypothesis of this study is that H2pmen induced cytotoxic and anti-proliferative effect on HepG2 cells following acute exposure of 24 h.

1.5. Aim

This study aims to determine the potential anticancer and cytotoxic effects of H2pmen on HepG2 cells by investigating the biochemical, molecular mechanisms contributing to cell death upon acute exposure (24 h).

1.6. Objectives

The objectives of the study were to:

- Assess the viability of HepG2 cells exposed to different concentrations of H2pmen using the MTT assay and obtain an IC_{50} for subsequent assays.
- Assess if HepG2 cells metabolized H2pmen by quantifying CYP3A4 using luminometry.
- Assess mitochondrial integrity by measuring the ATP and JC-10 using luminometry.
- Establish if oxidative stress occurred by:
    - measuring the level of MDA using TBARS assay.
    - quantifying nitric oxide using the NOS assay, iNOS protein using western blot and NF-κB gene expression using PCR.
    - quantifying GSH using luminometry.
    - determining antioxidant protein expression (SOD2) using western blotting and gene expression (*GPx1* and *Nrf2*) using qPCR
    - determining the extent of oxidative DNA damage by quantifying *OGG1* using qPCR.

- Clarify if H2pmen induced cell death by:
    - detecting externalized phosphatidylserine using Annexin V assay
    - determining if apoptosis was initiated by assessing the activity of initiator caspases (Caspase-2, -8 and -9) and the protein expression of p53 and Bax.
    - detecting if apoptosis was executed by quantifying caspase-3/7, STAT3 and PARP1.
    - determining the extent of plasma membrane damage in a cell population by quantifying LDH.

CHAPTER 2: LITERATURE REVIEW

2.1. Liver

2.1.1. Structure and function

The liver is a vital organ in the human body. It weighs approximately 1.5 kilograms (kg) and accounts for about 2 percent (%) of an adult's body weight, making it the largest gland in the body (Poisson *et al*., 2017, Kisseleva and Brenner, 2021). It is found below the diaphragm on the right side of the abdominal cavity. The liver has two lobes: a larger right lobe and a smaller left lobe, divided by the falciform ligament (Figure 2.1) (Wang *et al*., 2017). The falciform ligament also helps attach the liver to the anterior abdominal wall (Wang *et al*., 2017). Glisson's capsule is a fibrous tissue layer that covers the outside of the liver (Lada *et al.*, 2020, Kisseleva and Brenner, 2021). The peritoneum, a membrane that forms the lining of the abdominal cavity, further protects this capsule (Lada *et al.*, 2020). This helps hold the liver into place and protect the liver from physical damage.

The liver is a metabolically active organ that performs various crucial life functions. The liver's primary functions are bile production, fat-soluble vitamin storage, and drug metabolism (Ozougwu, 2017, Chung, 2021). Bile is an essential fluid as it assists in the absorption and digestion of lipids by secreting bile salts and acids, which helps in the excretion of the material not excreted by the kidneys (Almazroo *et al.*, 2017). Bile is produced and released by hepatocytes into the bile canaliculi, where it passes from smaller to larger ducts before being stored in the gallbladder for storage and concentration (Ozougwu, 2017, Wen *et al.*, 2019).

Fat-soluble vitamins (vitamin A, D, and E) are stored and metabolized in the liver. Most fat-soluble vitamins reach the liver through intestinal absorption as chylomicrons or very-low-density lipoprotein (VLDL) (Ozougwu, 2017). Vitamin A is stored in Ito cells and can be converted to retinal and then retinoic acid for phototransduction (Chug, 2021). The hepatic cytochrome P450 (CYP450) system converts vitamin D3 to a 25-hydroxylated form, which is then further hydroxylated in the kidney to achieve its functional form. The liver receives Vitamin E in its alpha and gamma-tocopherol state (Jeon and Shin, 2018). While the liver metabolizes the gamma-tocopherol form for excretion, alpha-tocopherol is integrated with VLDL or high-density lipoprotein (HDL) in the liver and subsequently released back into circulation (Jeon and Shin, 2018, Wen *et al.*, 2019).

The metabolic and detoxification of xenobiotics is another essential function of the liver. Some of these substances are metabolized by lysosomes in the liver, although biotransformation is a crucial mode of metabolism and detoxification (Almazroo *et al.*, 2017).

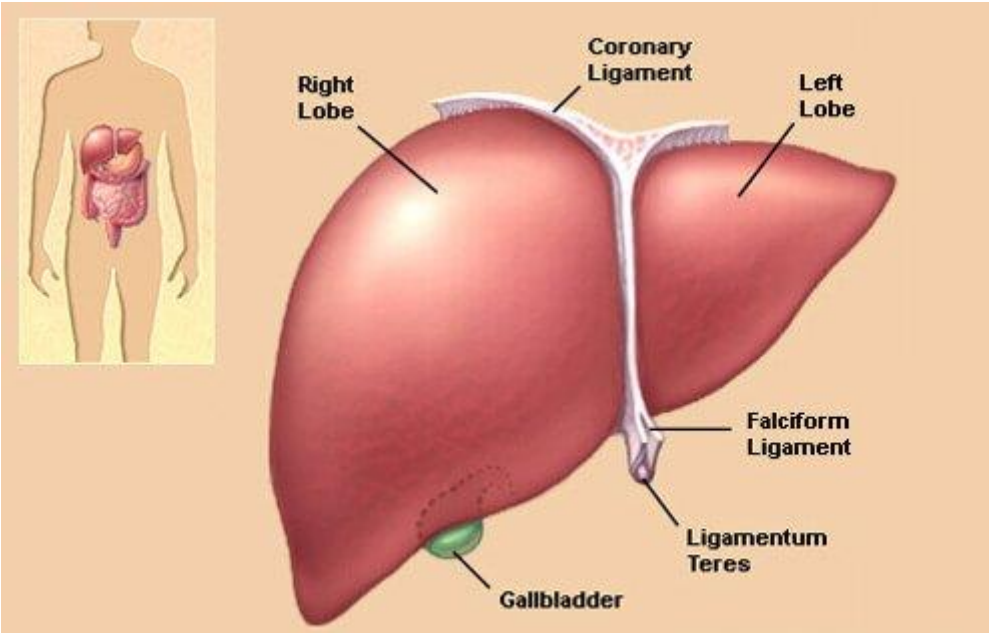

Figure 2.1: The diagram which shows the left and right lobes of the liver separated by a falciform ligament (Wang *et al*., 2017).

2.1.2. Cellular anatomy of the liver

Hepatocytes, biliary epithelial cells, stellate cells, Kupffer cells, and liver sinusoidal endothelial cells are among the cell types that make up the liver (Ozougwu, 2017, Kisseleva and Brenner, 2021). Each of these cell types is of different embryological origin and has its own set of functions that work together to control hepatic function at various levels (Poisson *et al*., 2017). Hepatocytes are the liver's primary epithelial cells. They make up most of the liver's volume and execute many of its activities (Wang *et al*., 2017). Hepatocytes play a crucial role in metabolism, detoxification, and protein synthesis (Schulze *et al*., 2019).

The CYP450 enzymes present in hepatocytes are among the most important drug-metabolizing enzymes. CYP1, CYP2, and CYP3 are recognized to play essential roles in most drug metabolism among the CYP450 isoforms (Yokoyama *et al.*, 2018, Drozdzik *et al.*, 2021). Some reactions, such

as hydroxylation, dealkylation, and oxygenation, are catalyzed by P450 enzymes (Yokoyama *et al.*, 2018). These cytochromes can also catalyze reductive reactions, which result in the inactivation of P450 due to the metabolite generated (Chug, 2021).

The hepatocyte's role as a secretory workhorse is highlighted by the presence of a large endoplasmic reticulum (ER) and Golgi network (Schulze *et al.*, 2019, Drozdzik *et al.*, 2021). Proteins intended for secretion in the hepatocyte begin with ribosomal synthesis and transport of nascent polypeptides into the ER lumen via the Sec61 translocon before being vesicularly trafficked to the Golgi apparatus (Moremen *et al.*, 2012, Schulze *et al.*, 2019). Hepatocytes secrete several proteins into circulation, including fetoprotein, albumin, transferrin, plasminogen, fibrinogen, and clotting factors (Rapoport *et al.*, 2017). Serum albumin, produced only by hepatocytes, is any cell's most highly released protein. Proteins are packaged in secretory vesicles in the Golgi to facilitate transport to the basolateral membrane for exocytosis (Schulze *et al.*, 2019).

Hepatocytes have cords structured into hexagonal lobules constructed around a central vein to allow filtered and modified blood to drain into the hepatic vein and eventually into the inferior vena cava (Schulze *et al*., 2019). This arrangement guarantees that hepatocytes are among the first cells to be exposed to everything that is orally ingested and, after that, absorbed through the digestive system, whether it is healthy or harmful (Ozougwu, 2017). The liver receives 75% of its blood directly from the gastrointestinal tract and the spleen through portal veins, which transport drugs and xenobiotics in near-undiluted form (Licata, 2016, Song *et al*., 2019). Thus, rendering the liver highly susceptible to damage exerted by toxic drugs and other substances due to this unique metabolism and close interaction with the gastrointestinal tract (Ortega-Alonso and Andrade, 2018).

2.1.3. Xenobiotic Metabolism

Xenobiotics are chemicals that an organism is exposed to that are not part of its regular metabolism such as drugs like antibiotics and analgesic drugs (Bissig *et al.*, 2018, Watt *et al.*, 2019). Xenobiotic metabolism refers to the metabolic pathways that alter the chemical structure of xenobiotics (Hansen and Shane, 2019). Many xenobiotics might reach toxic concentrations if not broken down through proper cellular metabolism (Bissig *et al.*, 2018, Tamai *et al.*, 2021). The majority of metabolic activity within the cell needs energy, cofactors, and enzymes (Song *et al*., 2021).

Metabolism, also called biotransformation, is usually accomplished through a succession of CYP450-dependent enzymatic processes. A CYP450 system is a group of isozymes that use oxidation, reduction, or hydrolysis processes to metabolize drugs (Hansen and Shane, 2019). Although the liver is the site of most of these reactions, CYP450 isozymes have been found in other tissues such as the kidney, skin, lungs, and gastrointestinal tract (Almazroo *et al*., 2017). The CYP3A enzyme subfamily, which includes the isoforms CYP3A7, CYP3A5, and CYP3A4, is the most widely expressed CYP in the liver (Pasanen *et al.*, 1995, Shunmugam, 2016). CYP3A4 is the most abundantly expressed CYP in the liver and small intestine, making 50% of all CYP total content and playing a vital role in the metabolism of xenobiotics and drugs (Shunmugam, 2016, Tamai *et al.*, 2021).

Biotransformation can be divided into two phases, each of which aids in eliminating the drug from the body. Phase I enzymes make xenobiotics more polar and give rise to sites for conjugation processes and are frequently the first to metabolize lipophilic xenobiotics (Stanley, 2017). Several enzymes function in phase I to add reactive and polar groups into their substrates (Schlichting *et al.*, 2000, Hansen and Shane, 2019). The hydroxylation catalyzed by the CYP450-dependent mixed-function oxidase system is one of the most prevalent modifications (Akagah *et al.*, 2008, Almazroo *et al.*, 2017). These enzyme complexes function by introducing an atom of oxygen into nonactivated hydrocarbons, resulting in the formation of hydroxyl groups or the N-, O-, and S-dealkylation of substrates [Figure 2.2] (Schlichting *et al.*, 2000, Harlow *et al.*, 2018). The P450 oxidases' reaction mechanism involves the reduction of cytochrome-bound oxygen and the formation of a highly reactive oxyferryl species (Almazroo *et al.*, 2017). Oxidation, reduction, hydrolysis, cyclization, decyclization, and addition of oxygen or removal of hydrogen are all examples of phase I reactions carried out by mixed-function oxidases (Akagah *et al.*, 2008, Hansen and Shane, 2019). A CYP450 monooxygenase, Nicotinamide adenine dinucleotide phosphate hydrogen (NADPH), and oxygen are usually involved in these oxidative reactions (Figure 2.2) (Stanley, 2017).

$$\mathbf{O_2 + NADPH + H^+ + RH \rightarrow NADP^+ + H_2O + ROH}$$

Figure 2.2: Chemical reaction catalyzed by CYP450. O_2, RH, nicotinamide adenine dinucleotide phosphate ($NADP^+$), R-OH represents oxidant, the xenobiotic compound, reducing agent, and oxidized xenobiotic metabolite, respectively (Carloson *et al*., 2019).

When the metabolites from phase I reactions are sufficiently polar, they may be eliminated easily at this stage (Hansen and Shane, 2019). Many phase I products are not readily excreted. They are subjected to a phase II reaction in which an endogenous substrate reacts with the newly introduced functional group to generate a highly polar conjugate (Akagah *et al.*, 2008, Stanley, 2017). In subsequent phase II reactions, the activated xenobiotic metabolites are conjugated with charged species like glutathione (GSH), sulfate, and glycine (Almazroo *et al.*, 2017). Carboxyl (-COOH), hydroxyl (-OH), amino (NH2), and thiol (-SH) groups are all sites on drugs where conjugation reactions take place (Akagah *et al.*, 2008, Stanley, 2017). In contrast to Phase I reactions, which commonly generate active metabolites, conjugation reaction products have a higher molecular weight and are less active than their substrates (Akagah *et al.*, 2008, Harlow *et al.*, 2018). Large anionic groups detoxify reactive electrophiles and form more polar metabolites that cannot penetrate membranes and must be actively transported.

Several pathways are involved in either causing or exacerbating the hepatic injury. Many chemicals damage mitochondria, energy-producing intracellular organelles (Wedde *et al.*, 2019). Their malfunction produces an excessive amount of oxidants, damaging hepatic cells (Wedde *et al.*, 2019). Oxidative stress is also caused by the activation of certain enzymes in the cytochrome P450 system, such as CYP2E1 (Ortega-Alonso and Andrade, 2018). When hepatocytes and bile duct cells are injured, bile acid builds up within the liver (Bischoff *et al.*, 2018). This accelerates the damage exerted upon the liver.

Cirrhosis, the final stage of all chronic liver diseases, is not only a significant risk factor for the development of HCC, but it is also a limiting factor for anticancer therapy for both liver and non-hepatic cancers

2.2. Liver cancer

2.2.1. Cancer

The human body is made up of fundamental units called cells. As the body requires new cells, cells divide and grow (Hassanpour and Dehghani, 2017, Zheng *et al.*, 2019). Cells usually die when they become too old or damaged to work properly. Then, in their place, new cells arise (Zheng *et al.*, 2019). Cancer develops, and uncontrollable cell growth begins when this orderly process is interrupted by genetic changes, excessive alcohol, poor diet, occupational hazard, environmental and viral infections (Chuang *et al.*, 2015, VoPham, 2019) (Chuang *et al.*, 2015, VoPham, 2019).

Cancer can be classified into different categories depending on where it begins. Carcinomas can occur at various body sites, such as the skin or tissue surrounding the surface of the internal organs (Mattiuzzi and Lippi, 2019). Carcinomas are the most common types of cancer and usually form solid tumors (Beloribi-Djefaflia *et al*., 2016, McGlynn *et al*., 2021). Hepatocellular carcinoma (HCC) is considered the most frequently diagnosed form of carcinoma, worldwide (Li and Wang, 2016, McGlynn *et al*., 2021).

Primary and secondary liver cancer are the two types of liver cancer. Primary liver cancer starts in the liver and spreads to other body parts (Petrick and McGlynn, 2019). Secondary liver cancer begins from another organ or other body parts and spreads to the liver (Emsen *et al.*, 2021). The majority of liver cancers are secondary or metastatic, primarily due to the high incidence of hepatitis caused by infectious viruses and puts a person at risk for liver cancer (Calderaro *et al*., 2019). Cholangiocarcinoma, angiosarcoma, hepatoblastoma, and HCC are all kinds of primary liver cancer that begin from different liver cells (Petrick and McGlynn, 2019).

2.2.3. Hepatocellular carcinoma

Since the liver comprises a range of cell types, it may develop several kinds of tumours (Calderaro *et al*., 2019). These tumours are caused by a number of factors and are treated in various ways. The diagnosis for health or recovery depends on the type of tumour (Valery *et al*., 2018). Tumours are formed as old or damaged cells form a mass; a tumour may be malignant or benign (Rizvi *et al.*, 2020). A malignant tumour can develop and spread across the body, but a benign tumour does not spread as they are deemed non-cancerous (Rizvi *et al*., 2020).

To date, HCC remains the fifth most common cancer in men and the eighth-most common cancer in women around the world [Figure 2.3] (Huang *et al.*, 2021). In many developed countries, the incidence of primary liver cancer is rising, and this trend is expected to continue for decades to come (Valery *et al*., 2018). Men are three times more likely than women to be diagnosed with HCC, with around 28,000 people diagnosed each year in South Africa [Figure 2.3] (Huang *et al.*, 2021). The HCC is the most prominent type of primary liver cancer and the most significant cause of cancer-related death, globally (Valery *et al*., 2018, Groopman *et al*., 2021).

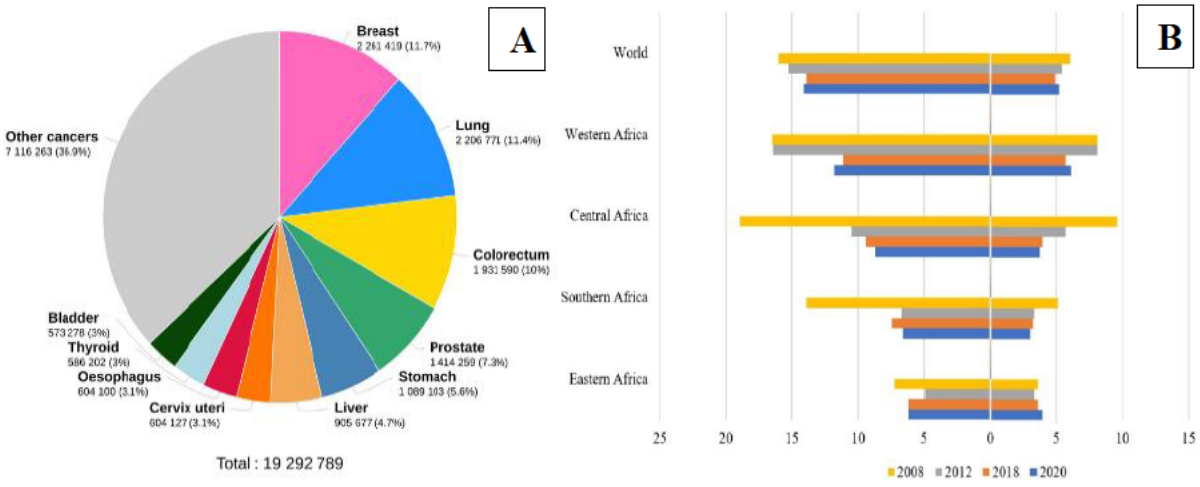

Figure 2.3: (**A**)The incidence of liver cancer worldwide compared to other types of cancer for both sexes. (**B**) The incidence of liver cancer in Africa compared to the world (Sharma, 2020).

2.2.2.1. HCC Risk factors

The most prominent risk factors for the development of HCC are chronic liver disease and cirrhosis, with viral hepatitis and excessive alcohol consumption being the primary risk factors, worldwide (Petrick and McGlynn, 2019). Cirrhosis and HCC can develop as a result of chronic viral hepatitis. The most frequent causes of chronic hepatitis worldwide are hepatitis B and C (Yim and Lok, 2006, Seto *et al.*, 2018). The hepatitis B virus (HBV) is a circular, double-stranded DNA molecule that has eight genotypes (A to H) (McMahon, 2009, Kulik and El-Serag, 2019). Infected blood transfusions, intravenous injections, and sexual contact are all possible ways hepatitis B can be transmitted (Yim and Lok, 2006, Kulik and El-Serag, 2019). The HBV infection is transmitted vertically from mother to fetus in most cases. Carriers of hepatitis B have a 10–25% lifetime chance of getting HCC (McMahon, 2009, Seto *et al.*, 2018). The HBV is unique among chronic hepatitis causes in that HCC can develop without symptoms of cirrhosis (Seto *et al.*, 2018). The hepatitis C virus (HCV) is a single-stranded RNA virus with a lot of genetic diversity (Kulik and El-Serag, 2019). The HCC develops mainly in the liver with developed cirrhosis in hepatitis C patients; however, in the hepatitis C antiviral long-term treatment against cirrhosis (HALT-C) trial, 8% of HCC occurred in individuals with only severe fibrosis (Balogh *et al.*, 2016).

Cirrhosis is the histological development of regenerating nodules surrounded by fibrous bands due to chronic liver disease. The replacement of wounded tissue by a collagenous scar is referred to as fibrosis (Bellentani *et al.*, 1997, Mohammed *et al.*, 2018). The normal wound healing response is perpetuated in the liver, resulting in an excessive prolongation of fibrogenesis damage, which leads to portal hypertension and end-stage liver disease (Farrell and Larter, 2006). Fibrosis advances at

different rates depending on the cause of the liver disease and environmental and host factors. Cirrhosis is a more advanced stage of liver fibrosis accompanied by hepatic vascular distortion (Bellentani *et al.*, 1997, Tapper and Parikh, 2018). The portal and arterial blood supplies are pushed directly into the hepatic outflow, impairing the exchange between the hepatic sinusoids and the neighbouring liver parenchyma (Mohammed *et al*., 2018).

Cirrhosis, the final stage of all chronic liver diseases, is not only a significant risk factor for the development of HCC, but it is also a limiting factor for anticancer therapy for both liver and non-hepatic cancers (Pinter *et al.*, 2016, Mitra *et al.*, 2020). Cirrhosis can limit surgical and interventional cancer treatments, alter anticancer medication pharmacokinetics, enhance chemotherapy side effects, make patients more prone to hepatotoxicity, and eventually result in a higher risk of morbidity and mortality (Durand and Valla, 2008, Pinter *et al.*, 2016, Lleo *et al.*, 2019).

2.2.2.2. HCC Cell Line

The HepG2 cell line is a human liver cancer cell line obtained from a 15-year-old Caucasian male with well-differentiated HCC (Santos *et al*., 2016). Cell lines are known for their longer lifespan, stable phenotype, high availability, and ease of use (Mersch-Sundermann *et al.*, 2004, Štampar *et al.*, 2020). However, compared to hepatocytes, they have a significant limitation in the expression of some metabolic functions (Es-haghi *et al.*, 2019). The HepG2 cells have been successfully grown in large-scale cultivation systems and are an excellent *in vitro* model for studying polarized human hepatocytes (Santos *et al*., 2016). HepG2 cells are non-tumorigenic cells with a rapid proliferation rate and an epithelial-like morphology that perform a wide range of differentiated hepatic activities (Mersch-Sundermann *et al.*, 2004, Es-haghi *et al.*, 2019). They are most widely utilized in drug metabolism and hepatotoxicity experiments.

2.3. Cancer treatments

There are a variety of cancer treatments available. The type of cancer and its stage of progression decide the type of treatment given to a patient (Miller *et al*., 2016, Rig *et al*., 2021). Some cancer patients may successfully respond to one treatment. However, the majority require a regime of treatments, such as surgery combined with chemotherapy and/or radiation therapy, to efficiently eliminate the cancerous cells (Reig *et al.*, 2021).

2.3.1. Surgery

Surgery is a procedure in which a surgeon removes cancerous portions of tissues or whole organs from the body (Anwanwan *et al.*, 2020). Surgical procedures come in various forms, and the types vary depending on the surgery's intent, the body part that requires surgery, and the extent of tissue that needs to be removed (O'Donnell *et al*., 2019). Surgery works best for solid tumours that are contained in one area (Reig *et al.*, 2021). It is a local treatment, which means it only treats the cancerous region of the body and is not used to treat cancers that have metastasized (Anwanwan *et al.*, 2020).

2.3.2. Radiation therapy

Radiation therapy is a cancer treatment that involves administering large doses of radiation to cancer cells to destroy them and shrink tumours (Chen and Kuo, 2017, Geschwind and Nezami, 2020). Radiation therapy kills cancer cells or delays their development by destroying DNA at high doses (Graham and Unger, 2018). Cancer cells that have DNA damage deemed beyond repair will either avoid dividing or die, and when damaged cells die, the body breaks them down to eliminate them (Geschwind and Nezami, 2020). Radiation therapy does not instantly destroy cancer cells. It takes days or weeks of therapy before the cancer cell DNA is weakened enough to induce cell death (Geschwind and Nezami, 2020). Following several radiation therapy sessions, the cancer cells will begin to die, and this may last for weeks or months after radiation therapy concedes (Care, 2019).

2.3.3. Chemotherapy

Chemotherapy is a treatment in which potently toxic synthetic drugs are used to destroy cancer cells. Chemotherapy may also be used to reduce the size of tumours, reduce the risk of it returning, delay or avoid its progression (Anwanwan *et al.*, 2020). Chemotherapy, when paired with other therapies, may reduce a tumour before surgery or radiation therapy, remove cancer cells that may survive after surgery or radiation therapy, increase the efficacy of other treatments, and kill cancer cells that have returned or extended to other areas of the body (Dickens and Ahmed, 2018).

However, the body is made up of various cells, including healthy cells that grow at a rapid rate (Pearce *et al.*, 2017, Anwanwan *et al.*, 2020). Chemotherapy treatments cannot distinguish between cancerous and healthy cells (Love *et al.*, 1989, Carelle *et al.*, 2002, Liu *et al.*, 2021). As a result, it affects or kills both healthy and malignant cells. Chemotherapy's influence on healthy cells is responsible for

several common adverse effects, including anemia, a reduced immune system, hair loss, and nausea (Love *et al.,* 1989, Pearce *et al.,* 2017). These side effects can influence treatment continuation and have a detrimental impact on a patient's quality of life (Liu *et al.*, 2021).

There is an urgent need to identify an alternative approach to anti-cancer therapeutics for these reasons. Over the years, scientists have focused on inorganic compounds as a potential anti-cancer agent due to toxicity and effectiveness in disease treatment (Gandin *et al.*, 2018).

2.4. N, N'-Bis (2-Pyridylmethyl)-1, 2-Ethylenediamine Tetrahydrochloride

The functional groups that comprise H2pmen and contribute to its effects include ethylenediamine, pyridyl and methyl groups. Ethylenediamine is the chelating moiety, while the HCl molecules are added to make it a salt.

2.4.1. Ethylenediamine

Ethylenediamine is an organic molecule with the formula $C_2H_4(NH_2)_2$ (Huang *et al.*, 2018). It is a common chemical building block that easily combines with moisture in humid air to produce a corrosive, poisonous, and irritating mist to which even short-term exposure can cause significant health problems (Huang *et al.*, 2018). The two nitrogen atoms donate their lone pairs of electrons when ethylenediamine serves as a ligand, making it a well-known bidentate chelating ligand for coordination compounds (Gusev *et al*., 2019). The chelating agent- EDTA, derived from ethylenediamine by a Strecker synthesis, is one of the most well-known ethylenediamine derivatives (Gusev *et al*., 2019). Recent studies of a gene delivery concept based on ethylenediamine-functionalized single-walled carbon nanotubes (f-SWCNTs) that use the oncogene suppressor p53 gene as a model gene in Michigan cancer foundation-7 (MCF-7) breast cancer cells showed that nearly 40% of cells underwent cell death following 72 h of treatment with f-SWCNTs-p53 compared to the untreated MCF-7 cells. Thereby indicating that f-SWCNTs are cytotoxic against MCF-7 cells (Jurisevic *et al.*, 2018).

2.4.2. Tetrahydrochloride

Tetrahydrochloride is any compound with four hydrochloride groups (Puchkov *et al*., 2018). The reaction between hydrochloric acid and an organic base gives rise to hydrochloride, an acid salt (Ghosh *et al*., 2012, Wood *et al*., 2017). Several medications require the addition of salt in order to

be absorbed into the bloodstream. Salts can sometimes improve the stability of medicine, allowing it to last longer. Salts make up more than half of all pharmaceuticals. The most often used salt is hydrochloride, which is present in 15.5% of all drugs (Wood *et al.*, 2017). Previous studies indicate that erlotinib hydrochloride, a targeted anticancer drug that inhibits the activity of the epidermal growth factor receptor has been approved for the treatment of advanced non-small-cell lung cancer in patients who have failed at least one previous chemotherapy regimen (Lv *et al*., 2012, Yalcin *et al*., 2020).

2.4.3. H2pmen

The H2pmen is a tetradentate ligand (Figure 2.4) that has been recently discovered to form stable complexes with Fe, Cr, Cu(II), and Zn (II) and has been shown to be potentially effective metallic chelation reagent (Popov *et al*., 2019). Over the years, chelating drugs and chelator metal complexes have been used to treat cancer. Inhibiting the molecular mechanisms that keep cancer cells active and able to metastasize is a promising approach in discovering anticancer therapies (Kontoghiorghes and Kontoghiorghe, 2020). Metals like Cu and Fe have received much attention since they are at the root of cancer cell proliferation and metastasis (Yu *et al*., 2012, Gaur *et al*., 2018).

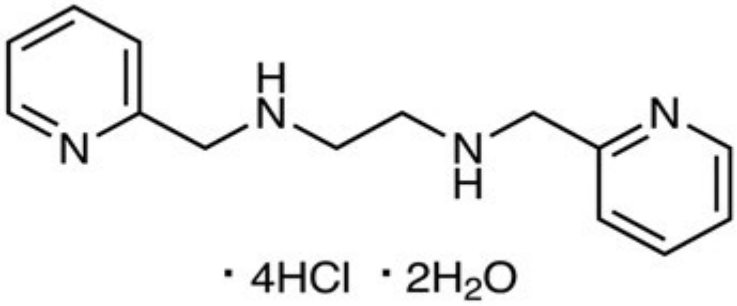

Figure 2.4: Two-dimensional chemical structure of H2pmen (National Centre for Biotechnology Information, 2021).

The chelators of interest act through various mechanisms, including binding metals extracellularly, depleting metal ions from cancer cells or intracellular sites that control cell function and inhibiting rather than eliminating molecular pathways (Gaur *et al*., 2018). Anticancer treatments with Cu, Zn, and Fe chelators are exceedingly promising, with several currently undergoing anticancer clinical human trials (Mevada *et al*., 2014, Gaur *et al*., 2018). Although several experimental chelators have been found to be effective as anticancer treatments, only a few have progressed to clinical application

(Kontoghiorghes and Kontoghiorghe, 2020). The cytotoxic effects of these metal complexes are mostly triggered by oxidative stress and they have a strong affinity for enzymes and proteins with thiol groups, which are involved in normal cellular defence mechanisms (Flora *et al.*, 2009, Patwa and Flora, 2020).

2.5. Oxidative Stress

2.5.1. Free radicals and antioxidants

Oxidative stress is an imbalance in the body of free radicals and antioxidants (Figure 2.5), which causes damage to cells and tissues (Forman and Zhang, 2021). The body's cells generate free radicals such as OH^-, O_2^- and NO across biochemical processes (Hayes *et al.*, 2020). Cells also produce antioxidants like GSH, *GPx1*, and SOD2 that neutralize those free radicals. Antioxidants are substances that, by donating an electron, neutralize or remove free radicals. Under normal physiological conditions, the body can maintain an equilibrium between antioxidants and free radicals (Gandin *et al.*, 2018). This is necessary for proper physiological functions. When the body's ability to regulate free radicals is overwhelmed, the result is oxidative stress (Forman and Zhang, 2021).

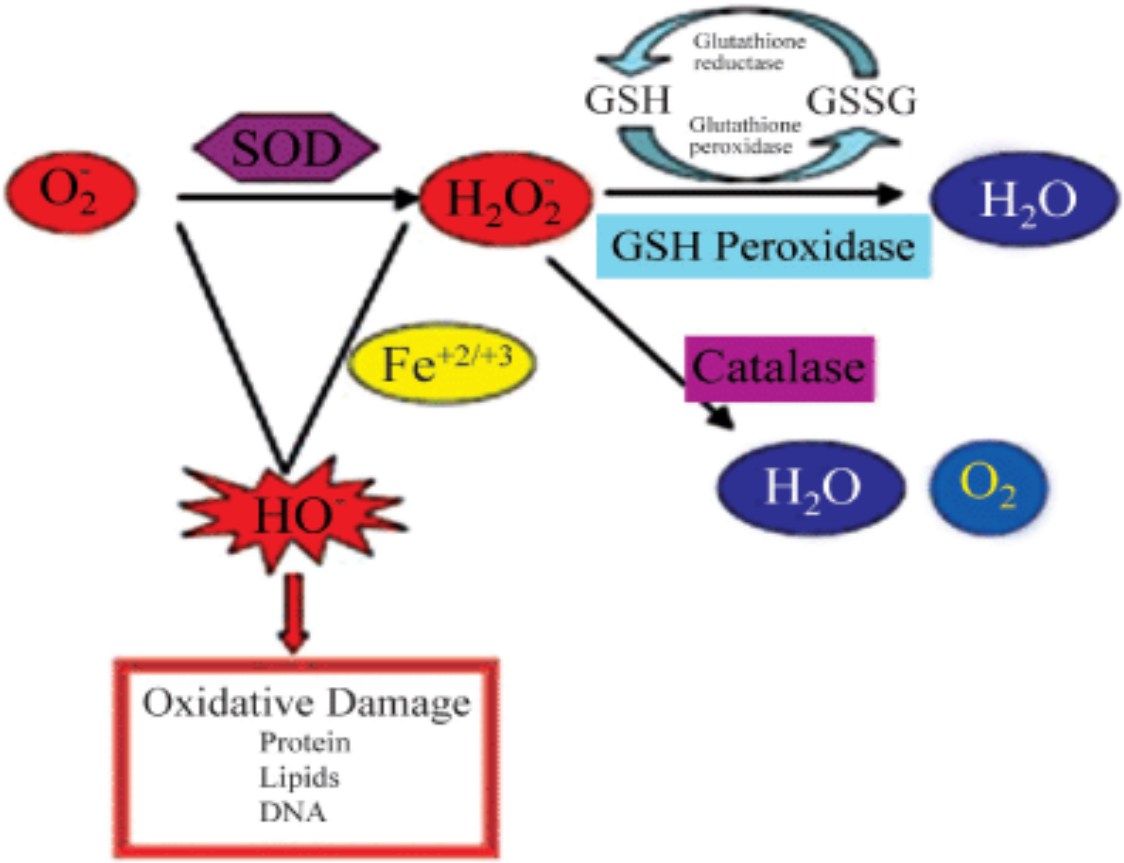

Figure 2.5: The SOD2 converts this harmful substance [oxygen ion (O_2^-)] to $H_2O_2^-$, which antioxidant enzymes like catalase can then detoxify into water. When there's low production of antioxidants, O_2^- and $H_2O_2^-$ are converted to HO^- through Fenton reaction, thus causing oxidative stress (Li *et al.*, 2015).

Disturbances in a cell's normal redox state can lead to the formation of peroxides and free radicals, which can damage all of the cell's components, including proteins, lipids, and DNA (Birch-Machin and Bowman, 2016, Hayes *et al*., 2020). Base damage and strand breaks in DNA are caused by oxidative stress from oxidative metabolism (Hayes *et al*., 2020). The ROS such as O_2^{-}, OH^{-}, and H_2O_2 cause base damage in most cases and in presence of NO they gets converted to RNS that potentiate cellular damage (Birch-Machin and Bowman, 2018).

The body requires free radicals because they are crucial signalling molecules. The problem arises when they are present in high concentrations as they can oxidize cellular molecules, including lipids, protein, and DNA. In proteins, they form protein carbonyl; in DNA, they target guanine and form oxo-guanine that must be detoxified by the enzymatic and DNA replication mechanisms; and in lipids they form lipid peroxidation (Forman and Zhang, 2021). Oxidative stress may cause chronic inflammation. Excess ROS can either oxidize biomolecules or change the structure of genes and proteins, triggering signalling cascades that can contribute to inflammatory disease initiation and progression (Speer *et al.*, 2020). Inflammation begins when ROS activate transcription factors and pro-inflammatory genes (Speer *et al.*, 2020). Infections and injuries stimulate an immune response. When fighting off invading germs, immune cells called macrophages create free radicals such as NO that can cause inflammation by damaging healthy cells (Murata, 2018).

2.6. Inflammation

Inflammation is a defensive reaction involving immune cells, blood vessels, and molecular mediators that occurs when body tissues are exposed to harmful stimuli such as pathogens, toxic compounds, damaged cells, or irritants such as germs (Chatterjee, 2016, Antonelli and Kushner, 2017). The aim of inflammation is to clear out necrotic cells and tissues weakened by the original injury and the inflammatory process and begin tissue repair (Munn, 2017, Davidson *et al*., 2021).

2.6.1. Nuclear factor kappa-light-chain-enhancer of activated B cells (NF-$_K$B)

The NF-$_K$B is a family of inducible transcription factors that regulate many genes involved in immunological and inflammatory response pathways (Ji *et al*., 2019). The NF-$_K$B1 (also known as p50), NF-$_K$B2 (also known as p52), RelA (also known as p65), RelB, and c-Rel are the five proteins that make up the NF-$_K$B family. Activation of NF-$_k$B involves two major signalling pathways: (1) the

canonical and (2) non-canonical pathways (Figure 2.6), which, despite their differences in signalling mechanisms, are both critical for controlling immunological and inflammatory responses (Sun, 2017, Ji e*t al*., 2019).

2.6.1.1. Canonical pathway

The inducible degradation of nuclear factor of kappa light polypeptide gene enhancer in B-cells inhibitor, alpha ($I_KB\alpha$), driven by its site-specific phosphorylation by a multi-subunit I_KB kinase (IKK) complex, is the central mechanism for canonical NF-$_K$B activation (Figure 2.6) (Chen *et al*., 2018). The IKK complex comprises two catalytic subunits, IKKα and IKKβ, and NF-KB essential modulator (NEMO) or IKK gamma (y), a regulatory subunit. Various stimuli, such as cytokines, growth factors, mitogens, microbial components, and stress agents, can activate IKK (Davidson *et al.*, 2021). When IKK is activated, it phosphorylates $I_KB\alpha$ at two N-terminal serine residues, triggering ubiquitin-dependent $I_KB\alpha$ degradation in the proteasome and causing rapid and transient nuclear translocation of canonical NF-$_K$B members, primarily the p50/RelA and p50/c-Rel dimers (Ji *et al*., 2019).

2.6.1.2. Non-canonical pathway

The non-canonical NF-$_K$B pathway reacts to a specific set of stimuli, including ligands from a subset of the tumour necrosis factor receptor (TNFR) superfamily (Greten and Grivennikov, 2019). The non-canonical NF-$_K$B activation relies on processing the NF-$_K$B2 precursor protein, p100, rather than $I_KB\alpha$ degradation (Figure 2.6) (Ji *et al*., 2019). The NF-$_K$B-inducing kinase (NIK) is an essential signalling protein in this pathway, activating and functionally cooperating with IKK to induce p100 phosphorylation, which leads to the protein's ubiquitination and processing (Greten and Grivennikov, 2019). The processing of p100 results in the formation of mature NF-$_K$B2 and nuclear translocation of the non-canonical NF-$_K$B complex p52/RelB by degrading its C-terminal I_KB-like structure (Sun, 2017).

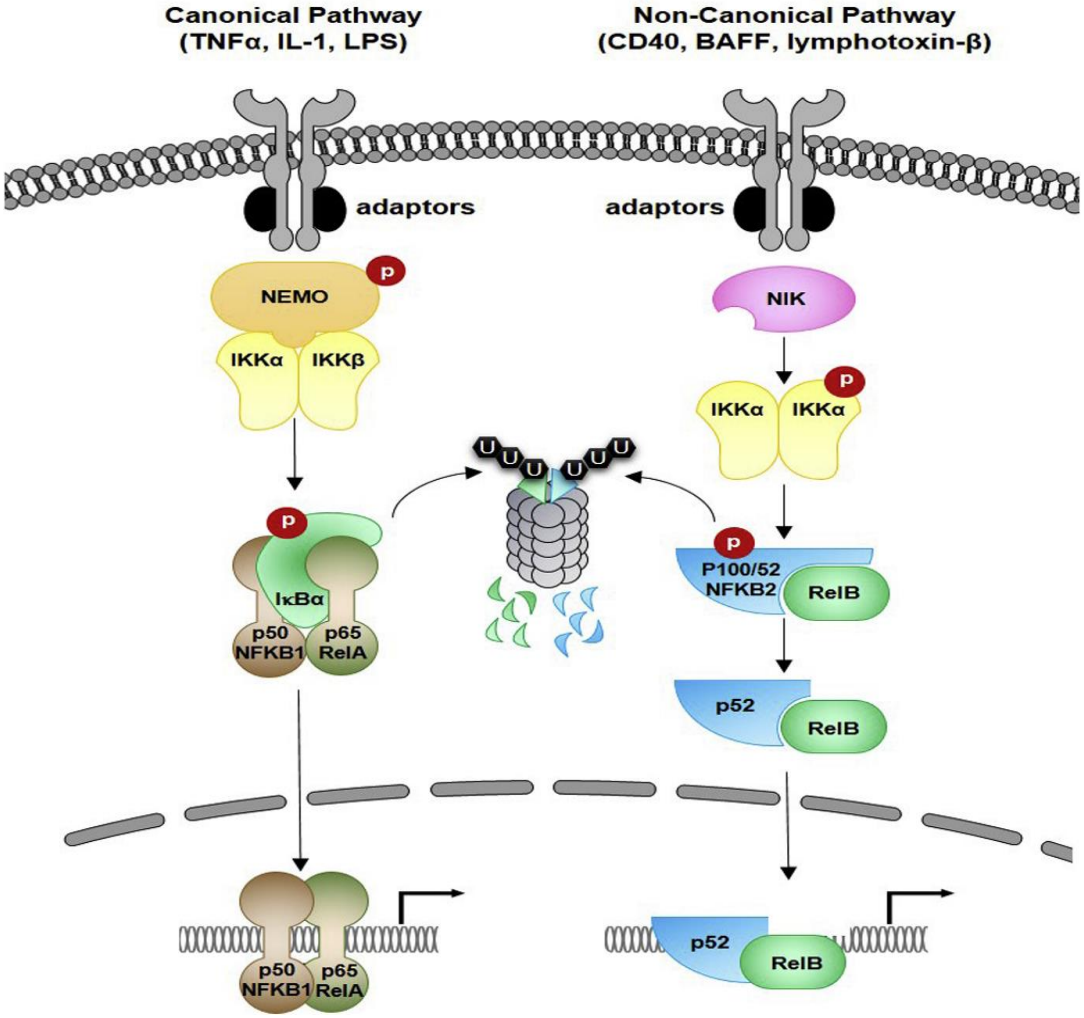

Figure 2.6: The canonical and non-canonical pathway of inflammation (Ji *et al*., 2019).

2.6.2. Inflammation and cancer

Recent research has confirmed that inflammation is essential in tumour growth (Chatterjee, 2016). Infection, chronic irritation and inflammation are all factors that contribute to the development of cancer (Chatterjee, 2016, Davidson *et al*., 2021). Although it is now evident that cell proliferation does not cause cancer in and of itself, prolonged cell proliferation in an environment rich in inflammatory cells, growth factors, active stroma (non-cancer cell and non-immune cell components of tumour), and DNA-damage-promoting chemicals undoubtedly amplifies and/or promotes the risk of cancer development (Hussain *et al.*, 2016). The tumour microenvironment, predominantly regulated by inflammatory cells such as neutrophils and lymphocytes, is now recognized as an essential participant in the carcinogenic process, supporting proliferation, survival, and migration (Greten and Grivennikov, 2019). Tumour cells have also appropriated some of the innate immune system's signalling molecules, such as selectins, chemokines, and receptors, for invasion, migration, and metastasis (Greten and Grivennikov, 2019). These discoveries pave the way to developing new

anti-inflammatory therapeutic approaches aimed against cancer development. Apoptosis is the most prevalent type of cell death used to eliminate cells that have been genetically modified and are thus potentially dangerous to the body (Zhou *et al.*, 2019). Apoptosis is necessary for normal tissue formation and maintenance, and its dysregulation is linked to various diseases (Kang *et al.*, 2019). Delayed apoptosis of inflammatory cells leads to their build-up in inflammatory reactions, which is necessary for efficient pathogen elimination (Kang *et al.*, 2019). Apoptosis is a multi-pathway process with a complicated mechanism (Wong, 2011, Carneiro and El-Deiry, 2020). Defects in these pathways can develop at any stage, resulting in malignant transformation of the damaged cells, tumour spread, and anticancer drug resistance (Carneiro and El-Deiry, 2020). However, apoptosis plays a crucial role in cancer treatment as it is a prominent target of many therapeutic approaches.

2.7. Apoptosis

Apoptosis, also known as programmed cell death, occurs in multicellular organisms such as plants, animals, and fungi (Naeini *et al.*, 2020). Apoptosis is a physiological and homeostatic mechanism that maintains cellular components in tissues and occurs naturally during development and aging (Meier *et al.*, 2000, Jan, 2019). Apoptosis is also a defense mechanism that occurs in immune reactions and when cells are harmed by disease or toxic substances (Lowe and Lin, 2000, Pfeffer and Singh, 2018). Apoptosis initiation is strictly controlled by activation pathways at the gene level, allowing damaged cells to be removed precisely and efficiently (Naeini *et al.*, 2020). The intrinsic pathway, also known as the mitochondrial pathway and the extrinsic pathway, are the two most well-known activation pathways of apoptosis (Figure 2.7) (Su *et al*., 2015, Pfeffer and Singh, 2018).

The ratio between pro-apoptotic and anti-apoptotic protein regulators is often a significant factor in determining whether or not a cell undergoes apoptosis (Plati *et al.*, 2008, Mortezaee *et al.*, 2019). The activation of apoptosis in precancerous lesions due to DNA damage can eliminate potentially dangerous cells, halting tumour progression (Fulda, 2009, Mortezaee *et al.*, 2019). Unrestrained cell growth, cancer formation, progression, and cancer resistance to treatments are all linked to deregulation of the process of apoptosis (Plati *et al.*, 2008, Wong, 2011, Carneiro and El-Deiry, 2020).

2.7.1. Morphological and biochemical changes in apoptosis

Apoptotic cell death causes morphological changes in both the nucleus and the cytoplasm, and these changes are strikingly consistent across cell types and species (Naeini *et al.*, 2020). Chromatin

condensation and nuclear fragmentation are morphological hallmarks of apoptosis in the nucleus, which are followed by cell rounding, cellular volume reduction, also known as pyknosis, and pseudopode retraction (D'Arcy, 2019). Condensation of chromatin begins at the nuclear membrane's periphery, making a crescent or ring-like structure. The chromatin condenses even more until it breaks up inside a cell with a functioning membrane, a process known as karyorrhexis (Majtnerová and Roušar, 2018). Membrane exposure of phosphatidylserine (PS) is also a morphological change that allows macrophages to recognize dead cells early, leading to phagocytosis without releasing proinflammatory cellular components (Saraste and Pulkki, 2000, Majtnerová and Roušar, 2018). Some of the morphological features observed later in apoptosis are membrane blebbing, ultrastructural alteration of cytoplasmic organelles, and a loss of membrane integrity (D'Arcy, 2019). Apoptosis is predominantly carried out by a family of proteases known as caspases, essential to the apoptosis mechanism since they both initiate and execute cell death. Initiator caspases (caspase-2, -8, and -9) become activated through homodimerization, and they then cleave and activate the executioner caspases (caspase-3/7) (Su *et al*., 2015). Executioner caspases are responsible for all the morphological apoptotic hallmarks. The irreversible proteolytic activity driven by executioner caspases represents the final results of both the extrinsic and intrinsic apoptotic pathways (Carneiro and El-Deiry, 2020).

2.7.2. Intrinsic pathway

The intrinsic apoptotic pathway is initiated by various stimuli such as irreparable genetic damage, hypoxia, and severe oxidative stress, which generate intracellular signals that converge at the mitochondrial level (Pfeffer and Singh, 2017). The activation of pro-apoptotic BH3-only members of the B-cell lymphoma 2 (Bcl-2) family, Bax and Bak causes the antiapoptotic proteins Bcl-2, B-cell lymphoma-extra-large (Bcl-xL), and myeloid cell leukemia-1 (Mcl-1) to be neutralized, which leads to the disruption of mitochondrial membrane outer membrane permeability (MOMP), allowing proteins like cytochrome *c* which are usually restricted in the intermembrane space to spread into the cytosol (Gong *et al*., 2017). Released cytochrome *c* then binds to the activating factor of apoptotic protease–1 (Apaf-1) and ATP, which then binds to pro-caspase-9 to build an apoptosome (Figure 2.7) (Gong *et al*., 2017). The apoptosome complex binds the initiator pro-caspase-9 through its caspase recruitment domain (CARD), enabling auto-activation and proteolysis (Pistritto *et al.*, 2016). This process then activates the downstream executioner caspases-3/7, which cleave cellular substrates such as PARP, thus causing apoptosis (Pistritto *et al.*, 2016, Tompkins and Thorburn, 2019).

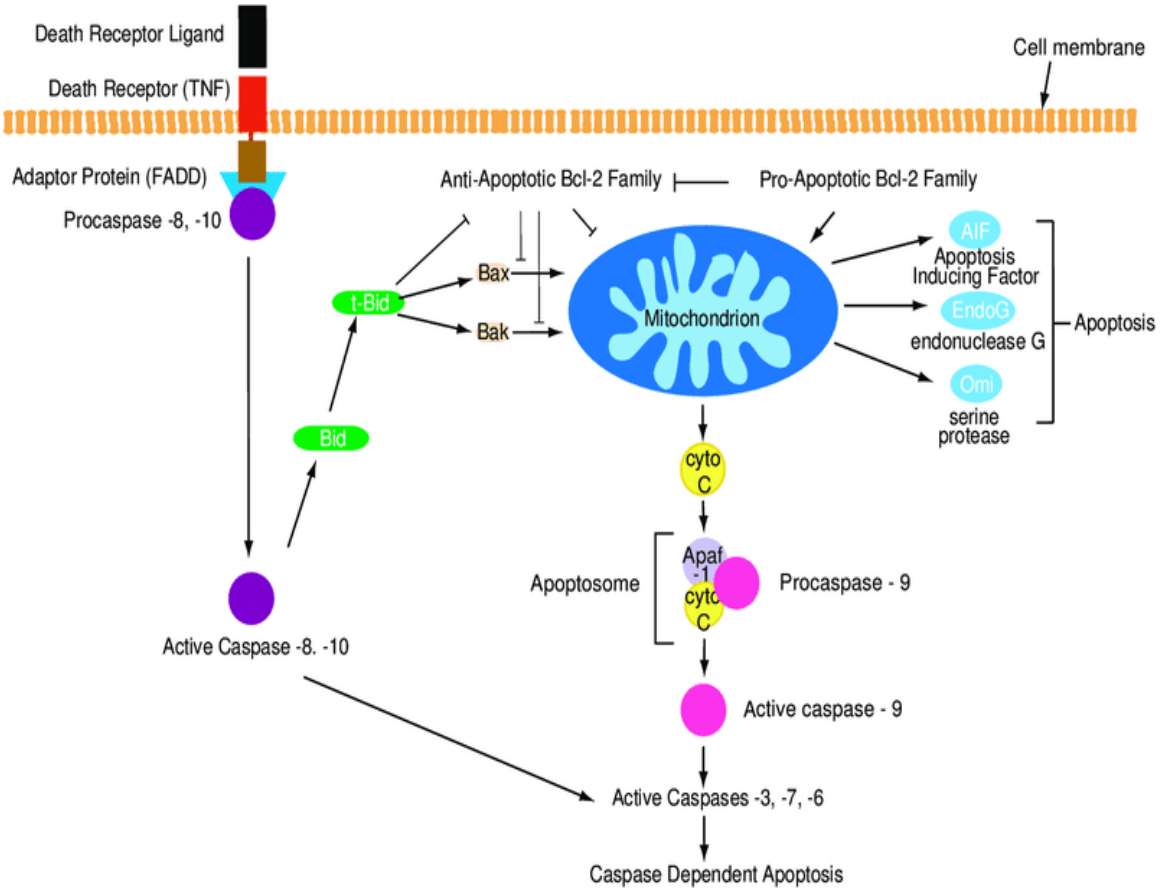

Figure 2.7: The intrinsic and extrinsic pathway of apoptosis (Taabazuing *et al*., 2017).

2.7.3. Extrinsic pathway

The extrinsic pathway is activated by extracellular ligands, which bind to cell-surface death receptors, resulting in the formation of the death-inducing signalling complex [DISC] (Pfeffer and Singh, 2018). The first apoptosis signal (Fas) receptor, which is the transmembrane protein of the Tumour necrosis factor (TNF) family, binds the Fas ligand [FasL] (Gong *et al*., 2017). The DISC complex, which consists of the Fas-associated death domain protein (FADD), pro-caspase-8, and/or pro-caspase-10, is formed when Fas and FasL interact [Figure 2.8] (Zahedifard *et al*., 2015). The formation of the DISC complex causes the pro-caspases to be auto-catalytically cleaved for activation. Active caspase-8 directly cleaves and activates executioner caspase-3/7, whose activation leads to the cleavage of necessary substrates for cell viability, triggering the cell's apoptosis (Pistritto *et al.*, 2016). Caspase-8 also signals the mitochondria via cytosolic Bid, a BH3-only protein. Caspase-8 cleaves Bid to make truncated Bid (tBid), which subsequently translocate from the cytosol to the mitochondria and trigger the release of cytochrome *c*, so this co-engages intrinsic pathway (Jan, 2019).

Loss of apoptotic regulation enables cancer cells to live longer, allowing more time for mutations to accumulate, increasing tumour invasiveness, promoting angiogenesis, deregulating cell proliferation, and interfering with differentiation (Matsuura *et al*., 2016). Drugs that increase apoptosis are desirable as anti-cancer drugs. Metal chelators have been shown to induce apoptosis mediated through ROS production, DNA fragmentation, and decreased mitochondrial membrane potential [$\Delta\Psi m$] (Hong *et al*., 2017, Manikandamathavan *et al*., 2017).

CHAPTER 3: MATERIALS AND METHODS

3.1. Materials

The HepG2 cells were purchased from Highveld Biological (Johannesburg (Jhb), South Africa (SA)). The growth medium used (Eagle's Minimum Essential Medium (EMEM)), flasks, 96-well plates, Eppendorf's, sterilin tubes, and micropipette tips were purchased from Whitehead Scientific (Jhb, SA). H2pmen, 0.1M phosphate-buffered saline (PBS), trypan blue, methyl thiazole tetrazolium (MTT) salt, malondialdehyde (MDA), butylated hydroxytoluene (BHT), thiobarbituric acid (TBA), sodium nitrate, sulphanilamide (SULF), vanadium chloride (VCl_3), and N-1-Naphthyl ethylenediamine dihydrochloride (NEDD), bicinchoninic acid (BCA) kit and β-actin were purchased from Sigma Aldrich (St. Louis, Missouri, United States of America (USA)). Promega (Madison, Wisconsin, United States) luminometry kits and Cell Signalling Technology (CST, Danvers, Massachusetts) primary and secondary antibodies were obtained from Anatech (Jhb, SA). Western blotting reagents were purchased from Bio-Rad (Hercules, California, USA) unless stated otherwise. Ethanol, dimethylsulphoxide (DMSO), salts for buffers, phosphoric acid, butanol, hydrochloric acid (HCl), and all other reagents were purchased from Merck (Darmstadt, Germany).

3.2. Cell culture

Cryovials of HepG2 cells were thawed in an incubator [37 degrees Celsius (^oC), 5% carbon dioxide (CO_2)] for 5 minutes (min) and it was then centrifuged for 10 minutes (min) at 400 x g, room temperature (RT). The supernatant was discarded, and the pellet was resuspended with 1 ml complete culture media (CCM; EMEM supplemented with 1% L-glutamine, 1% penicillin-streptomycin-fungizone, and 10% foetal bovine serum) and then transferred to a 25 cm^3 cell culture flask. A 4 ml of CCM was added to each flask. The flasks were incubated at 37 degrees Celsius (^oC) and 5% carbon dioxide (CO_2) to ensure that the normal physiological pH is maintained for optimum cell growth. The cell growth was monitored and CCM was changed as necessary until ±90% confluency was reached. Confluent flasks of HepG2 cells were trypsinized using 1 ml trypsin (0.05%), and cell numbers were counted using trypan blue and sub-cultured as required for the various assays.

3.2.1. Trypsinisation

Adherent HepG2 cells were dislodged from cell culture flasks for cell counting and plating using the process of trypsinization. Aliquots of trypsin (1 ml for 25 cm^3 cell culture flask) stored at -20^oC were warmed to 37^oC before use. HepG2 cells were rinsed three times with 1 M PBS and 1 ml of trypsin

was added to the flask. The HepG2 cells were visually monitored for rounding and detachment from the culture vessel. When the cells were round in shape, trypsin was discarded, the cells were disloged by agitation and 2 ml of CCM was added to inactivate the trypsin and the cells were counted.

3.2.2. Cell counting

The cell counting solution was prepared by adding 150 µl CCM, 50 µl cell suspension, and 50 µl trypan blue in a microcentrifuge tube. The mixture was vortexed for 5 seconds (s) and 10 µl was pipetted between the hemocytometer and the coverslip. The HepG2 cells in 5 quadrants were counted under the microscope, and the average cell count was used to calculate cells per ml using the formular below. The cell number was adjusted as required for use in the different assays.

$$\text{Cells per ml} = \frac{Total\ number\ of\ cells\ in\ 5\ quadrants\ x\ 5}{5} x\ 10\ 000$$

3.3. Preparation of the treatment

The 5 mg of H2pmen was weighed and dissolved in 10 ml CCM to obtain a 1288 µM stock solution. The stock solution was used to prepare the dilutions used in subsequent assays.

3.4. MTT Assay

3.4.1. Principle

The 3-(4,5-dimethylthiazol-2-yl)-2,5-diphenyltetrazolium bromide (MTT) assay is a colorimetric assay used as a measure of cell viability, proliferation and cytotoxicity by calculating cellular metabolic activity (Aslantürk, 2018). This assay is based on the reduction of yellow tetrazolium salt to purple formazan crystals by metabolically active cells (Bahuguna *et al.*, 2017, Guo *et al*., 2021). The viable cells contain enzymes such as NAD(P)H-dependent oxidoreductase that reduce the MTT to purple formazan (Figure 3.1) (Guo *et al.*, 2021). The insoluble formazan crystals are then solubilized using an organic solvent and quantified using a wavelength of 570 nm (Kamiloglu *et al*., 2020). The darker the solution, the more significant the amount of metabolically active, viable cells (Bahuguna *et al*., 2017).

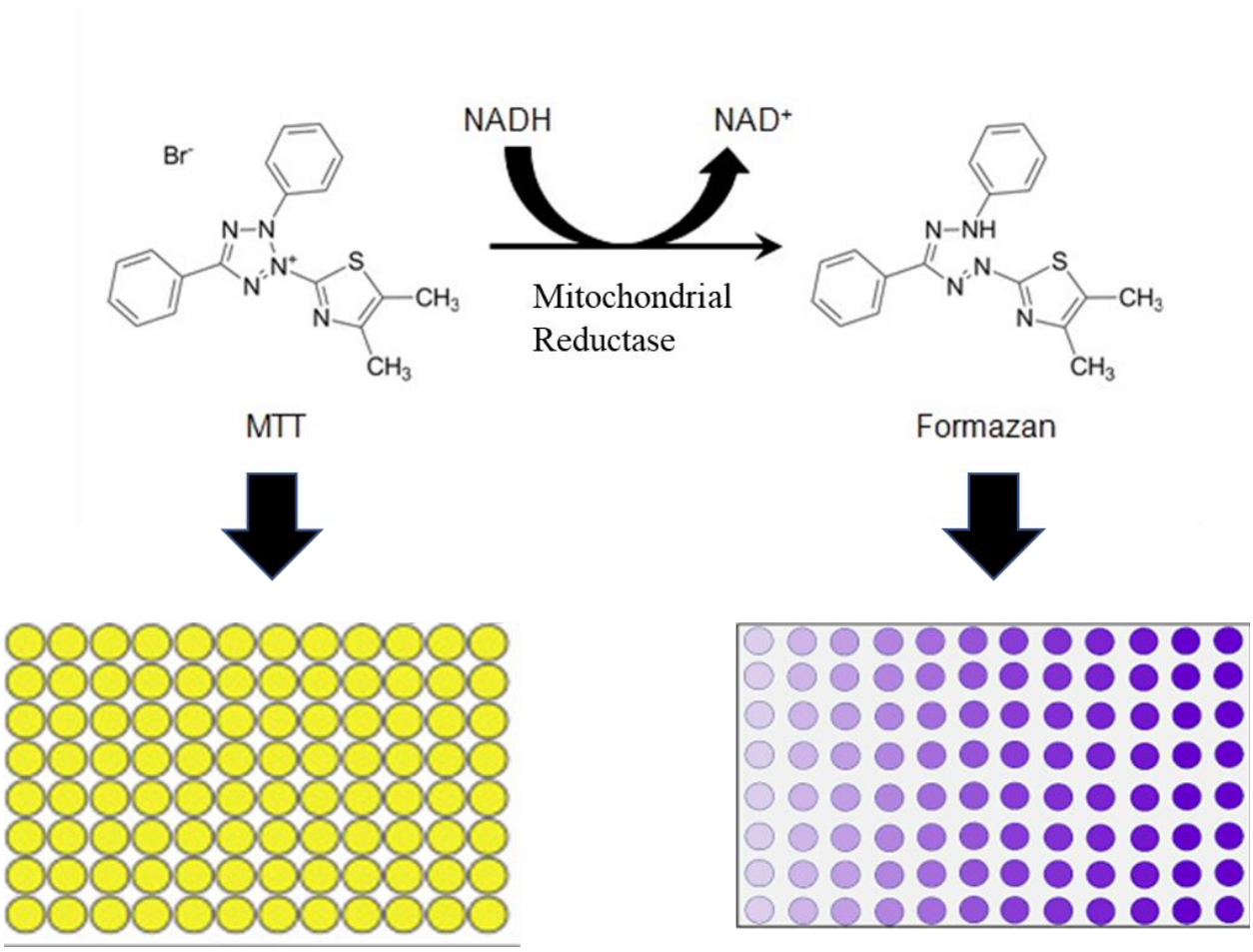

Figure 3.1: The reduction of the yellow tetrazolium MTT salt to purple formazan product [Modified from (Shunmugam *et al*., 2016)].

3.4.2. Protocol

The cytotoxicity of H2pmen was measured in HepG2 cells using the MTT assay. The HepG2 cells (15 000 cells/well) were seeded in triplicate in a 96-well microtiter plate and allowed to attach overnight (37°C, 5% CO_2). The cells were then treated for 24 hours (h) with a range of H2pmen concentrations (0, 25, 50, 100, 250, 500, 750, and 1000 µM) in triplicate (200 µl/well). The treatment medium was discarded, and each well was replenished with 20 µl of MTT salt solution (5 mg/ml in 0.1 M PBS) and CCM (100 µl/well) for 4 h. After that, supernatants were removed, and cells were incubated in DMSO (100 µl/well) for 1 h to solubilize formazan crystals. The formazan product's optical density (OD) was measured using a spectrophotometer (SPECTROstar Nano, BMG Labtech, Ortenberg, Germany) at 570 nm, with a reference wavelength of 690 nm. The percentage cell viability was calculated using the equation below, and GraphPad Prism V5.0 software (GraphPad Software Inc., La Jolla, USA) was used to plot the concentration-response curve. Each experiment was conducted twice on separate occasions to determine the half-maximal inhibitory concentration (IC_{50}).

$$\% \text{ Cell viability} = \frac{mean\ absorbance\ of\ treated\ cells}{mean\ absorbance\ of\ control\ cells}\ x\ 100$$

An IC_{50} of 209 μM was obtained. The IC_{20} of 71 μM which indicates the concentration of H2pmen needed to inhibit HepG2 cells proliferation cells by 20% was extrapolated from the standard curve. Subsequently, HepG2 cells were maintained in 75 cm^2 flasks until 90% confluent, then treated with the IC_{20} and IC_{50}. Control cells remained untreated and received CCM only. The treated cells were trypsinised and counted, then plated as required for the various assays.

3.5. Luminometry

Luminometry is a very sensitive method that uses a luminometer to measure photons of light via phototubes (Aslantürk, 2018). The functional principle of luminometers is based on luminescence. This phenomenon is commonly attributed to oxidative reactions that occur in solution, resulting in excited molecules (García-Ponce *et al.*, 2021). Some of these processes release energy in the form of heat, while others produce photons (García-Ponce *et al.*, 2021). Current commercial luminometric technology employs a phototube in the 400-420 nm wavelength range which is the most effective for light emission (Duman *et al.*, 2015, Aslantürk, 2018). Intracellular caspases in treated cells release luciferin from the substrate (Jung *et al.*, 2020). Luciferase action then results in the formation of a light signal that is quantified using the luminometer (Jung *et al.*, 2020).

3.5.1.Cytochrome P450 3A4 Activity

3.5.1.1. Principle

The P450-GloTM CYP3A4 assay uses a luminescence approach to assess CYP3A4 activity. The assays are used to determine P450 activity from mutant and indigenous sources and investigate the effects of analytes such as drugs and novel chemical entities on P450 activity (Ning *et al.*, 2019). The assay is based on the conversion of a luciferase-inactive D-luciferin derivative to D-luciferin by CYP3A4 (Chapron *et al.*, 2020). D-luciferin is released and interacts with luciferase to produce a luminescent signal (Figure 3.2) (Promega corporation, 2021). The luminescent signal is proportional to the activity of CYP3A4.

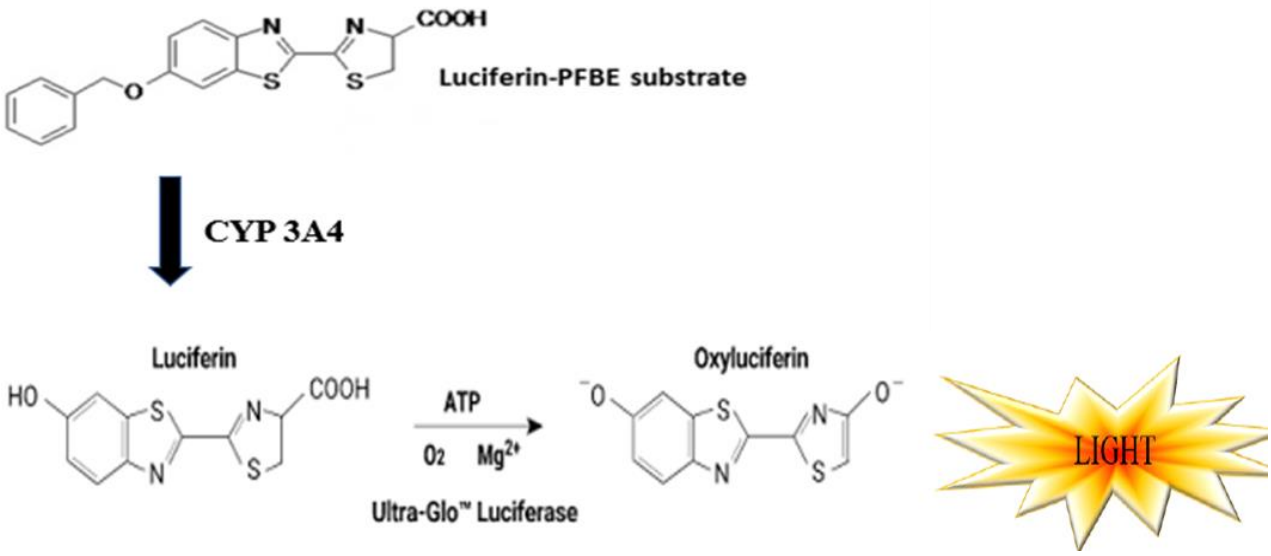

Figure 3.2: The conversion of an inactive luciferin derivative to luciferin in the presence CYP 3A4 of to produce a luminescence signal through luciferase interaction [Modified from (Shunmugam, 2016)].

3.5.1.2. Protocol

The activity of cytochrome P450 3A4 (CYP3A4) activity was measured by the P450-Glo™ assay kit (#V8901/2, Promega, Madison, USA). The H2pmen treated and untreated (control) HepG2 cells were resuspended in 0.1 M PBS and aliquoted in triplicate into a white 96-well luminometer plate (20,000 cells/well in 50 µl 0.1 M PBS). The 25 µl of P450-Glo™ prepared before the assay according to the manufacturer's guidelines was added into each well, and the plate was then incubated (30 min, dark, RT). Luminescence was measured using a Modulus™ microplate luminometer (Turner Bio-systems, Sunnyvale, California, USA). Data obtained was expressed as relative light units (RLU).

3.5.2. ATP Quantification Assay

3.5.2.1. Principle

The ATP assay is a technique that uses bioluminescence to detect ATP to determine cell viability (Zhang *et al.*, 2020). The firefly luciferase enzymatic reaction, which uses ATP from living cells to produce light photons was used in this assay. Reagents containing firefly luciferase enzyme and substrate are used to catalyze a two-step reaction after viable cells are lysed to release ATP for detection (Promega corporation, 2021). The first step was to activate D-luciferin with ATP in the presence of Mg^{2+} to produce luciferyl-adenylate and pyrophosphate (Nguyen *et al.*, 2021). In the second step, the luciferyl-adenylate reacts with O_2 to produce oxyluciferin in an electronically excited state and CO_2 (Adan *et al*., 2018). The luminescent signal is directly proportional to the concentration of ATP and thus cell viability (Figure 3.3). A luminometer was used to measure the intensity of the luminescent signal.

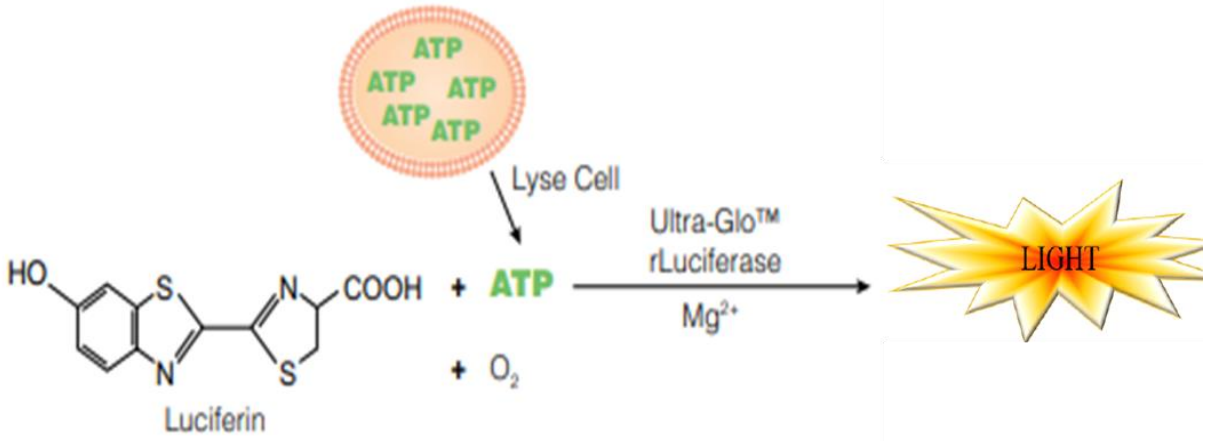

Figure 3.3: Bioluminescent reaction catalyzed by luciferase in the presence of ATP, $Mg^{2+,}$ and molecular O_2 to quantify ATP in the cells [Modified from (Promega corporation, 2021)].

3.5.2.2. Protocol

Intracellular ATP levels were quantified by Cell Titre-Glo® luminescent assay (#G7570, Promega, Jhb, SA). Treated (H2pmen) and untreated (control) HepG2 cells were resuspended in 0.1 M PBS and aliquoted in triplicate into a white 96-well luminometer plate (20,000 cells/well in 50 µl 0.1 M PBS). Thereafter, 25 µl of reagent prepared according to manufacturer's instruction was added to the treated cells, followed by incubation (30 min, dark RT). After incubation, a Modulus™ microplate luminometer (Turner BioSystems, Sunnyvale, California, USA) was used to detect luminescent proportional to the intracellular ATP level. Data obtained was expressed as RLU.

3.5.3. Mitochondrial membrane potential (ΔΨm) assay

3.5.3.1. Principle

The ΔΨm assay employed JC-10, a JC-1 derivative that can be used in flow cytometry and microplate-based fluorescent experiments to determine ΔΨm in mammalian cells and for screening apoptosis inhibitors and activators using microplate readers (Miyai *et al*., 2018). In healthy cells, JC-10 concentrates in mitochondria and emits red-fluorescent JC-10 aggregates (λex = 540/λem = 590 nm) (Limboonreung *et al*., 2020, Promega corporation, 2021)). However, when a cell is injured, JC-1 monomers are produced as the membrane potential decreases, leading to a change to green fluorescence emission (λex = 490/λem = 525 nm) (Miyai *et al*., 2018) (Figure 3.4).

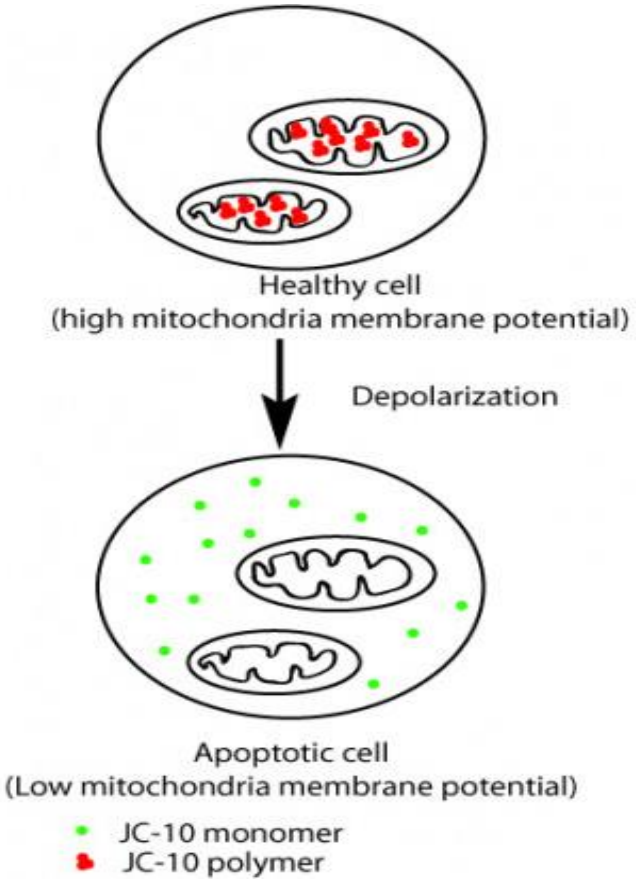

Figure 3.4: The JC-10 assay showing the conversion of red to green fluorescence as an indication of decreased mitochondrial membrane potential [Adapted from (Miyai *et al.*, 2018)].

3.5.3.2. Protocol

The JC-10 Mitochondrial Membrane Potential Assay Kit (#MAK159, Sigma, St. Louis, Missouri, United States) was used to determine changes in mitochondrial membrane potential. The H2pmen-treated and untreated (control) HepG2 cells were resuspended in 0.1 M PBS and aliquoted in triplicate for each caspase into a white 96-well luminometer plate (20,000 cells/well in 50 µl 0.1 M PBS). The JC-10 dye was prepared as per the manufacturer's instruction (1% of JC-10 dye in assay buffer), and 20 µl was added to each well, and the plate was incubated (30 min, dark, RT). A Modulus™ microplate luminometer (Turner BioSystems, Sunnyvale, California, USA) was used to detect the fluorescent signals using red fluorescent at 490/525 nm and green fluorescent at 540/590 nm wavelength. The ratio was calculated by dividing the red fluorescence values obtained from the luminometer by the green luminescence values to obtain the reported ratios. Data obtained was expressed as relative fluorescence units (RFU).

3.5.4. GSH Assay

3.5.4.1. Principle

The GSH-Glo™ Assay is a luminescent-based assay used to detect and quantify GSH levels in cells. Changes in GSH levels are crucial for evaluating toxicological responses since they are a marker of oxidative stress, facilitating apoptosis (Sun *et al*., 2019). The assay is based on GSH S-transferase (GST) catalyzing the conversion of a luciferin derivative to luciferin in the presence of GSH (Promega corporation, 2021). In a linked reaction with fluorescent luciferase, the signal generated is proportional to the amount of GSH present in the sample (Promega corporation, 2021).

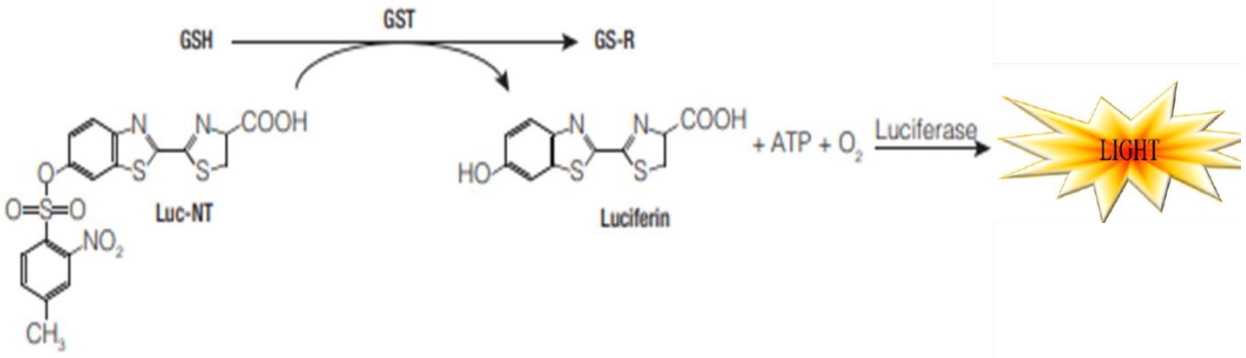

Figure 3.5: Bioluminescent reaction catalyzed by luciferase in the presence of GSH and GST to quantify GSH in the cells [Modified from (Promega corporation, 2021)].

3.5.4.2. Protocol

Intracellular GSH levels were quantified using the GSH-Glo™ assay (# V6911/2, Promega, Jhb, SA). The H2pmen-treated and untreated (control) HepG2 cells were resuspended in 0.1 M PBS and aliquoted in duplicate into a white 96-well luminometer plate (20,000 cells/ well in 50 µl 0.1 M PBS). The 20 µl of GSH-Glo™ reagent made up as per the manufacturer's instructions was added into each well, and the plate was then incubated (30 min, dark, RT). Thereafter, 12.5 µl of reconstituted Luciferin Detection Reagent was added and incubated (15 min, RT, dark). Luminescence was measured using a Modulus™ microplate luminometer (Turner Bio-systems, Sunnyvale, California, USA). Data obtained was expressed as RLU.

3.5.5. Assessment of Caspases

3.5.5.1. Principle

The Caspase-Glo® Assay is a luminescent, homogenous assay for measuring caspase activity. The caspase cleaves luminogenic substrate conjugated aminoluciferin in this technique (Mposula *et al*.,

2021). When the aminoluciferin is released, it works as a luciferase substrate, reacting with the enzyme luciferase in the presence of ATP and molecular oxygen to produce a luminescent signal (Promega corporation, 2021). The level of caspase activity is proportional to the amount of luminescence (Figure 3.6).

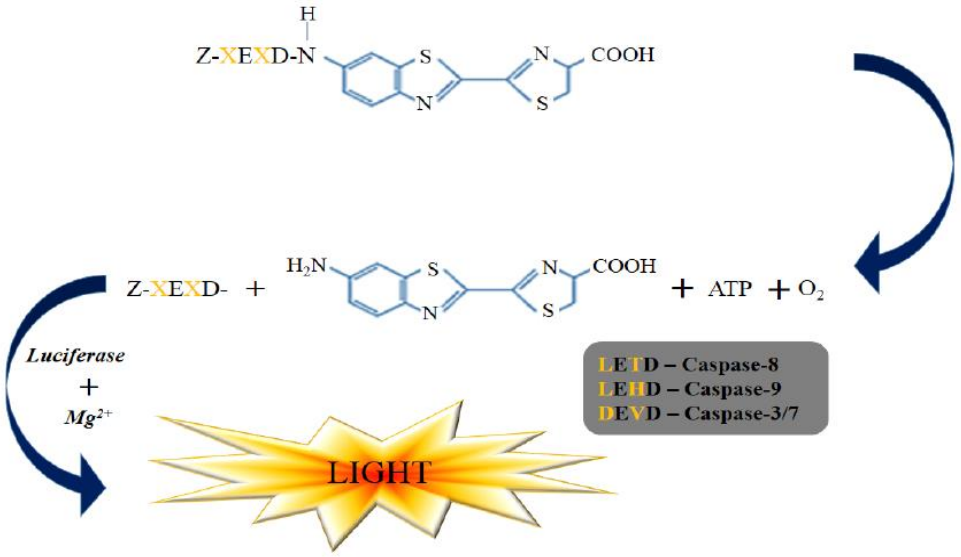

Figure 3.6: Bioluminescent quantification of caspase -8, -9 and -3/7 activity (Adapted from Devnarain *et al*., 2017). The X represents the peptide sequence: LETD (caspase -8), LEHD (caspase-9), or DEVD (caspase-3/7).

3.5.5.2. Protocol

The activities of caspase-3/7 (#8090, Promega, Madison, Wisconsin, United States), -8 (# 8200, Promega, Madison, Wisconsin, United States), and -9 (#8210, Promega, Madison, Wisconsin, United States) and were identified using the Caspase-Glo® assay kit (Promega, Jhb, SA). The treated (H2pmen) and untreated (control) HepG2 cells were resuspended in 0.1 M PBS and aliquoted in triplicate for each caspase into a white 96-well luminometer plate (20,000 cells/well in 50 µl 0.1 M PBS). Caspase-Glo®-3/7, -8, and -9 reagents were reconstituted as per the manufacturer's instruction, and 25 µl was added into each well, and the plate was incubated (30 min, dark, RT). Luminescence was detected using a Modulus™ microplate luminometer (Turner Bio-systems, Sunnyvale, California, USA), and data were expressed as RLU.

3.5.6. Annexin V assay

3.5.6.1 Principle

Annexin V is a cellular protein that belongs to the annexin family. The ability of annexin V to bind to phosphatidylserine, a biomarker of apoptosis when it is on the outer leaflet of the plasma

membrane, is often utilized in flow cytometry to identify apoptotic cells (Kupcho *et al*., 2019). Annexin V binding assay is based on the measurement of the loss of plasma membrane asymmetry (Álvarez-Teijeiro *et al*., 2017). In normal physiological conditions, the phospholipid distribution between the two leaflets of the cellular membranes is strictly asymmetric, with phosphatidylserine (PS) facing the cytosolic side (Kabakov and Gabai, 2018). This asymmetry vanished quickly in the early phases of apoptosis, while the membrane's integrity remained intact, allowing PS to be exposed to the outer leaflet via phagocytosis (Álvarez-Teijeiro *et al*., 2017). Hapten-labeled Annexin V, which has a strong affinity for PS residues in the presence of micromolar Ca^{2+} concentrations, can detect this phenomenon (Figure 3.7). Apoptotic and necrotic cells are distinguished by simultaneously excluding the nuclear dye propidium iodide (PI) (Kabakov and Gabai, 2018).

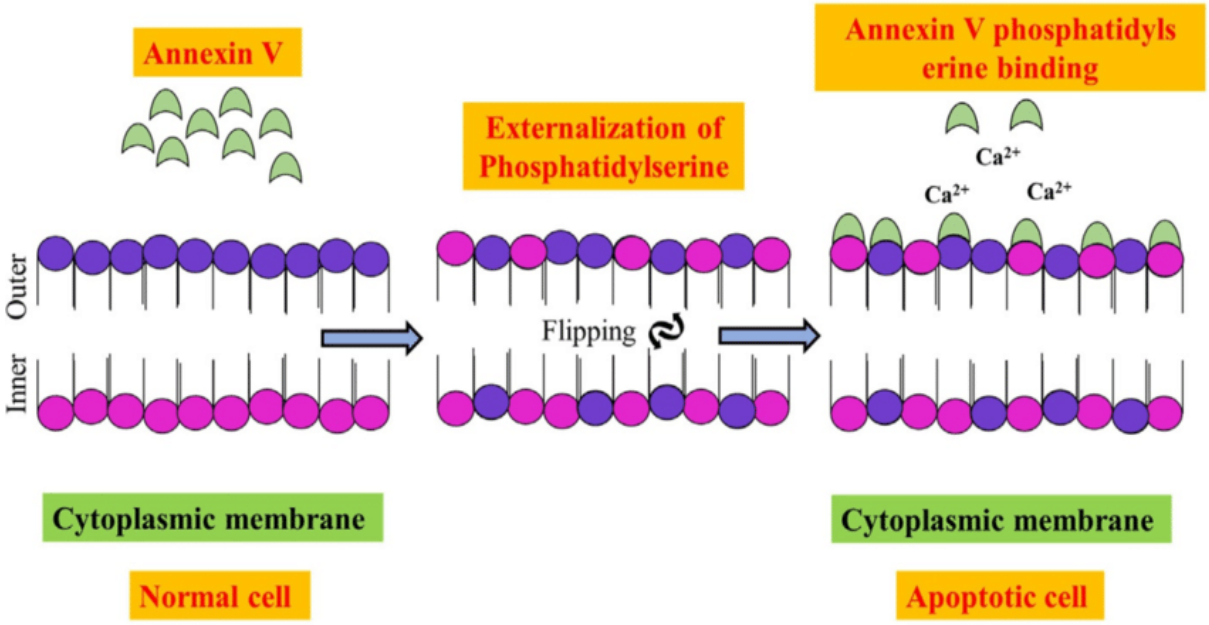

Figure 3.7: Schematic representation of PS externalization to the outer part of cytoplasmic membrane and binding with annexin v in the presence of Ca^{2+} (Adapted from Sumit Jawmal., 2021).

3.5.6.2. Protocol

Apoptotic and necrotic cells were detected using Real-Time-Glo™ Annexin V Apoptosis and Necrosis assay (#JA10111, Promega, Jhb, SA). The treated (H2pmen) and control (untreated) HepG2 cells were resuspended in 50 µl 0.1 M PBS and aliquoted in triplicate for each caspase into a white 96-well luminometer plate (20,000 cells/ well). Real-Time-Glo™ Annexin V reagents were prepared according to the manufacturer's instruction, and 20 µl was added into each well, and the plate was incubated (30 min, dark, RT). A Modulus™ microplate luminometer (Turner Bio-systems, Sunnyvale, California, USA) was used to detect the luminescent signals, and data were expressed as RLU.

3.6. Spectrophotometry

Spectrophotometry is a technique for determining how much light a chemical substance absorbs by measuring the intensity of light as it travels through a sample solution (Abasi *et al.*, 2021). The fundamental principle is that each substance absorbs or emit light across a specific wavelength range (Hou *et al.*, 2018). Photometers also known as spectrophotometers are used in this technique to measure the intensity of a light beam at various wavelengths (Ravichandran *et al.*, 2014, Bennani *et al.*, 2021). This technique can also be used to determine the amount of a chemical compound that is known (Hou *et al.*, 2018).

3.6.1. Thiobarbituric acid reactive substance (TBARS) Assay

3.6.1.1. Principle

The TBARS assay is performed to determine if oxidative stress occurred by detecting the levels of MDA, the main lipid oxidation by-product (De Leon and Borges, 2020). The thiobarbituric acid (TBA) reacts with MDA in this assay to create a pink adduct at low pH and high temperature; butylated hydroxytoluene (BHT) added during sample preparation prevents further sample peroxidation during processing (Danet, 2021). The adduct is extracted in butanol and detected using a colorimetric (OD = 532 nm) or fluorometric plate reader (Figure 3.8) (Ghani *et al.*, 2017, De Leon and Borges, 2020).

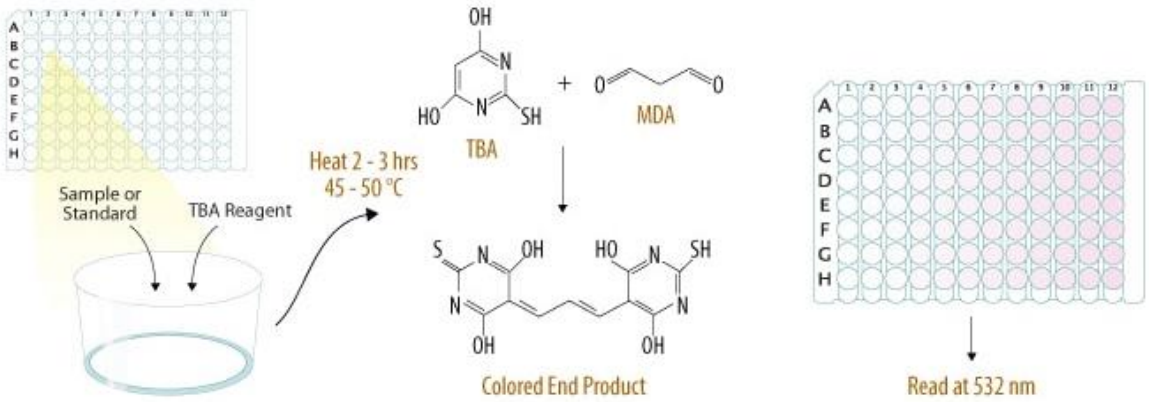

Figure 3.8: Reaction between MDA and TBA/BHT in TBARS assay [Adapted from (Ghani *et al.*, 2017)].

3.6.1.2. Protocol

The TBARS assay was used to measure the extent of lipid peroxidation in H2pmen-treated HepG2 cells. Following the H2pmen treatments, 200 µl of supernatant per control/treatment was added into

appropriately labeled, sterile glass test tubes. A negative control (200 µl CCM) and positive control (1 µl MDA + 199 µl CCM) were also prepared. The 2% phosphoric acid (200 µl) and 7% phosphoric acid (400 µl) were sequentially added to each of the test tubes to inactivate any interfering proteins/enzymes. This was followed by the addition of 400 µl TBA/BHT to each sample except the blank. Instead, 400 µl of 3 mM HCl was added to the blank. All test tubes were vortexed, and 200 µl 1M HCl was added to acidify each sample. The tubes were boiled in a water bath for 15 min at 100^{o}C to achieve the optimal hydrolysis of MDA adducts. Thereafter, the tubes were allowed to cool at RT before adding 1500 µl of butanol into each tube to ensure the extraction of MDA through phase separation. Each tube was vortexed and allowed to separate into two phases. The upper butanol phase (500 µl) was transferred to microcentrifuge tubes. Each sample was transferred to a 96-well microtiter plate in triplicate (100 µl per well). Absorbance was measured using the SPECTROstar Nano (BMG Labtech, Ortenberg, Germany) spectrophotometer at 532 nm, with a reference wavelength of 600 nm. The average concentration of MDA (µM) was established by dividing the mean replicates by the absorption coefficient (156mM^{-1}) (De Leon and Borges, 2020).

3.6.2. Nitrates Assay

3.6.2.1. Principle

Nitric oxide synthase (NOS) belongs to a group of enzymes that catalyze the synthesis of nitric oxide (NO) from L-arginine (Dong *et al*., 2018). The NO is a diatomic free radical that has a very short half-life. Therefore, it is rapidly oxidized to create stable metabolite products, which are nitrate (NO_3^-) and nitrite (NO_2^-) (Zhu *et al*., 2015). These stable metabolites are then used to indirectly measure NO concentration (Dong *et al*., 2018). The reduction of NO_3^- to NO_2^- is catalyzed by VCl_3 in this colorimetric assay (Figure 3.9) (Dong *et al*., 2018). The diazonium ion undergoes the Griess reaction, where SULF and NEDD reacts with NO_2^- to form a pink azo dye product, that can be measured by spectrophotometer at a 540 nm (Gao *et al.*, 2019).

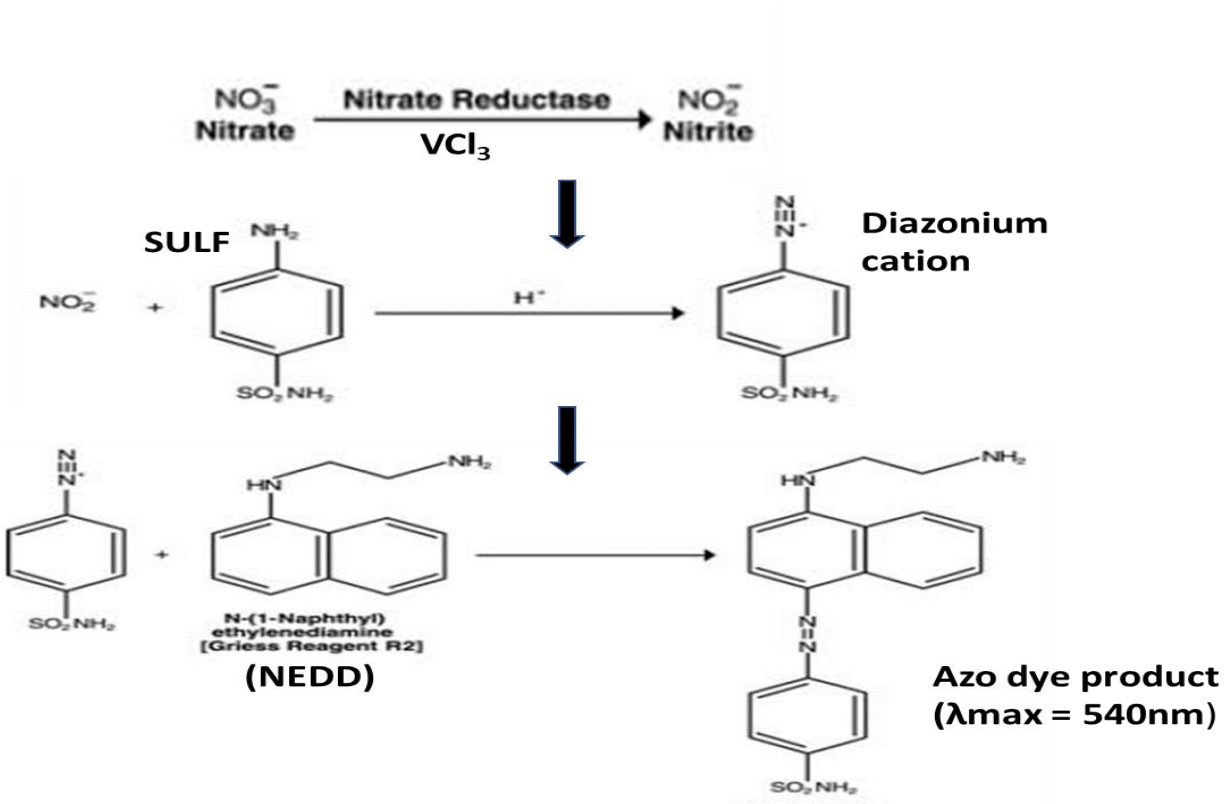

Figure 3.9: The reduction of NO_3^- to NO_2^- catalyzed by VCl_3 which further reacts with SULF and NEDD to form azo dye product [Modified from (Dong *et al*., 2018)]

3.6.2.2. Protocol

The NOS assay was used to measure the effect of H2pmen on NO production in HepG2 cells. Following H2pmen treatments, supernatant from samples and standards (0, 25, 50, 75, 25, 50, 100,125, 150,175, 200 µM) (50 µl) were aliquoted, in triplicate, into a 96-well microtiter plate. Subsequently, 50 µl VCl_3, 25 µl SULF, and 50 µl NEDD were added in quick succession into each well, and the plate was incubated (dark, 45 min, 37ºC). The absorbance was measured at a wavelength of 540 nm, with a reference wavelength of 690 nm using the spectrophotometer (SPECTROstar Nano, BMG Labtech, Ortenberg, Germany). Standard means were used to generate a standard curve from which the nitrates and nitrite levels in the samples were extrapolated. Data were represented as mean nitrates/nitrite concentration (µM).

3.6.3. Lactate dehydrogenase (LDH) Cytotoxicity Detection Assay

3.6.3.1. Principle

The LDH assay is cell death and cytotoxicity assay used to determine the extent of plasma membrane damage in a cell population (Kumar *et al*., 2018). Generally, LDH is a stable enzyme found in the cytosol of all cell types and is released rapidly into the extracellular culture medium when the plasma

membrane is damaged (Cox *et al.*, 2021). The LDH is the most commonly used marker for cytotoxicity. This assay has two enzymatic reactions, including converting lactate to pyruvate to reduce nicotinamide adenine dinucleotide (NAD^+) to $NADH/H^+$ (Parhamifar *et al.*, 2019). The transfer of H/H^+ from $NADH/H^+$ to a tetrazolium salt, iodonitrotetrazolium (INT), is then catalyzed by an oxidase (diaphorase enzyme), resulting in a purple formazan product (Figure 3.10) (Cox *et al.*, 2021).

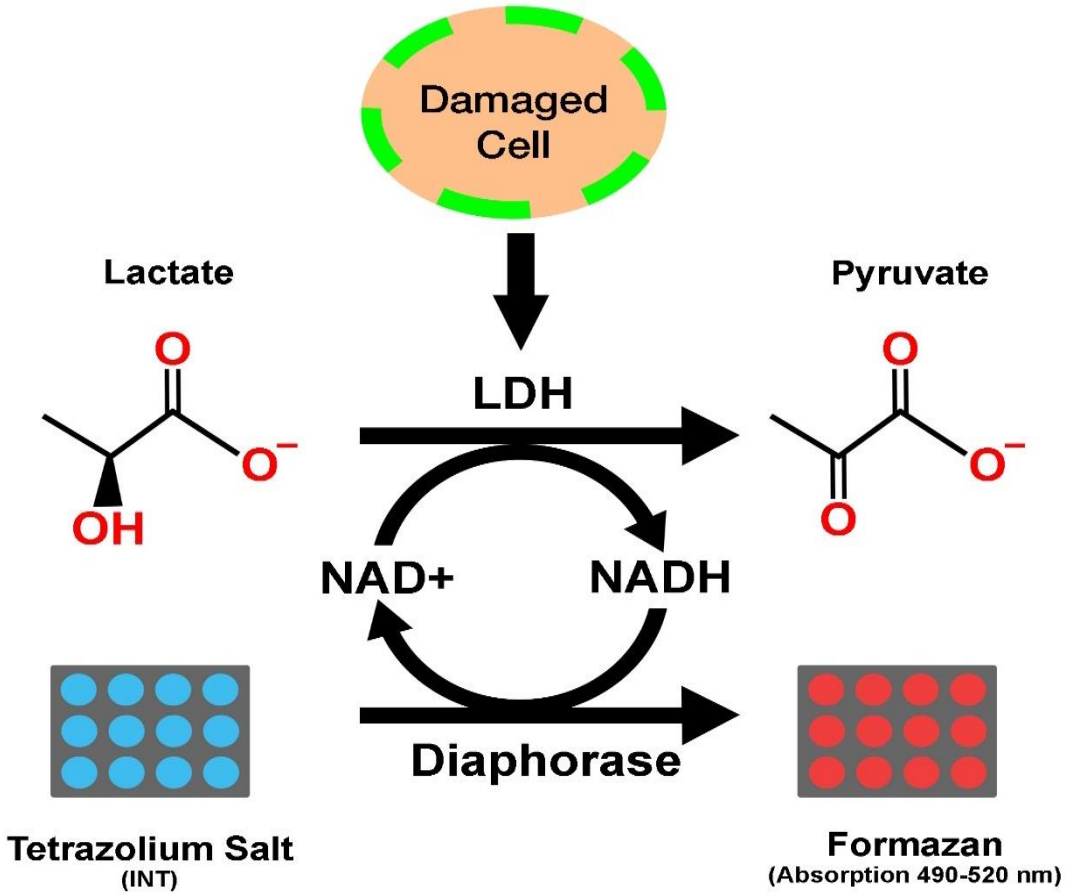

Figure 3.10: The conversion of lactate to pyruvate by LDH and diaphorase to form pink/purple formazan [Adapted from (Parhamifar *et al*., 2019)].

3.6.3.2. Protocol

Extracellular LDH levels were quantified using a Cytotoxicity Detection Kit (#04744926001, Roche, Mannheim, Germany). Treatment supernatants (50 µl) were pipetted into a microtiter plate, in triplicate. Thereafter, 50 µl of the substrate mixture [dye solution (INT/sodium lactate) and catalyst (diaphorase/NAD^+)] was added to each well, and the plate was incubated for 30 min at 37°C to allow the reaction to take place. The stop solution (25 µl) was added to each well to stop the reaction. Formazan product was formed, and optical density was measured at a wavelength of 490 nm with a

reference wavelength of 600 nm using the SPECTROstar Nano spectrophotometer (BMG Labtech, Ortenberg, Germany). Data was expressed as optical density (OD).

3.7. Western Blotting

3.7.1. Principle

Western blotting is a commonly used analytical technique for detecting specific proteins in a sample of tissue homogenate or extract (Bass *et al*., 2017). To separate a specific protein from a complex, the western blot approach employs three steps: size separation, protein transfer to a solid support and visualization of the target protein using a primary and secondary antibody (Gallo-Oller *et al*., 2018). An antibody is developed that recognizes and binds to a specific target protein. Before excess antibody is washed off, the electrophoresis membrane is washed in a solution containing the primary antibody (Pillai-Kastoori *et al.*, 2020). A secondary antibody is introduced that identifies the original antibody and attaches to it (Gallo-Oller *et al*., 2018). The secondary antibody can be seen using various techniques, including staining and immunofluorescence, which allows for indirect identification of the particular target protein (Bass *et al*., 2017). Proteins are represented by bands, with the width of each band equal to the quantity of the protein of interest (Lewis *et al*., 2019).

3.7.2. Protocol

Western blot was used to determine the effect of H2pmen on protein expression of inducible nitric oxide synthase (iNOS, #13120), SOD2 (#13141), Bcl-2-associated X protein (Bax, #5023), Caspase-2 (#2224), and Poly (ADP-ribose) polymerase 1 (PARP1, #9542) on HepG2 cells.

3.7.2.1. Sample preparation

Total protein was extracted using CytoBuster reagent (catalog no. 71009; Novagen, San Diego, California), supplemented with protease and phosphatase inhibitors (Roche, Germany, 05892791001 and 04906837001, respectively), per manufacturer's instructions. CytoBuster reagent (400 µl) was added to H2pmen-treated and control (untreated) HepG2 cells in a 75 cm^2 flask and left on ice for 15 min and subsequently centrifuged (10 000 xg; 4°C, 10 min) to obtain a crude protein extract. The supernatant was transferred to a clean labeled microcentrifuge tube and kept on ice. Protein concentration was determined using the bicinchoninic acid (BCA; Sigma, St Louis, Missouri) assay. Briefly, bovine serum albumin (BSA) standards (0, 0.2, 0.4, 0.6, 0.8, 1 mg/ml) were prepared and pipetted (12.5 µl) into duplicate wells of a 96-well plate. Thereafter, 100 µl of BCA solution consisting of 2 µl $CuSO_4$ and 99 µl BCA was prepared and added to each well. The plate was then

incubated at 37ºC for 30 min, and absorbance was measured at 562 nm using the SPECTROstar Nano spectrophotometer (BMG Labtech, Ortenberg, Germany). A standard curve was constructed using the average absorbances of the standards, and the crude protein concentration of each sample was calculated using the extrapolated equation.

The samples were then standardized to a 1.5 mg/ml concentration in CytoBuster to facilitate a protein expression comparison between treated samples. Thereafter, Laemmli buffer (dH_2O, 0.5M Tris-HCl (pH 6.8), 3% glycerol, 10% SDS, 12% β-mercaptoethanol, 1% bromophenol blue) was added to the standardized protein samples in a 1:4 ratio, and the samples were boiled for 5 min at 100°C. The samples were stored at -80°C.

3.7.2.2. Sodium dodecyl sulfate-polyacrylamide gel electrophoresis

SDS polyacrylamide gel electrophoresis was used to separate denatured protein samples based on molecular size (Figure 3.11). Initially, 10% resolving gel was prepared (dH_2O, 1.5MTris, 10% SDS, Bis/acrylamide, 10% ammonium persulphate [APS], tetramethylene diamine [TEMED]) was added between glass plates in a casting stand and allowed to polymerize (1 h). Thereafter, 4% stacking gel was prepared (dH_2O, 0.5 M Tris, 10% SDS, Bis/acrylamide, 10% APS, and TEMED) and added on top of the resolving gel (1 h). The standardized protein samples (25 µl) and a molecular-weight marker (5 µl) were loaded into the gels, submerged in a tank containing 1x running buffer (dH_2O, SDS, glycine, Tris, 4ºC) and electrophoresed (150V, 1.5 h) with the Bio-Rad compact power supply (Hercules, California, USA) to facilitate protein separation.

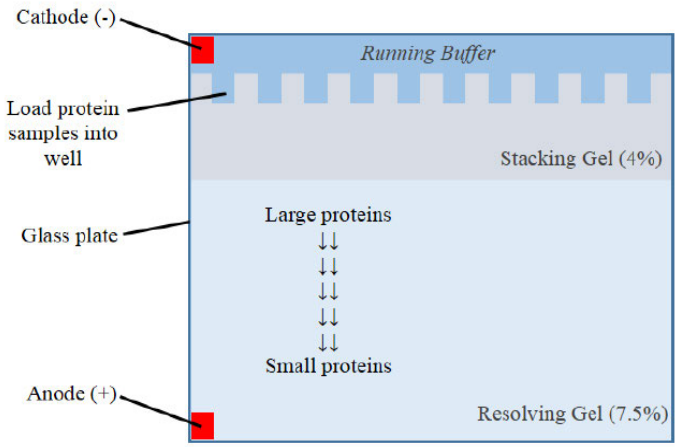

Figure 3.11: The setup of the gel electrophoresis apparatus [Adapted from (Devnarain *et al*., 2017)].

3.7.2.3. Electro-transfer

After electrophoresis, the gels and nitrocellulose membrane were equilibrated in transfer buffer (dH_2O, Tris, glycine, methanol, pH 8.3, 4^oC) for 10 min. The separated protein bands were electro-transferred from the gel to the nitrocellulose membrane using a Bio-Rad Trans-Blot Turbo Transfer System (Hercules, California, USA) (Figure 3.12) (25 V, 2.5 mA, 30 min).

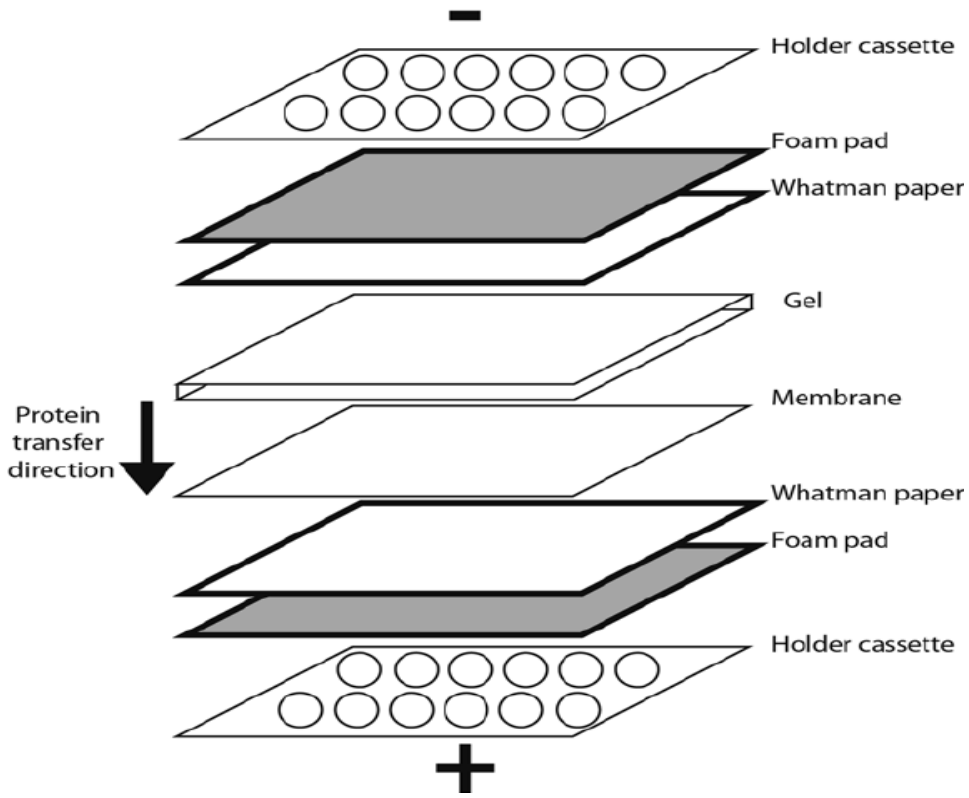

Figure 3.12: Protein transfer from the gel to the membrane [Adapted from (Kupcho et al.,2019)].

3.7.2.4. Immunoprobing

Nonspecific binding of antibodies was prevented by blocking the nitrocellulose membranes. They were submerged in 5% BSA in Tris-buffered saline (dH_2O, Tris-HCl [pH 7.4], NaCl) containing 0.5% Tween-20 (TTBS) and incubated on shaker for 2 h at RT. Membranes were incubated with the individual primary antibodies (1:1,000 in 5% BSA in TTBS) for 1 h at RT and at 4^oC overnight to allow the antibody to bind to its specific target protein. The membranes in the primary antibody were placed on a shaker for 1 h to allow them to reach RT. They were washed 5 times (10 min each time) with 10 ml TTBS to remove excess antibody that did not bind to target proteins and probed with horseradish peroxidase (HRP)-labeled secondary antibody (1:2,500 in 5% BSA in TTBS). Membranes were washed 5 times (TTBS, 10 min). A Clarity Western luminal/enhancer solution and peroxide substrate solution (catalog no. 1705061, Bio-Rad) was added onto each electro-blotted nitrocellulose membrane to form the antigen-antibody complex (Figure 3.13). The generated signal

was detected using the Chemidoc™ Imaging System (Bio-Rad), and protein expression was analyzed with Image Lab™ Software (Bio-Rad). After that, the membranes were quenched with 5% H_2O_2, rinsed three times (10 min, TTBS), blocked in 5% BSA (2 hr; RT), and probed with β-actin (ab8226) (Sigma, St Louis, Missouri, USA) in a 1:5 000 dilution with 5% BSA (30 min) for protein normalization and loading control. The data was expressed as relative fold change (RFC).

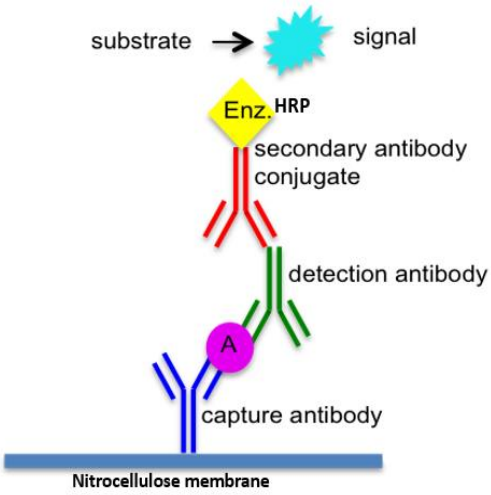

Figure 3.13: Schematic representation of indirect immunodetection involving antigen-antibody interactions [Adapted from (Kupcho *et al*., 2019)].

3.8. Quantitative polymerase chain reaction (qPCR)

3.8.1. Principle

The qPCR is a method used to amplify a specific DNA sequence from template strands. Primers, which are single-stranded DNA flanking the targeted gene, are used in this technique (Mohan, 2019). Primers are then extended via DNA polymerase (Taq polymerase), which allows for the addition of deoxynucleotide triphosphates (dNTP) to the 3' end of primers (Nagura-Ikeda *et al*., 2020). The thermocycler is used to perform PCR where it undergoes repetitive cycling (30-40 times) of three incubation steps at different temperatures to exponentially produce exact copies of the target DNA (Sibiya, 2018). Amplification is achieved by a series of three steps (Figure 3.14):

1. Denaturation **(**95^{o}C) - heat is used to denature the double-stranded (Davidson, #359) DNA templates to form single-stranded (ss) DNA templates.
2. Annealing (55^{o}C – 60^{o}C) - primers bind to the complementary bases from the 3' end of the template.
3. Extension (72^{o}C)-annealed primers have dNTPs added on via DNA polymerase to produce new dsDNA.

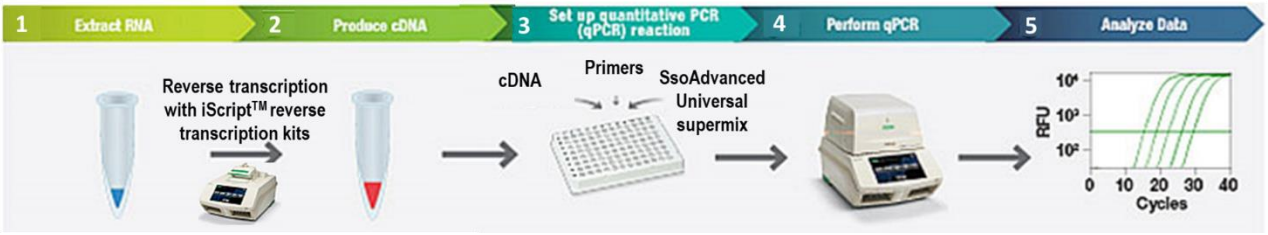

Figure 3.14: **Figure 3.14**: RNA isolation and standardisation, cDNA synthesis and qPCR (Modified from Nagura-Ikeda *et al*., 2020).

For the PCR to occur, the following components are required: DNA template which contains a particular DNA sequence of interest, forward and reverse primer that binds to the 3' ends of the forward and reverse strands of the target sequence, Taq polymerase that catalyzes the formation of new strands of DNA complementary to the sequence of interest, by adding nucleotides to the ends of the annealed primers, $MgCl_2$, the Taq DNA polymerase activity is enhanced by this cofactor, which increases the rate of DNA amplification, deoxynucleotide triphosphates (dNTPs) that bind with the complementary DNA strand by hydrogen bonds and use Taq DNA polymerase to extend the developing DNA strand and lastly the buffer system that maintains optimum pH for PCR reaction to occur (Sarker *et al.*, 2018).

Due to its efficacy in detecting and precisely quantifying the target genes, even at low expression levels, qPCR is widely recognized as the most effective approach for analyzing gene expression modulations (Mohan, 2019). The PCR amplicons created during each cycle of the PCR process can be measured using qPCR. The SYBR Green is a dsDNA binding dye that is used to detect overall fluorescence emission to quantify amplicon amount during PCR. The dye binds to dsDNA's minor groove but not to ssDNA (Nagura-Ikeda *et al*., 2020). A housekeeping gene is utilized to normalize gene levels and concentrations of target DNA expressed with respect to the amount of housekeeping gene (Mohan, 2019).

3.8.2. Protocol

3.8.2.1. RNA isolation and standardisation

The CCM was removed from treated (H2pmen) and untreated (control) flasks, and the flasks were rinsed 1x with PBS. Thereafter, 500 µl of Triazol and 500 µl of PBS was added to each flask. The suspension was transferred to 1.5 ml RNAse/DNA-free microcentrifuge tubes, then stored at -80^{0}C overnight. After the samples were thawed to RT, 100 µl chloroform was added to the samples, which

were thoroughly mixed and centrifuged (12,000 xg, 15 min, 4^0C). The aqueous layer containing the crude RNA was transferred into new 1.5 ml microcentrifuge tubes, and 250 µl isopropanol was added and then incubated at -80^0C overnight. The thawed samples were centrifuged (12,000 x g, 20 min, 4^0C), RNA pellets were washed with cold 75% ethanol (500 µl) and centrifuged (7,400 xg, 15 min, 4^0C). The ethanol was removed, and RNA pellets were then air-dried for about 2 h and, then re-suspended in 15 µl of nuclease-free water. The RNA was quantified using the Nanodrop2000 spectrophotometer (Thermo scientific, Waltham, Massachusetts, USA) and standardized to 1,000 nanogram/microliter (ng/µl).

3.8.2.2. cDNA synthesis

A reaction volume containing 4 µl RNA template, 2 µl 5X iScript™ reaction mix, 0.5 µl iScript reverse transcriptase and nuclease-free water was used to synthesize cDNA (iScript™ cDNA Synthesis kit, Bio-Rad; catalog no 107-8890). Thermocycler conditions were 25^0C for 5 min, 42^0C for 30 min, 85^0C for 5 min, and a final hold at 4^0C. Once the process was complete, 80 µl of nuclease-free water was added to each tube, and samples were stored at -80^0C until use.

3.8.2.3. qPCR

SsoAdvanced™ Universal SYBR® Green Supermix (catalog no. #172-5271, Bio-Rad) was used according to the manufacturer's instructions to analyze gene expression. The mRNA expressions of *GPx1, Nrf-2, Nf-$_k$B, p53, 8-Oxoguanine DNA Glycosylase (OGG1)* were analyzed using specific forward and reverse primers (Table 3.1). The housekeeping gene that was used was *GAPDH*. Reaction volumes consisting of the following were prepared: SYBR green (6.25 µl), forward primer (0.5 µl), reverse primer (0.5 µl), nuclease-free water (3.75 µl) and cDNA template (1000 ng/µl, 1 µl). The 11 µl reaction mix was added to each well, and all reactions were carried out in triplicate.

The samples were amplified using a CFX96 Touch™ Real-Time PCR Detection System (Bio-Rad). The initial denaturation occurred at 95°C (4 min), followed by 40 cycles of denaturation (95°C, 15 second (s)), annealing (40 s; Temperatures – Table 3.1) and extension (72°C, 30 s) followed by a plate read. The relative changes in mRNA expression were determined using the method described by Livak and Schmittgen, where 2-ΔΔCT represents the fold change observed in mRNA expression (Livak and Schmittgen 2001). The expression of the gene of interest was normalized against the house-keeping gene, *GAPDH*, which was amplified simultaneously under the same conditions.

Table 3.1: The gene of interest, annealing temperatures, and primer sequences used for qPCR.

Gene	Annealing Temperature	Primer	Sequence
GPx1	57.4°C	Forward	5'-GACTACACCCAGATGAACGAGC-3'
		Reverse	5'-CCCACCAGGAACTTCTCAAAG-3'
Nrf2	52.6°C	Forward	5'-AGTGGATCTGCCAACTACTC-3'
		Reverse	5'-CATCTACAAACGGGAATGTCTG-3'
Nf-$_k$B	54.8°C	Forward	5'-GACCTGAATGCTGTGCGGC-3'
		Reverse	5'-ATCTTGAGCTCGGCAGTGTT-3'
p53	54.8°C	Forward	5'-CCACCATCCACTACAACTACAT-3'
		Reverse	5'-CAAACACGGACAGGACCC-3'
OGG1	60°C	Forward	5'-GCATCGTACTCTAGCCTCCAC-3'
		Reverse	5'-AGGACTTTGCTCCCTCCAC-3'
GAPDH	61.4°C	Forward	5'-TCCCTGAGCTGAACGGGAAG-3'
		Reverse	5'-GGAGGAGTGGGTGTCGCTGT-3'

4.9. Statistical analysis

All statistical analysis was performed using the GraphPad Prism v 5.0 software (GraphPad Software Inc., La Jolla, CA, USA). For the MTT assay, a non-linear regression was performed. A one-way analysis of variance test with Tukey's post-test comparing all pairs of columns was used for multiple group comparison. Non-linear regression analysis was performed to generate a log inhibition versus normalized response-variable slope from which the IC_{20} and IC_{50} were derived. The unpaired student *t*-test was performed with Welch's correction to determine statistical significance for subsequent assays. Data was expressed as mean ± standard deviation. Data was considered statistically significant with a 95% confidence interval and p-value ≤ 0.05.

CHAPTER 4: RESULTS

4.1. Cytotoxicity

The MTT and LDH assays were used to determine the cytotoxicity of H2pmen in HepG2 cells. A dose-response curve generated from serially diluted H2pmen concentrations (0–1000 μM) over a 24 h period was used to determine the IC_{50} of 209 μM and IC_{20} of 71 μM. At 25 μM (89.67±5.364, p=0.1939) and 50 μM (89.00±6.506, p=0.2330) the cell viability decreased to about 90% and subsequently at a 100 μM (76.33±3.180, p=0.0176) it decreased to 76%, at 250 μM (36.67±5.783, p=0.0082) and 500 μM (32.33±2.333, p=0.0012) was decreased to less than 40% with a further decrease to less than 10% at 750 μM (9.667±0.3333, p<0.0001) and 1000 μM (7.333±1.453, p=0.0002) (Figure 4.1A). In the LDH assay, HepG2 cells indicated a significant 1.55-fold increase in LDH levels at IC_{20} (0.1310±0.006000 OD, p=0.0055) and another significant increase by 2.02-fold at IC_{50} (0.1710±0.008000 OD, p=0.0029) compared to the untreated control (0.0845±0.0005000) (Figure 4.1B).

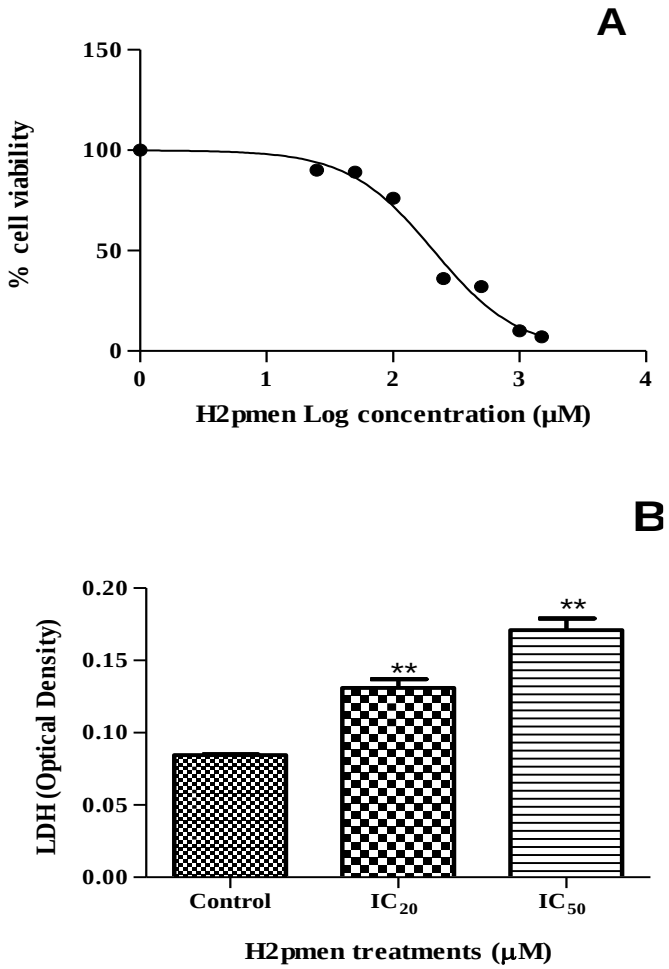

Figure 4.1:The effect of H2pmen in HepG2 cells viability. (A), The H2pmen compound induced a dose-dependent decrease in HepG2 cell viability after 24 h treatment with higher concentrations showing high reduction in cell viability. **(B)** The LDH levels were also significantly increased in HepG2 cells in both IC_{20} and IC_{50} after 24 h treatment, OD: optical density. (*,**,***$p \leq 0.05$ relative to the control), unpaired student *t*-test with Welch's correction.

4.2. Metabolism

The CYP3A4 activity assay was used to quantify the levels of CYP3A4 to identify if H2pmen was metabolized in HepG2 cells. A significant increase of CYP3A4 by 1.78-fold was measured at IC_{20} (1589±115 RLU, p=0.0109) and another significant increase by 2.25-fold at IC_{50} (2005±75.01 RLU, p=0.0002) was measured relative to the control (892.0±54 RLU) after H2pmen treatment (Figure 4.2).

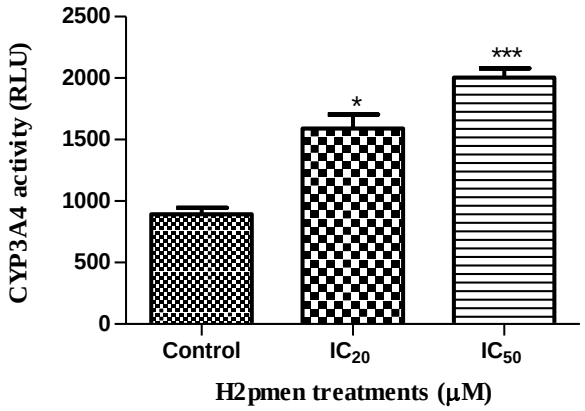

Figure 4.2: The metabolism of H2pmen in HepG2 cells. The CYP3A4 levels were significantly increased in HepG2 cells at both IC_{20} and IC_{50} after 24 h treatment, RLU: relative light units. (*,***$p \leq 0{,}05$ relative to the control) unpaired student *t*-test with Welch's correction.

4.3. Mitochondrial Integrity

ATP assay was used to measure cell viability and mitochondrial integrity after HepG2 cells were treated with H2pmen. H2pmen decreased ATP levels in HepG2 cells to 0.88-fold at IC_{20} (13670000±152753 RLU, p=0.0946) and significantly decreased ATP levels to 0.37-fold at IC_{50} (57770000±285311 RLU, p=0.0044) compared to the control (15600000±1100000 RLU) [Figure 4.3]. The ratio of JC-10 red and green was used in this study to determine the $\Delta\Psi m$ changes in HepG2 cells. After H2pmen treatment, HepG2 cells indicated a significant decrease to 0.87-fold at IC_{20} (0.06600±0.0008931 RFU, p=0.0023) and a significant decrease to 0.86-fold at IC_{50} (0.06539±0.001067 RLU, p=0.0022) in JC-10 levels compared to the control (0.07615±0.001561 RFU) [Figure 4.3B].

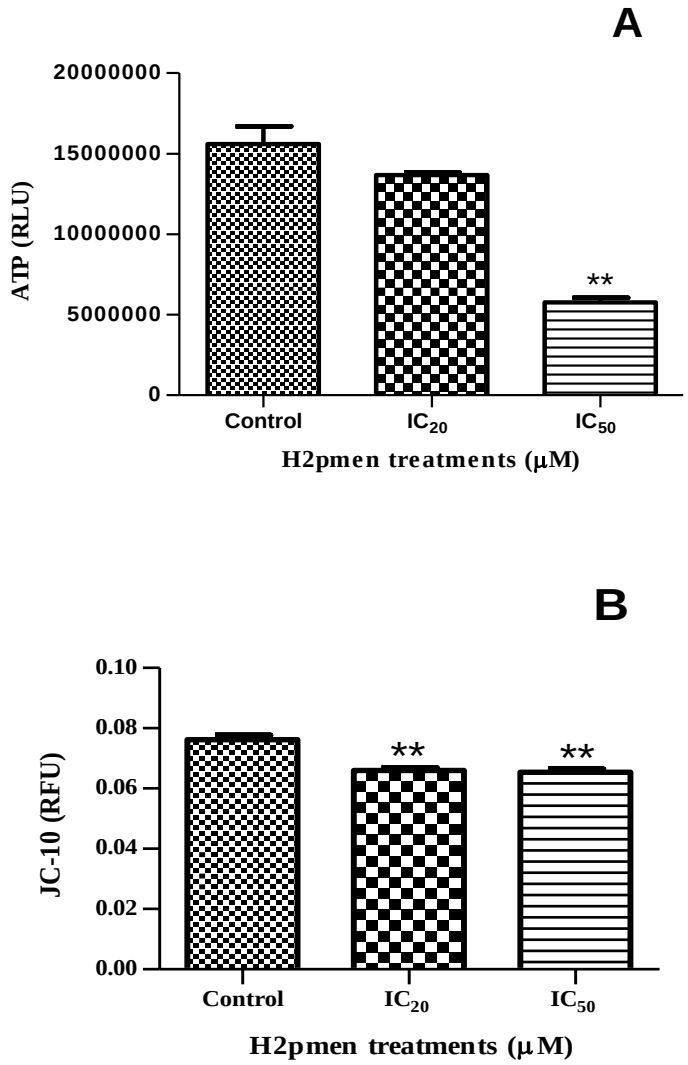

Figure 4.3: **The effects of H2pmen in HepG2 cells mitochondrial integrity.** (**A**) The ATP levels were decreased in HepG2 cells at IC_{20} and IC_{50} after 24 h treatment, RLU: relative light units. (**B**) The JC-10 levels were significantly decreased in HepG2 cells at both the IC_{20} and IC_{50}, RFU: relative fold units. (**$p \leq 0.05$ relative to control) unpaired student *t*-test with Welch's correction.

4.4. ROS-associated Macromolecule Damage

Lipid peroxidation was assessed using TBARS assay to quantify MDA levels in HepG2 cells. H2pmen induced a significant increase in MDA concentration by 1.19-fold at IC_{20} (0.07906±0.003701 µM, p =0.0240) and 1.32-fold increase at IC_{50} (0.08761±0.009792 µM, p= 0.0715) relative to the control (0.06624±0.003701 µM) [Figure 4.4A]. The *OGG1* gene expression was quantified using PCR to assess the oxidative DNA damage induced by H2pmen in HepG2 cells. A significant increase of 1.32-fold at the IC_{20} (1.320±0.02000 RFC, p=0.0013) was measured, and another significant increase of 0.88-fold at the IC_{50} (1.233±0.08737 RFC, p=0.0438) was also recorded relative to the control (1.000±0.000 RFC) [Figure 4.4B].

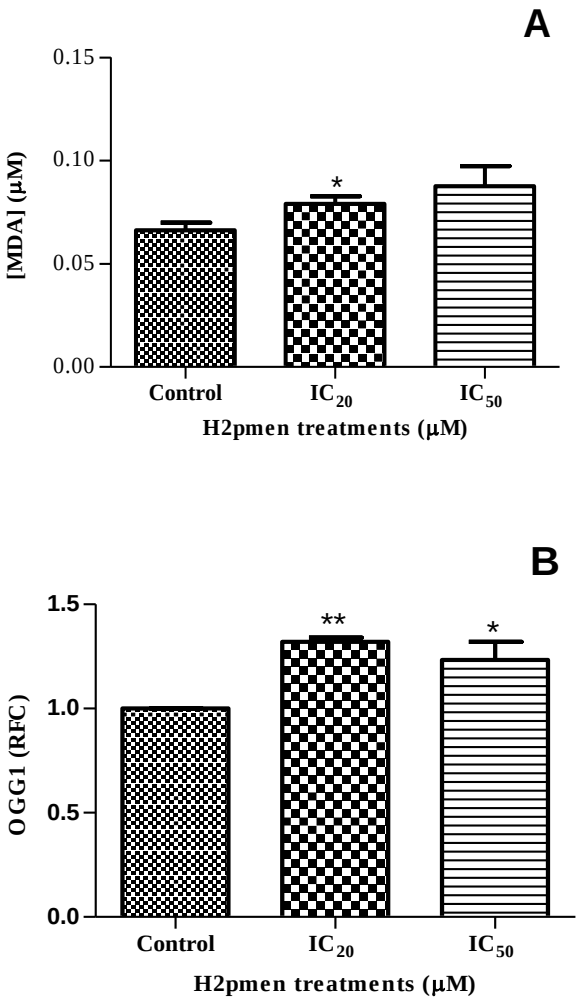

Figure 4.4: The effects of H2pmen in ROS-associated macromolecule damage in HepG2 cells. **(A)** The MDA concentration was significantly increased in HepG2 cells at IC20 and IC50 after 24h treatment. (**B**) The OGG1 gene expression was significantly increased at both the IC20 and IC50 in HepG2 cells RFC: Relative fold change. (*, **p≤0.05 compared to the control) unpaired student t-test with Welch's correction.

4.5. RNS Production

The *NF-κB* gene expression was assessed using PCR to determine the stimulation of iNOS and a 10.66-fold significant increase at the IC_{20} (9.980±0.5091 RFC, p=0.0255) was measured and at IC_{50} (3.265±0.4313 RFC, p=0.0852), there was an increase by a 0.38-fold relative to the control (1.000±0.000 RFC) [Figure 4.5A]. The iNOS protein expression was assessed using western blot to quantify NOS production. The significant increase by 2.35-fold at the IC_{20} (0.3467±0.02402 RBD, p=0.0050) and also increased by 1.97-fold at the IC_{50} (0.2497±0.01860 RBD, p=0.0841) compared to the control (0.1484±0.004297 RBD) [Figure 4.5B]. Nitrate and nitrite concentrations were quantified using NOS Assay. In HepG2 cells, there was an insignificant increase in nitrate and nitrate

concentration, by 1.23-fold at IC_{20} (3.524±0.2429 µM, p=0.1381) and by 1.32-fold at IC_{50} (3.254±0.2429 µM, p=0.1080) relative to the control (2.124±0.2367 µM) [Figure 4.5C].

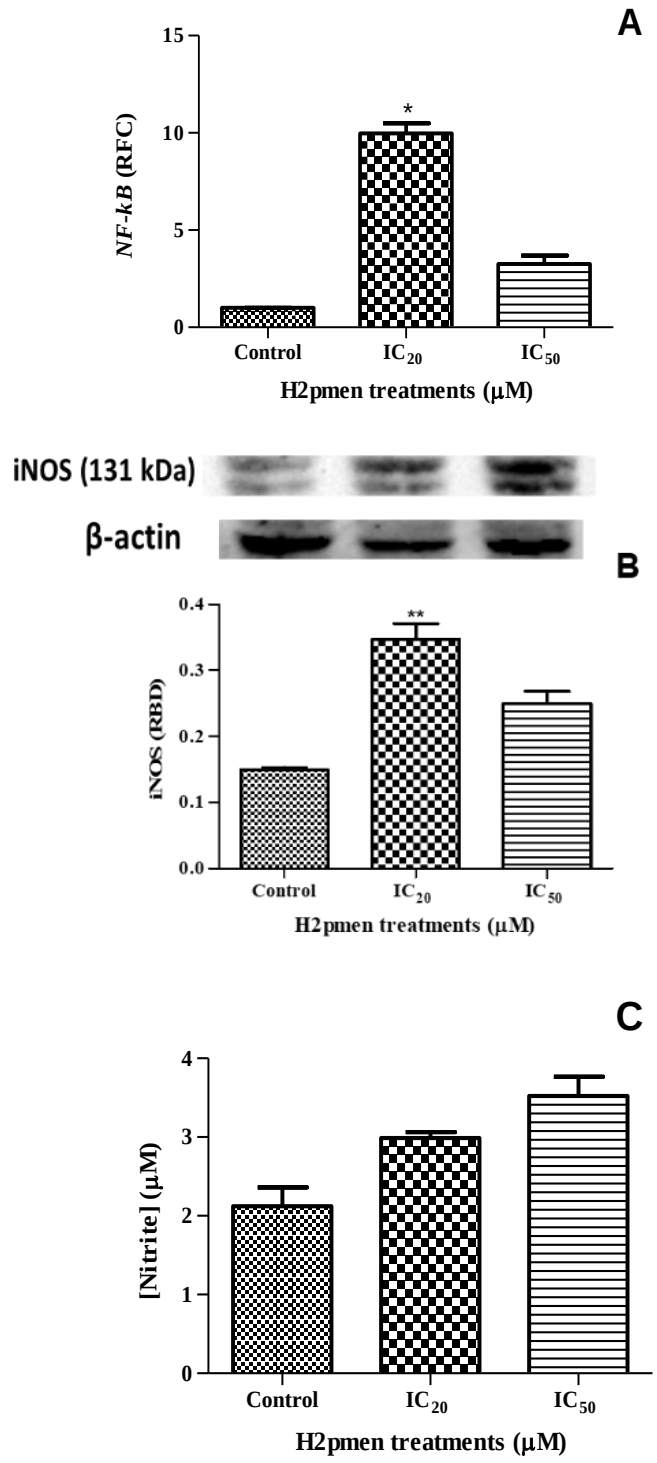

Figure 4.5: The effects of H2pmen in RNS production in HepG2 cells. (A) The *NF-κB* increased significantly at the IC_{20} and also increased at the IC_{50}, RFC: relative fold change. **(B)**The iNOS was significantly increased at the IC_{20} and also increased at the IC_{50} in HepG2 cells, RBD: relative band density. **(C)** Nitrite/nitrate concentration was increased in HepG2 cells at both the IC_{20} and IC_{50} treatment. (*, **$p \leq 0.05$ compared to the control) unpaired student *t*-test with Welch's correction.

4.6. Antioxidant defense

The antioxidant activity of SOD2 was quantified using western blot. The SOD2 protein expression was significantly decreased to 0.79-fold at the IC_{20} (0.5851±0.01336 RBD, p=0.0021) and to 0.82-fold at the IC_{50} (0.6060±0.01450 RBD, p=0.0034) compared to the control (0.7385±0.02281 RBD) [Figure 4.6A]. The qPCR was used to assess the antioxidant activity of *GPx1*. The H2pmen induced a 0.54-fold and 0.37-fold upregulation of *GPx1* gene expression in HepG2 cells at the IC_{20} (5.403±0.7778 RFC, p=0.0102) and at the IC_{50} (1.900±0.4969 RFC, p=0.0884) compared to the control (1.000±0.000 RFC) [Figure 4.6B]. The GSH assay was used to detect the antioxidant activity of GSH. The HepG2 cells indicated a 0.44-fold decrease in GSH levels at IC_{20} (875782±154338 RLU, p=0.1247) and a 0.30-fold significant decrease at IC_{50} (459822±10026RLU, p=0.0042) compared to the control (1526000±119115 RLU) after H2pmen treatment (Figure 4.6C). The antioxidant activity of *Nrf2* was also quantified using qPCR. There was a 2.70-fold increase in *Nrf2* at the IC_{20} (2.040±0.2263 RFC, p=0.0972) and a significant 0.59-fold increase at the IC_{50} (1.600±0.1100 RFC, p=0.0110) compared to the control (1.000±.0.000 RFC) [Figure 4.6D].

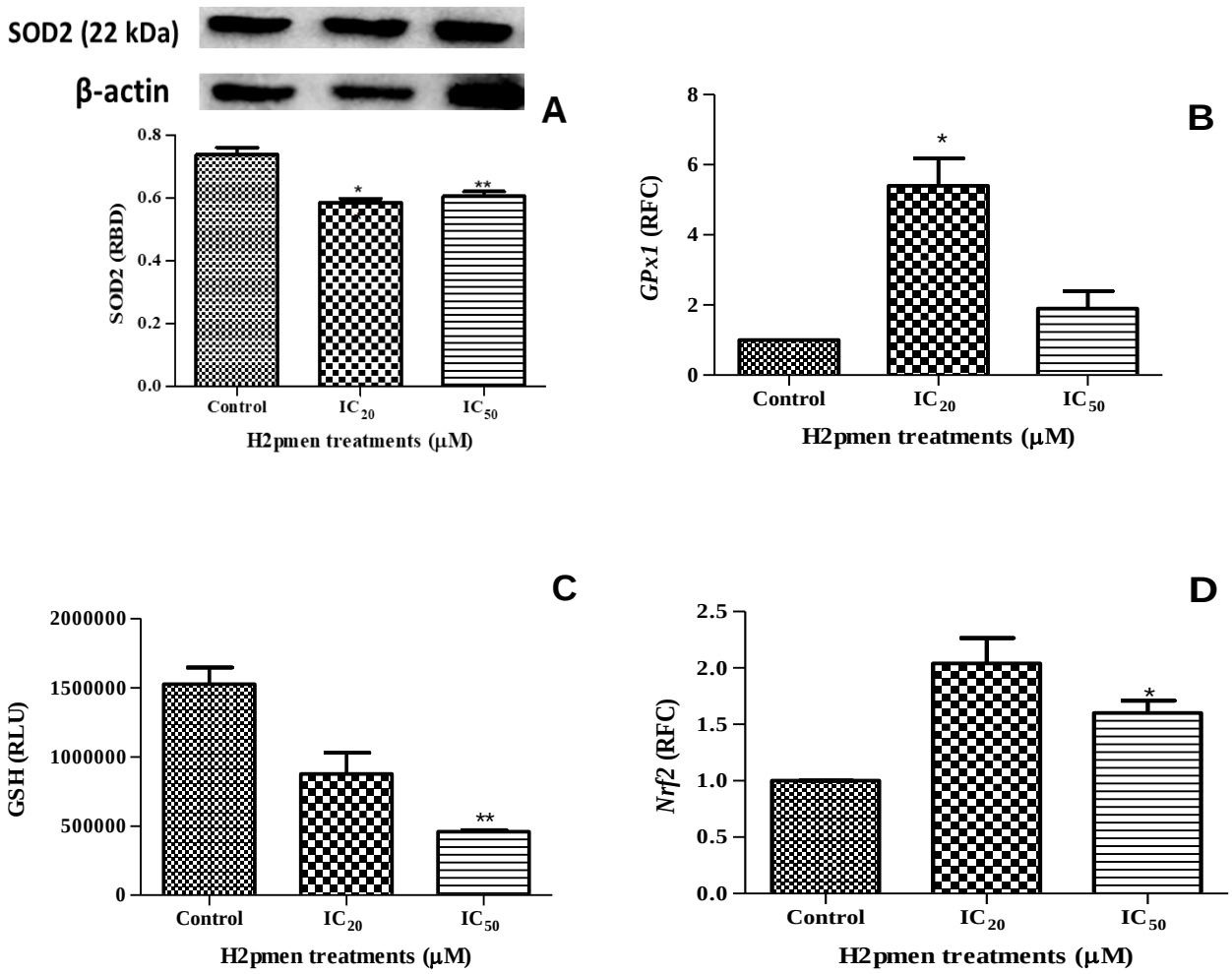

Figure 4.6: The effects of H2pmen in the antioxidant response in HepG2 cells. (A) A significant decrease in SOD2 at the IC_{20} and IC_{50} was obtained, RBD: Relative band density**. (B)** A significant increase in *GPx1* at the IC_{20} and also an increased at the IC_{50} in HepG2 cells was obtained, RFC: Relative fold change. **(C)** The levels of GSH were decreased in HepG2 cells at both the IC_{20} and IC_{50} after 24h treatment, RLU: relative light units. (**D**) The *Nrf2* increased at the IC_{20} and also significantly increased at the IC_{50}, RFC: Relative fold change. (*, **$p \leq 0.05$ compared to the control) unpaired student *t*-test with Welch's correction.

4.7. Initiation of Apoptosis

Western blot was used to quantify the activity of caspase-2 in HepG2 cells. There was a significant increase in caspase-2 activity in HepG2 cells at the IC_{20} (0.1559±0.004485 RBD, p=0.0006) by 3.14-fold and at the IC_{50} (0.1385±0.006295 RBD, p=0.0017) by 2.81-fold, relative to the control (0.04860±0.001428 RBD) [Figure 4.7A]. The activities of caspase-8 and -9 were determined via luminometry to see if apoptosis was initiated in HepG2 cells. There was a decrease to 0.85-fold in caspase-8 activity at the IC_{20} (2071000±159870 RLU, p=0.0521) and to 0.80-fold decrease at IC_{50} (1944000±38665 RLU, p=0.0435) relative to the control (2.423000±174605 RLU) [Figure 4.7B]. There was a decrease in caspase-9 activity to 0.87-fold at the IC_{20} (4244000±395880 RLU, p=0.0986) and a 1.06-fold increase at the IC_{50} (5178000±38630RLU, p=0.1973) relative to the control (4891000±258585 RLU) [Figure 4.7C]. The gene expression of *p53* was determined using PCR. The H2pmen significantly upregulated *p53* by 8.19-fold at the IC_{20} (8.190±0.6802 RFC, p=0.0030) and also caused upregulation at the IC_{50} (2.183±0.6730 RFC, p=0.0931) by 0.27-fold compared to the control (1.000±0000 RFC) [Figure 4.7D]. Western blot was used to quantify the protein expression of Bax. The H2pmen significantly increased Bax by 1.32-fold at the IC_{20} (6.286±0.2447 RBD, p=0.0075) and by 1.40-fold at the IC_{50} (6.538±0.06724 RBD, p< 0.0001) compared to the control (4.539±0.09719 RBD) [Figure 4.7E].

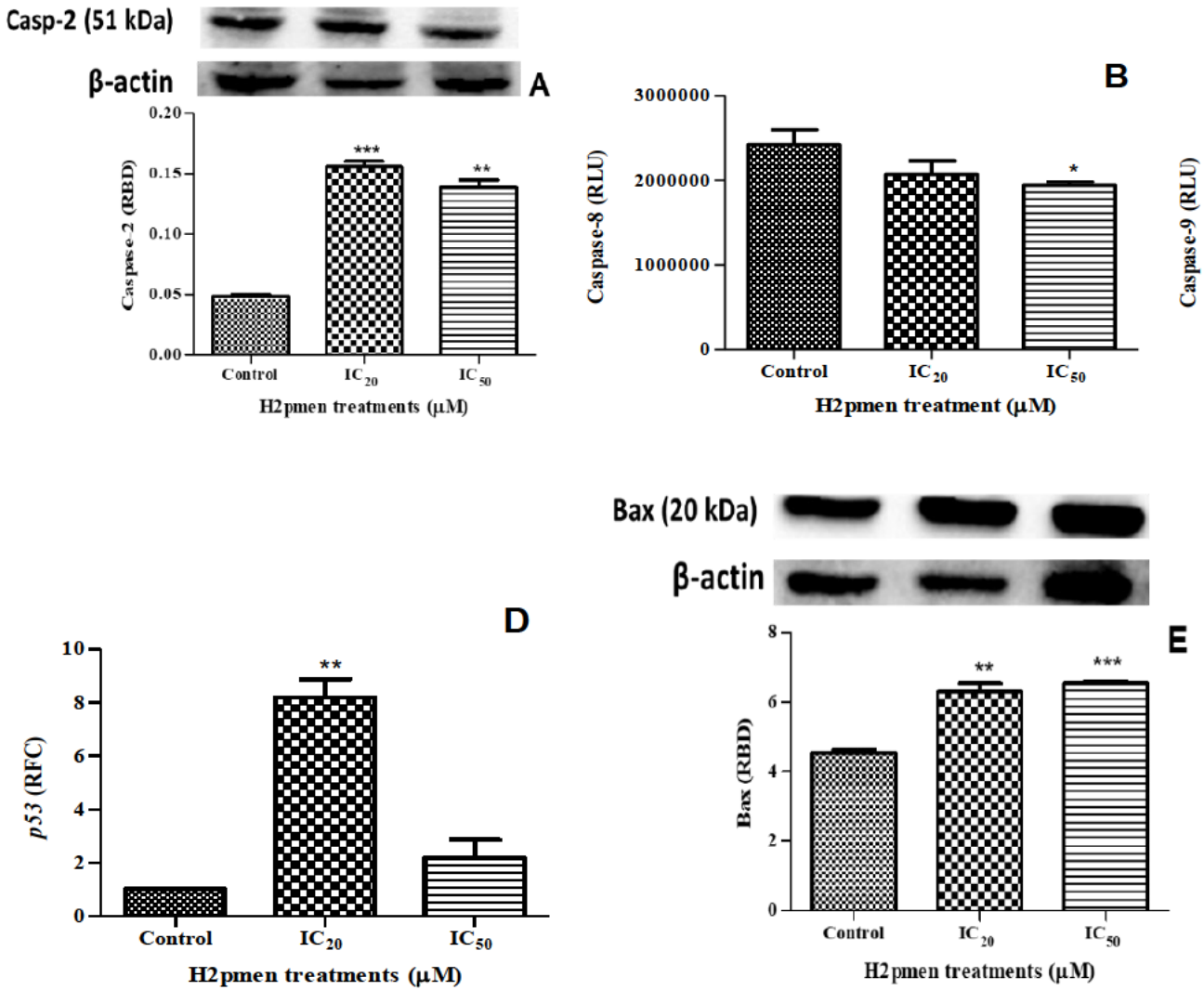

Figure 4.7: The effects of H2pmen in the apoptotic pathway initiation in HepG2 cells. (A) Caspase-2 was significantly upregulated at the IC_{20} and IC_{50}, RBD: relative band density. **(B)** There was a decrease in caspase-8 activity at both the IC_{20} and the IC_{50}, RLU: relative lights units. (**C**) In caspase-9, there was a decrease at the IC_{20} and a slight increase at the IC_{50}, RLU: relative lights units. (**D**) The *p53* was significantly increased at the IC_{20} and also increased at the IC_{50} in HepG2 cells, RFC: relative fold change. (**E**) Bax was significantly upregulated at the IC_{20} and IC_{50}, RBD: relative band density. (*, **, ***$p \leq 0.05$ compared to the control) unpaired student *t*-test with Welch's correction.

4.8. Execution of Apoptosis

The pSTAT3/STAT3 ratio was assessed using western blot. The ratio was determined by dividing each band measurement value of p-STAT3 by the average band measurement of STAT3 for each treatment. The H2pmen caused a significant 1.70-fold increase in pSTAT3/STAT3 ratio at the IC_{20} (0.04155±0.001110 RBD, p=0.0014) and another significant 1.51-fold increase at the IC_{50} (0.03702±0.0006189 RBD, p=0.0009) relative to the control (0.02451±0.0001566 RBD) [Figure 4.8A]. The activity of caspase-3/7 was quantified using luminometry. There was a 1.78-fold increase in caspase-3/7 activity at IC_{20} (3985000±77645 RLU, p=0.0046) and 2.40-fold increase at IC_{50} (5376000±234775 RLU, p=0.0004) relative to the control (2.243000±191270 RLU) [Figure 4.8B]. Annexin V assay was used to quantify the level of annexin in HepG2 cells. An increase in annexin by 2.46-fold was recorded at IC_{20} (22392±9589 RLU, p=0.1574) and a huge increase of 17.37-fold at IC_{50} (194115±50914 RLU, p=0.1226) was measured relative to the control (9105±4032 RLU) [Figure 4.8C]. The PARP1 protein expression was significantly assessed using western blot and it increased by 2.31-fold at the IC_{20} (0.8136±0.04215 RBD, p=0.0028) and also significantly increased by 2.02-fold at the IC_{50} (0.7129±0.02268 RBD, p=0.0014) compared to the control (0.3526±0.004689 RBD) [Figure 4.8D].

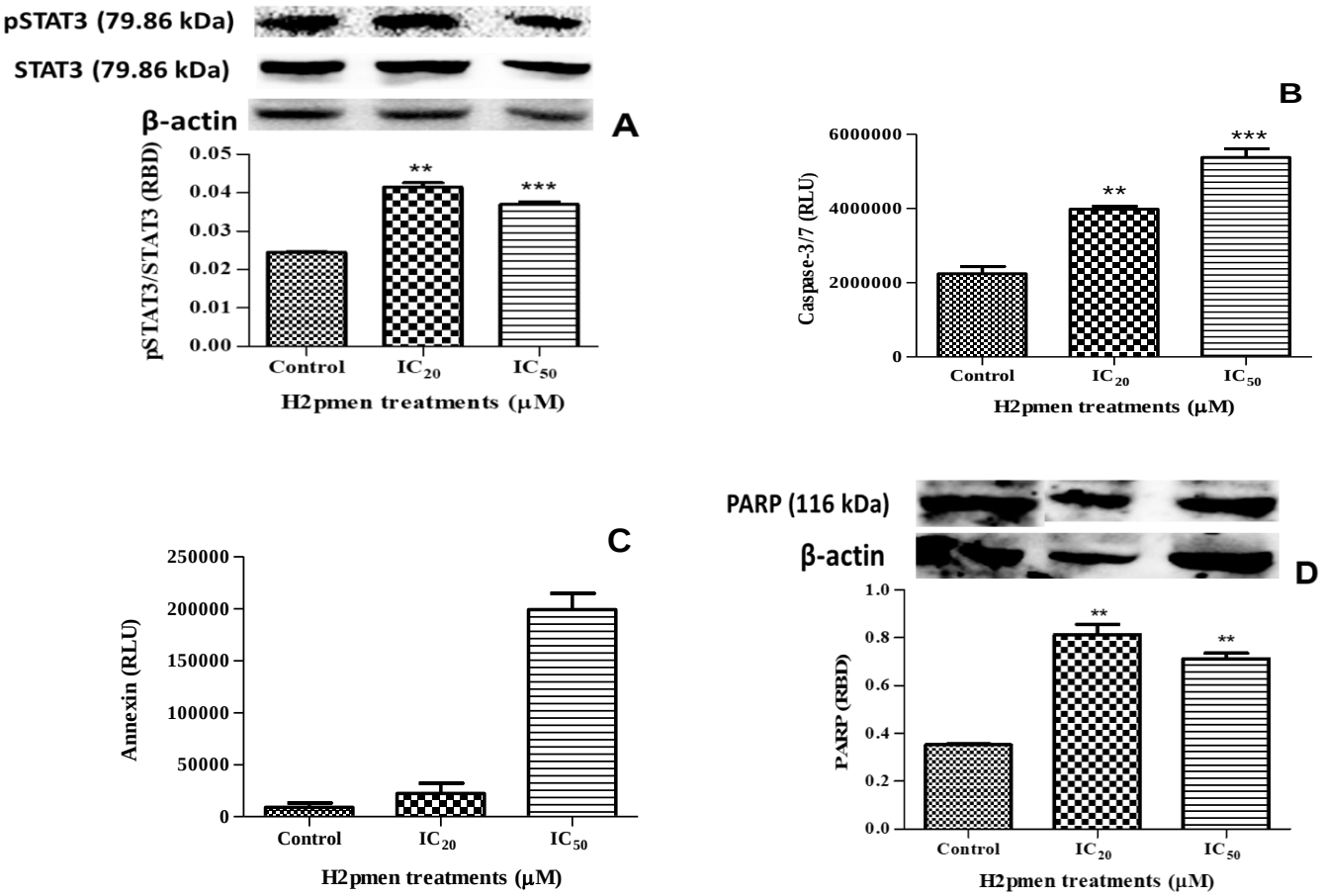

Figure 4.8: The effects of H2pmen in the apoptotic pathway execution in HepG2 cells. (A) There was a significant upregulation of in pSTAT3/STAT3 ratio at both the IC_{20} and IC_{50}, RBD: Relative band density. **(B)** The H2pmen induced a significant increase in caspase-3/7 at IC_{20} and IC_{50}, RLU: Relative lights units. **(C)** Annexin levels were increased at both IC_{20} and IC_{50} after 24 h H2pmen treatment. RLU: Relative Light Unit (**D**) The PARP1 protein expression was significantly upregulated at the IC_{20} and IC_{50} in HepG2 cells, RBD: Relative band density. (*, **, ***$p \leq 0.05$ compared to the control) unpaired student *t*-test with Welch's correction.

CHAPTER 5: DISCUSSION

The global incidence and mortality of patients living with cancer has increased (Sun *et al*., 2021). Currently, liver cancer is one of the leading causes of cancer-related deaths worldwide, accounting for 8.3% of cancer-related deaths in 2020 (Sung *et al*., 2021, Ferlay *et al*., 2021). Several cancer therapeutics have already been discovered and are being used to treat liver cancer. Treatment strategies include surgery, radiation and chemotherapy (Huang, 2021). However, most of them are associated with debilitating side effects such as nephrotoxicity, which reduces the effectiveness of the treatment and affects quality of life and overall survival of patients (Santos *et al*., 2020). Most liver cancer patients succumb to the disease within one year of diagnosis (Okeke *et al*., 2020). Therefore, there is an unmet need for innovative cancer therapies that cause less or no damage to the body's cells, while potently targeting and eradicating cancer cells. The tetradentate ligand, H2pmen, was recently discovered to form stable complexes with Fe, Cr, Cu(II) and Zn(II). It has been shown to be a potentially effective reagent for metal chelation (Popov *et al*., 2019). Chelating agents bind to toxic metal ions and form complex structures that can be easily excreted from the body, removing them from intracellular and extracellular spaces (Sharma and Pandita, 2020). However, a chelator may occasionally expose the metal to the biological environment, thus increasing its toxicity (Sharma and Pandita, 2020). The biochemical effects underlying the mechanism of H2pmen cytotoxicity on HepG2 cells has not yet been investigated. Since Jurisevic and colleagues (2018) showed that the chelator ethylenediamine to caused apoptosis in 40% of MCF-7 cells, it was hypothesised that H2pmen will induce cytotoxic effects on HepG2 liver cancer cells (Jurisevic *et al.*, 2018).

Organic molecules absorbed from the intestine undergo a complex metabolic transformation in the liver. Compared to the parent compounds, the metabolites of these reactions may show increased or decreased toxicity (Chen *et al*., 2021). The CYP3A4 protein is a member of the CYP450 family of enzymes that is prominently located in the liver and small intestine; this inducible enzyme plays a crucial role in drug metabolism and metabolises more than 50% of all clinically used medications (Zhou *et al*., 2007, Sevrioukova and Poulos, 2017). In this study, the increased activity of CYP3A4 (Figure 4.2) suggests that its induction by H2pmen in HepG2 cells may capacitate the metabolism of potentially cytotoxic drugs in the liver (Zhou *et al*., 2007, Sevrioukova and Poulos, 2017). This has important consequences, as it may result in the metabolic inactivation of therapeutic drugs or bioactivation of xenobiotics which will require phase 2 detoxification involving GSH and glutathione-S-transferase (Forman and Zhang, 2021). Hofman *et al.* (2021) showed that CYP3A4

may confer pharmacokinetic resistance to the chemotherapeutic docetaxel by decreasing its antiproliferative activity; however, vincristine and paclitaxel were not affected by CYP3A4 (Hofman *et al.*, 2021). Similarly, induced CYP3A4 may not interfere with H2pmen cytotoxicity.

The cytotoxicity of a compound provides an indication of cellular or metabolic changes associated with cell viability. In this study, the MTT assay showed that H2pmen caused a dose-dependent decrease in cellular metabolic activity and viability of HepG2 cells (Figure 4.1A) suggesting that H2pmen may have inhibited succinate dehydrogenase activity. Succinate dehydrogenase is a mitochondrial enzyme that forms part of complex II of the ETC and uses NADH as a source of reducing power cells to convert the tetrazolium salt MTT into a water-insoluble purple formazan crystal in metabolically active cells (Wang *et al*., 2010, Abdul *et al*., 2016, Rai *et al*., 2018). An early sign of declining cell viability is the interruption of the ETC, which is commonly followed by a reduction in ATP production (Feno *et al*., 2019).

The ATP is a source of energy of all living cells and is involved in many critical biochemical reactions, thus ATP is frequently utilized as a metric for determining whether or not a cell is viable (Bajerski *et al*., 2018). The decreased cell viability in this study (Figure 4.1B) correlated with decreased ATP concentration (Figure 4.3A) and ΔΨm (Figure 4.3B), possibly indicating the impaired functioning of the mitochondrial respiratory chain. Disruption of the mitochondrial respiratory chain results in disruption of the proton gradient within the mitochondrial membrane, which is required in the ATPase complex V for ATP production (Brandy and Murphy 1987, Hashimoto *et al*., 2019). Complex I, II (succinate dehydrogenase) and III of the ETC contain iron-sulfur (FeS) clusters, while the haem-containing cytochromes are also dependent on Fe^{2+} for their function in the ETC (Abdul *et al*., 2016). Therefore, Fe^{2+} chelation by metal chelators such as H2pmen may inhibit these enzymes and disrupt the ETC, contributing to the disrupted flow of electrons and dissipation of the proton gradient generated by complex I, III and IV (Feno *et al*., 2019). Chelation of Fe^{2+} in cytochrome *c* may lead to further disruption of the ETC, resulting in slow movement of electrons and uncoupling of the respiratory chain from ATP synthesis, consequently decreasing ATP (Figure 4.3A) (Yoon *et al*., 2003, Hoes *et al*., 2018).

The ΔΨm is a crucial measure of mitochondrial activity and an essential component in the process of energy generation during oxidative phosphorylation; thus the ETC and oxidative phosphorylation

mechanism that drives ATP synthesis is reflected in ΔΨm (Zorova *et al.*, 2018). A prolonged decrease in ΔΨm as seen in this study (Figure 4.3B) may result in a decrease in cell viability (Sivandzade *et al.*, 2019). A study conducted by Cordier (2021) suggests that this might be attributed to reduced metabolic activity (Figure 4.1A), which could have resulted in a drop in reducing equivalents and ATP generation (Cordier *et al*., 2021) (Figure 4.3A). These findings are similar to those obtained by Satyo and colleagues (2020), where the metal chelator di(2-picolyl) amine induced a dose-dependent decrease in cell viability and a reduction in ATP production (Satyo *et al*., 2020). Similar research has found that a decrease in cell viability and ATP generation is typically coupled with an increase in ROS, which eventually leads to oxidative stress (Gandin *et al.*, 2018).

Mitochondria are the main producer of ROS through oxidative phosphorylation and are also a highly susceptible target for ROS molecules and their damaging effects; ROS such as O_2^- and H_2O_2 may also be formed from other reactions, notably xanthine oxidase (Kelley *et al.*, 2010, Gilardini Montani *et al*., 2019). When the antioxidant system is overburdened due to an excess of ROS, oxidative stress occurs (Gandin *et al.*, 2018). Lipid peroxidation is a known biomarker of oxidative stress that arises due to the chemical reaction between fatty acids and ROS (O_2^-, H_2O_2 and $^{\bullet}OH$) leading to compromised cell membrane integrity and ultimately resulting in irreversible cellular damage (Su *et al*., 2019). Since the plasma membrane integrity is compromised during the lipid peroxidation process, cytoplasmic contents such as LDH may leach out of the cell (Kumar *et al*., 2018, Riss *et al*., 2019). Increased LDH leakage in this study (Figure 4.1B) indicate that the membrane assembly was disrupted, and the integrity was compromised, which correlates to an increase in ROS and RNS, and a reduction in antioxidants SOD2 (Figure 4.6A) and GSH (Figure 4.6C). The increased lipid peroxidation in this study (Figure 4.4A) suggests that H2pmen has the potential to increase ROS production and induce oxidative stress within HepG2 cells; the potential of H2pmen to chelate Fe^{2+} in the mitochondrial ETC may increase ROS production by complexes I, III and IV (Feno *et al*., 2019). In addition, chelation of metal ions required for the Fenton reaction may also be chelated, suggesting that lipid peroxidation was associated with O_2^- and H_2O_2. Other metal chelators including salicylaldehyde isonicotinoyl hydrazine and di(2-picolyl)amine produced similar results, inducing increased ROS in HepG2 and Hek293 cells respectively (Caro *et al*., 2015, Satyo *et al*., 2020).

The literature has shown that a high concentration of ROS such as O_2^- condenses with NO to form peroxynitrite ($ONOO^-$), a reactive RNS intermediate and extremely toxic oxidant (Satyo *et al*., 2020).

Cancer and other inflammatory diseases are associated with sustained high levels of NO and O_2^- which cause oxidative stress (Islam *et al*., 2019). In this study, H2pmen caused a significant increase in iNOS (Figure 4.5B) and downregulation of SOD2 (Figure 4.6A) protein synthesis implying that more NO and O_2^- was available for the formation of RNS (Figure 4.5C). This may explain the increased RNS production in this study that was much more pronounced than previously observed for di(2-picolyl)amine in Hek293 cells and 1,4,7-triazacyclononane in HepG2 cells (Mcoyi *et al.*, 2020, Satyo *et al.*, 2020). In a manner similar to protein oxidation by ROS to form protein carbonyls, nitrosylation of protein by RNS occurs mainly at tyrosine residues. This may influence the functioning of key molecules in metabolic pathways. Indeed, NO has been shown to activate the canonical NF-κB pathway in rat myoblasts at low concentrations, while the noncanonical pathway is activated by $ONOO^-$ in skeletal myocytes (Davidson *et al.*, 2021).

The NF-κB pathway plays a crucial role in response to oxidative stress, demonstrating both anti- and pro-oxidant potential (Flaherty *et al*., 2017, Liu *et al*., 2020). Oxidative stress, cytokines, free radicals, heavy metals, UV irradiation and oxidized low-density lipoprotein (LDL) are all triggers that activate the NF-κB pathway (Liu *et al*., 2020). The elevated transcriptional activity of *NF-κB* results in increased gene transcription and protein translation of pro-inflammatory and anti-inflammatory proteins, including iNOS (Lee *et al.*, 2019). It is thus not surprising that *NF-κB* gene expression was increased in this study (Figure 4.5A), and was associated with increased transcription and translation of iNOS (Figure 4.5B) leading to increased generation of RNS (Figure 4.5C) (Lee *et al.*, 2019). Thus, H2pmen demonstrated the potential to upregulate oxidative and nitrosative stress in HepG2 cells, causing the mitochondrial membrane and its functions to be disrupted (Figures 4.3A, B).

The Nrf2 protein regulates the gene expression of various cytoprotective proteins in response to oxidative stress, including antioxidant, detoxification enzymes and proteins that promote repair or elimination of damaged macromolecules, thus allowing the cells to adapt and survive in stressful conditions (Cho and Kleeberger, 2020). Normally, Nrf2 is subjected to proteasomal degradation due to its attachment to Keap1, but Keap1 oxidation during oxidative stress releases Nrf2 to the nucleus to promote the transcription of many genes (Ulasov *et al*., 2021). In this study, acute exposure to H2pmen resulted in an upregulation in Nrf2 (Figure 4.6D), thus the enzymes responsible for GSH synthesis and those related to GSH utilization would be transcriptionally upregulated by Nrf2 (Cho and Kleeberger, 2020). In this study, treatment with H2pmen resulted in a considerable reduction in GSH activity (Figure 4.6C). Depletion of GSH, a well-known marker of oxidative stress, may occur

following its utilisation in phase 2 biotransformation reactions catalysed by glutathione-S-transferase, failure to reduce GSSG to GSH if glutathione reductase or NADPH are deficient, conversion of O_2^- to H_2O_2 and repair of hydroperoxides (Grandn *et al*., 2018, Siauciunaite *et al*., 2019). Since decreased SOD2 (Figure 4.6A) lowers H_2O_2 availability, this finding suggests that the associated accumulated O_2^- caused lipid peroxidation (Figure 4.4A) in HepG2 cells; alternate sources of H_2O_2 may also be implicated in lipid peroxidation. When repair of oxidative damage induced by high levels of ROS and RNS is compromised, the mitochondrial membrane and its functions may be disrupted (Figures 4.3A, B), and lipid peroxidation may result (Figure 4.4A), as observed in this study and other studies (Caro *et al*., 2015, Satyo *et al*., 2020).

Both GSH and GPx1 are involved in the detoxification of lipid hydroperoxides, and the conversion of H_2O_2 to H_2O to limit its harmful side effects; H_2O_2 may be formed from O_2^- by antioxidant enzyme SOD2 (Dikalova *et al*., 2017, Gandin *et al*., 2018). However, a reduction of SOD2 expression (Figure 4.6A) possibly due to chelation of the Mn by H2pmen suggests a consequent increase in O_2^-, while H_2O_2 will decrease. However, H_2O_2 is also formed from other reactions, including xanthine oxidase (Kelley *et al*., 2010). In this study, protein expression of *GPx1* was upregulated (Figure 4.6B), implying that detoxification of H_2O_2 to H_2O should have occurred in the H2pmen-treated cells. However, low levels of GSH sustained H_2O_2 which together with the increased O_2^- facilitated the rise in lipid peroxidation (Figure 4.4A); the study assumes that lipid peroxidation was not affected by the potent OH radical due to chelation of Fenton reaction metals by H2pmen (Caro *et al*., 2015, Satyo *et al*., 2020).

The persistence of free radicals may also induce oxidative DNA damage in cells; with some studies suggesting that ROS such as H_2O_2 induces both single and double strand breaks in DNA (Shi *et al*., 2021). Guanine bases are particularly susceptible to oxidation forming the potentially mutagenic 8-oxoguanine (8-oxoG) (Boiteux and Radicella, 2000, Corella *et al*., 2018). The DNA repair enzyme 8-oxoguanine DNA glycosylase-1 (OGG1) is responsible for executing the excision of 8-oxoG (Boiteux and Radicella, 2000, Corella *et al*., 2018). Since OGG1 is also found in mitochondria and oxidative damage in mitochondrial DNA (mtDNA) is predominantly repaired by the base excision repair (BER) mechanism, this crucial BER enzyme plays a crucial role in mtDNA damage repair by excising 8-oxoG from the mitochondrial genome (Cheng *et al*., 2013). A significant upregulation of *OGG1* gene expression was observed in this study (Figure 4.4B), indicating that H2pmen induced oxidative DNA damage in HepG2 cells at both the IC_{20} and IC_{50}, so the increase in *OGG1* gene expression will lead to the upregulation of *OGG1* protein to repair the damage induced. This

corresponds with the results from the study that Cragg and colleagues conducted (1998), where they found that 1,2-dimethyl-3-hydroxypyrid-4-one, a metal chelator caused oxidative DNA damage in HepG2 cells (Cragg *et al.*, 1998).

Literature suggests several proteins that are involved in DNA repair, including Nrf2 that plays a crucial role in repairing oxidative DNA damage (Ulasov *et al*., 2021) and PARP1 for repair of strand breaks (Hafner *et al.*, 2019). In this study, acute exposure to H2pmen resulted in an upregulation in *Nrf2* (Figure 4.6D) and PARP1 (Figure 4.8A) as a downstream effect of oxidative stress. PARP1 has been linked to various DNA repair mechanisms and the maintenance of genomic integrity (Kai, 2016, Perumal *et al*., 2019). It catalyzes the polymerization of ADP-ribose (PAR) units from donor NAD^+ molecules onto target proteins and binds other proteins to the DNA repair complex, including DNA ligase III and others (Hassa *et al*., 2006; Rouleau *et al*., 2010; Pietrzak *et al*., 2018). The three zinc fingers in PARP1's structure are necessary for its DNA repair function; however, H2pmen's chelation of Zn could be contributing to PARP1 inactivation, rendering PARP1 ineffective in its DNA binding and repair activity (Khan *et al.*, 2018). PARP1 is found upstream of p53 and indirectly regulates the phosphorylation of critical substrates in the p53 DNA repair pathway (Valenzuela *et al*., 2002, Zhang *et al*., 2020).

Tumour suppressor protein *p53* functions to integrate multiple stress signals into a series of diverse antiproliferative responses (Hafner *et al.*, 2019). This protein prevents cell cycle progression or induces apoptosis in cells with damaged DNA (Hafner *et al.*, 2019, Shi *et al.*, 2021). In this study, the DNA damage that H2pmen induced caused a significant increase in *p53* protein expression (Figure 4.7D), with consequent activation of pro-apoptotic Bax protein (Figure 4.7E). Located in the mitochondria, Bax interacts with the mitochondrial voltage-dependent anion channel (VDAC) to allow its opening and increase frequency, resulting in loss of membrane potential (Figure 4.3B) and release of cytochrome *c* from the intermembrane space into the cytoplasm (Redza-Dutordoir and Averill-Bates, 2021). Initiator caspase-2, known to induce mitochondrial outer membrane permeabilization (MOMP) through the cleavage and activation of the pro-apoptotic Bid, also faciltates cytochrome *c* release into the cytoplasm (Redza-Dutordoir and Averill-Bates, 2021). In this study, both Bax (Figure 4.7B) and Bid via caspase-2 activation (Figure 4.7A) were significantly increased following H2pmen exposure; consequent mitochondrial cytochrome *c* release will begin the intrinsic apoptotic pathway that activates the downstream effects of apoptosis (Tompkins and Thorburn, 2019).

Cytoplasmic cytochrome *c* forms an apoptosome with Apaf-1 and procaspase-9, resulting in the cleavage and activation of initiator capase-9 (Mhlanga *et al*., 2019). The active caspase-9 (Figure 4.7C) subsequently cleaves and activates executor caspase-3/7 (Figure 4.8B). The data indicate that the intrinsic pathway of apoptosis was responsible for the initiation of apoptosis, since caspase-8 was not activated (Figure 4.7B). It is well known that caspase-3/7 can be activated directly by the initiator caspases, where both activated caspase-8 and caspase-9 can transform procaspase-3/7 into the executioner caspase-3/7 (Pistritto *et al*., 2016, Tompkins and Thorburn, 2019, McComb *et al*., 2019). Deferasirox induced early apoptosis in human malignant lymphoma cells through intrinsic pathway – h2pmen appears to act in a similar manner (Choi *et al.*, 2012). Furthermore, overexpression of STAT3 also upregulates caspase-3 and induces apoptosis as shown in chronic lymphocytic leukemia cells (Rozovski *et al.*, 2016). Excessive activation of STAT3 causes activated STAT3 to bind to STAT3-specific binding sites within the procaspase-3/7 promoter region, resulting in increased transcription of procaspase-3/7 (Rozovski *et al*., 2016, Shunmugam, 2016, Fathi *et al*., 2018). In this study, H2pmen exposure induced a significant increase in the ratio of pSTAT3/STAT3 (Figure 4.8A), suggesting that STAT3 was excessively activated and bound to STAT3-specific binding sites within the procaspase-3/7 promoter region, thus initiating caspase activity and triggering apoptosis. Execution of apoptosis by caspase 3/7 is supported by the increase in PS externalization (Figure 4.8B and C). In literature, PS is considered an early marker of apoptosis when the protein undergoes the process of externalization to the outer leaflet of the plasma membrane (Wang *et al*., 2016). This finding also corresponds with the increase in LDH release (Figure 4.1B) since LDH may also serve as a late marker of apoptosis (Zaib *et al*., 2022). Caspase 3/7 also cleaves and inactivates PARP1 into a 24kDa and 89kDa fragment (Kumar *et al*., 2022); however, in this study upregulated PARP1 (Figure 4.8D) may have been inactivated by H2pmen thus limiting its role in DNA repair and contributing to the morphological features of apoptosis (Kumar *et al*., 2022). The data thus suggests that H2pmen induces caspase-dependent apoptosis via the intrinsic pathway.

CHAPTER 6: CONCLUSION

Morbidity and mortality associated with liver cancer treatment, and the poor five year survival rates indicate a need for viable treatments with minimal side effects. Since metal chelators have demonstrated this potential, this study investigated H2pmen, a novel compound, in HepG2 cells to find a viable and effective treatment for liver cancer. In this study, decreased cell viability by H2pmen was coupled with reduced ATP production and ΔΨm possibly indicating the impaired functioning of the mitochondrial respiratory chain (Figure 6.1). A concomitant increase in $O_2^{\cdot-}$ and NO production (associated with *NF-κB* mediated upregulation of iNOS) was noted; these free radicals contributed to lipid peroxidation and oxidation of DNA as indicated by increased MDA and *OGG1* gene expression respectively (Figure 6.1). The associated decreased SOD2 and GSH prompted the upregulation of *Nrf2*, and *GPx1* to respond to the increased lipid peroxidation (Figure 6.1). The prevailing oxidative stress also upregulated *p53* and STAT3; upregulation of *p53* initiated the intrinsic apoptotic pathway by activating Bax and consequently caspase 9, which together with STAT3 activated caspase 3/7 to execute apoptosis (Figure 6.1). Taken together, the data indicate that H2pmen demonstrated its cytotoxic potential by upregulation of oxidative and nitrosative stress in HepG2 cells, consequently intrinsic caspase-dependent apoptosis was mediated by p53 and STAT3.

The difference noted between the IC_{20} and the IC_{50} on parameters such as OGG1, NF-*k*B, iNOS, GPx1, Nrf2, caspase-2, p53, PARP1 and pSTAT3/STAT3 ratio. The concentration in these parameters potentially interfered with gene expression and therefore protein expression was decreased, or it directly inhibited protein synthesis. However, these are speculations and they will need to be investigated further in future studies. Since NF-κB and STAT3 was increased, it is recommended for future studies to focus on the inflammatory pathway. It is also crucial that the effects of H2pmen should be tested in healthy cells such as Hek293 cells and *in vivo* in future studies.

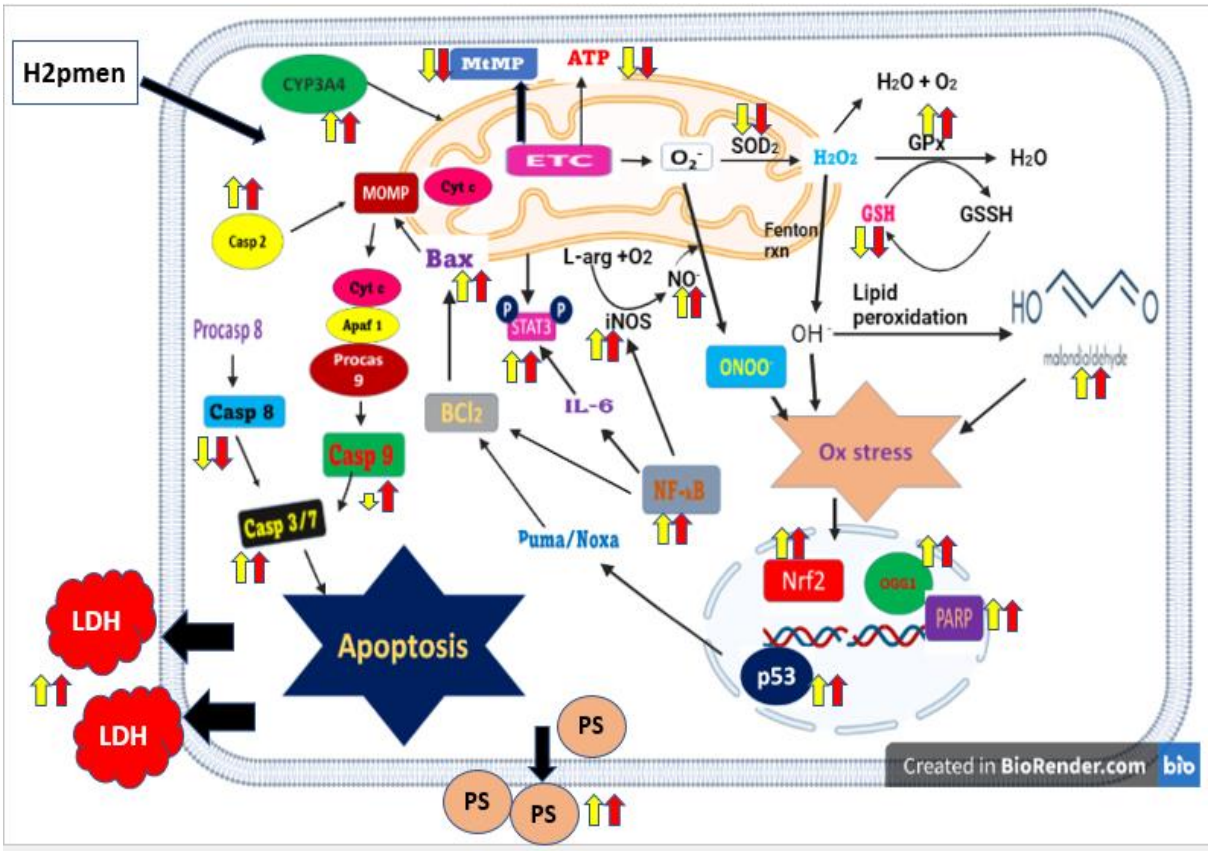

Figure 6.1: Schematic overview of the biochemical effects of H2pmen on metabolism, oxidative stress and apoptosis in HepG2 cells, (Prepared by author, 2022).

REFERENCES

ABDUL, N. S., NAGIAH, S. & CHUTURGOON, A. A. 2016. Fusaric acid induces mitochondrial stress in human hepatocellular carcinoma (HepG2) cells. *Toxicon,* 119**,** 336-344.

ADAN, A., KIRAZ, Y. & BARAN, Y. 2016. Cell proliferation and cytotoxicity assays. *Current pharmaceutical biotechnology,* 17**,** 1213-1221.

ÁLVAREZ-TEIJEIRO, S., MENÉNDEZ, S. T., VILLARONGA, M. Á., PENA-ALONSO, E., RODRIGO, J. P., MORGAN, R. O., GRANDA-DÍAZ, R., SALOM, C., FERNANDEZ, M. P. & GARCÍA-PEDRERO, J. M. 2017. Annexin A1 down-regulation in head and neck squamous cell carcinoma is mediated via transcriptional control with direct involvement of miR-196a/b. *Scientific reports,* 7**,** 1-12.

ANTONELLI, M. & KUSHNER, I. 2017. It's time to redefine inflammation. *The FASEB Journal,* 31**,** 1787-1791.

ARIAS, I. M., ALTER, H. J., BOYER, J. L., COHEN, D. E., SHAFRITZ, D. A., THORGEIRSSON, S. S. & WOLKOFF, A. W. 2020. *The liver: biology and pathobiology,* John Wiley & Sons.

BAHUGUNA, A., KHAN, I., BAJPAI, V. K. & KANG, S. C. 2017. MTT assay to evaluate the cytotoxic potential of a drug. *Bangladesh Journal of Pharmacology,* 12**,** Online: Apr 8-2017.

BAI, J., LI, Y. & ZHANG, G. 2017. Cell cycle regulation and anticancer drug discovery. *Cancer biology & medicine,* 14**,** 348.

BARRERA, G. 2012. Oxidative stress and lipid peroxidation products in cancer progression and therapy. *International Scholarly Research Notices,* 2012.

BASS, J. J., WILKINSON, D. J., RANKIN, D., PHILLIPS, B. E., SZEWCZYK, N. J., SMITH, K. & ATHERTON, P. J. 2017. An overview of technical considerations for Western blotting applications to physiological research. *Scandinavian journal of medicine & science in sports,* 27**,** 4-25.

BELORIBI-DJEFAFLIA, S., VASSEUR, S. & GUILLAUMOND, F. 2016. Lipid metabolic reprogramming in cancer cells. *Oncogenesis,* 5**,** e189-e189.

BENDRIS, N., LEMMERS, B. & BLANCHARD, J. M. 2015. Cell cycle, cytoskeleton dynamics and beyond: the many functions of cyclins and CDK inhibitors. *Cell cycle,* 14**,** 1786-1798.

BIRCH-MACHIN, M. & BOWMAN, A. 2016. Oxidative stress and ageing. *British Journal of Dermatology,* 175**,** 26-29.

BISCHOFF, K., MUKAI, M. & RAMAIAH, S. K. 2018. Liver toxicity. *Veterinary toxicology.* Elsevier.

BOITEUX, S. & RADICELLA, J. P. 2000. The human OGG1 gene: structure, functions, and its implication in the process of carcinogenesis. *Archives of biochemistry and biophysics,* 377**,** 1-8.

BRAND, M. D. & MURPHY, M. P. 1987. Control of electron flux through the respiratory chain in mitochondria and cells. *Biological Reviews,* 62**,** 141-193.

BUFFOLI, B., PECHÁNOVÁ, O., KOJŠOVÁ, S., ANDRIANTSITOHAINA, R., GIUGNO, L., BIANCHI, R. & REZZANI, R. 2005. Provinol prevents CsA-induced nephrotoxicity by reducing reactive oxygen species, iNOS, and NF-kB expression. *Journal of Histochemistry & Cytochemistry,* 53**,** 1459-1468.

CALDERARO, J., ZIOL, M., PARADIS, V. & ZUCMAN-ROSSI, J. 2019. Molecular and histological correlations in liver cancer. *Journal of hepatology,* 71**,** 616-630.

CARO, A. A., COMMISSARIAT, A., DUNN, C., KIM, H., GARCÍA, S. L., SMITH, A., STRANG, H., STUPPY, J., DESROCHERS, L. P. & GOODWIN, T. E. 2015. Prooxidant and antioxidant properties of salicylaldehyde isonicotinoyl hydrazone iron chelators in HepG2 cells. *Biochimica Et Biophysica Acta (BBA)-General Subjects,* 1850**,** 2256-2264.

CHATTERJEE, S. 2016. Oxidative stress, inflammation, and disease. *Oxidative stress and biomaterials.* Elsevier.

CHEN, H. H. & KUO, M. T. 2017. Improving radiotherapy in cancer treatment: Promises and challenges. *Oncotarget,* 8**,** 62742.

CHEN, L., DENG, H., CUI, H., FANG, J., ZUO, Z., DENG, J., LI, Y., WANG, X. & ZHAO, L. 2018. Inflammatory responses and inflammation-associated diseases in organs. *Oncotarget,* 9**,** 7204.

CHEN, S., WU, Q., LI, X., LI, D., MEI, N., NING, B., PUIG, M., REN, Z., TOLLESON, W. H. & GUO, L. 2021. Characterization of cytochrome P450s (CYP)-overexpressing HepG2 cells for assessing drug and chemical-induced liver toxicity. *Journal of Environmental Science and Health, Part C,* 39**,** 68-86.

CHO, H.-Y. & KLEEBERGER, S. R. 2020. Mitochondrial biology in airway pathogenesis and the role of NRF2. *Archives of pharmacal research,* 43**,** 297-320.

CORELLA, D., RAMÍREZ-SABIO, J. B., COLTELL, O., ORTEGA-AZORÍN, C., ESTRUCH, R., MARTÍNEZ-GONZÁLEZ, M. A., SALAS-SALVADÓ, J., SORLÍ, J. V., CASTAÑER, O. & ARÓS, F. 2018. Effects of the Ser326Cys polymorphism in the DNA repair OGG1 gene on cancer, cardiovascular, and all-cause mortality in the PREDIMED study: modulation by diet. *Journal of the Academy of Nutrition and Dietetics,* 118**,** 589-605.

DE LEON, J. A. D. & BORGES, C. R. 2020. Evaluation of oxidative stress in biological samples using the thiobarbituric acid reactive substances assay. *JoVE (Journal of Visualized Experiments)***,** e61122.

DEVNARAIN, N., TILOKE, C., NAGIAH, S. & CHUTURGOON, A. A. 2017. Fusaric acid induces oxidative stress and apoptosis in human cancerous oesophageal SNO cells. *Toxicon,* 126**,** 4-11.

DICKENS, E. & AHMED, S. 2018. Principles of cancer treatment by chemotherapy. *Surgery (Oxford),* 36**,** 134-138.

DIKALOVA, A. E., ITANI, H. A., NAZAREWICZ, R. R., MCMASTER, W. G., FLYNN, C. R., UZHACHENKO, R., FESSEL, J. P., GAMBOA, J. L., HARRISON, D. G. & DIKALOV, S. I. 2017. Sirt3 impairment and SOD2 hyperacetylation in vascular oxidative stress and hypertension. *Circulation research,* 121**,** 564-574.

DONG, N., LI, Y., QI, J., CHEN, Y. & HAO, Y. 2018. Nitric oxide synthase-dependent nitric oxide production enhances chilling tolerance of walnut shoots *in vitro* via involvement chlorophyll fluorescence and other physiological parameter levels. *Scientia Horticulturae,* 230**,** 68-77.

ESPÍN, S., SÁNCHEZ-VIROSTA, P., GARCÍA-FERNÁNDEZ, A. & EEVA, T. 2017. A microplate adaptation of the thiobarbituric acid reactive substances assay to determine lipid peroxidation fluorometrically in sm all sample volumes. *Revista de Toxicología,* 34**,** 94-98.

FAVORITI, P., CARBONE, G., GRECO, M., PIROZZI, F., PIROZZI, R. E. M. & CORCIONE, F. 2016. Worldwide burden of colorectal cancer: a review. *Updates in surgery,* 68**,** 7-11.

FENO, S., BUTERA, G., VECELLIO REANE, D., RIZZUTO, R. & RAFFAELLO, A. 2019. Crosstalk between calcium and ROS in pathophysiological conditions. *Oxidative medicine and cellular longevity,* 2019.

GAI, Z., VISENTIN, M., GUI, T., ZHAO, L., THASLER, W. E., HÄUSLER, S., HARTLING, I., CREMONESI, A., HILLER, C. & KULLAK-UBLICK, G. A. 2018. Effects of farnesoid X receptor activation on arachidonic acid metabolism, NF-kB signaling, and hepatic inflammation. *Molecular pharmacology,* 94**,** 802-811.

GAUR, K., VÁZQUEZ-SALGADO, A. M., DURAN-CAMACHO, G., DOMINGUEZ-MARTINEZ, I., BENJAMÍN-RIVERA, J. A., FERNÁNDEZ-VEGA, L., CARMONA SARABIA, L., CRUZ GARCÍA, A., PÉREZ-DELIZ, F. & MÉNDEZ ROMÁN, J. A. 2018. Iron and copper intracellular chelation as an anticancer drug strategy. *Inorganics,* 6**,** 126.

GHANI, M. A., BARRIL, C., BEDGOOD JR, D. R. & PRENZLER, P. D. 2017. Measurement of antioxidant activity with the thiobarbituric acid reactive substances assay. *Food chemistry,* 230**,** 195-207.

GHOSH, S. C., NGIAM, J. S., CHAI, C. L., SEAYAD, A. M., DANG, T. T. & CHEN, A. 2012. Iron-Catalyzed Efficient Synthesis of Amides from Aldehydes and Amine Hydrochloride Salts. *Advanced Synthesis & Catalysis,* 354**,** 1407-1412.

GILARDINI MONTANI, M. S., SANTARELLI, R., GRANATO, M., GONNELLA, R., TORRISI, M., FAGGIONI, A. & CIRONE, M. 2019. EBV reduces autophagy, intracellular ROS and mitochondria to impair monocyte survival and differentiation. *Autophagy,* 15**,** 652-667.

GILBERTO, S. & PETER, M. 2017. Dynamic ubiquitin signaling in cell cycle regulation. *Journal of Cell Biology,* 216**,** 2259-2271.

GONG, L., TANG, Y., AN, R., LIN, M., CHEN, L. & DU, J. 2017. RTN1-C mediates cerebral ischemia/reperfusion injury via ER stress and mitochondria-associated apoptosis pathways. *Cell death & disease,* 8**,** e3080-e3080.

GRAHAM, K. & UNGER, E. 2018. Overcoming tumor hypoxia as a barrier to radiotherapy, chemotherapy and immunotherapy in cancer treatment. *International journal of nanomedicine,* 13**,** 6049.

GRANADOS-ROMERO, J. J., VALDERRAMA-TREVIÑO, A. I., CONTRERAS-FLORES, E. H., BARRERA-MERA, B., HERRERA ENRÍQUEZ, M., URIARTE-RUÍZ, K., CEBALLOS-VILLALBA, J., ESTRADA-MATA, A. G., ALVARADO RODRÍGUEZ, C. & ARAUZ-PEÑA, G. 2017. Colorectal cancer: a review. *Int J Res Med Sci,* 5**,** 4667-4676.

GRETEN, F. R. & GRIVENNIKOV, S. I. 2019. Inflammation and cancer: triggers, mechanisms, and consequences. *Immunity,* 51**,** 27-41.

GUSEV, A. N., KISKIN, M. A., BRAGA, E. V., CHAPRAN, M., WIOSNA-SALYGA, G., BARYSHNIKOV, G. V., MINAEVA, V. A., MINAEV, B. F., IVANIUK, K. & STAKHIRA, P. 2019. Novel zinc complex with an ethylenediamine schiff base for high-luminance blue fluorescent OLED applications. *The Journal of Physical Chemistry C,* 123**,** 11850-11859.

HASHIMOTO, M., SAITO, N., OHTA, H., YAMAMOTO, K., TASHIRO, A., NAKAZAWA, K., INANAMI, O. & KITAMURA, H. 2019. Inhibition of ubiquitin-specific protease 2 causes accumulation of reactive oxygen species, mitochondria dysfunction, and intracellular ATP decrement in C2C12 myoblasts. *Physiological reports,* 7**,** e14193.

HASSANPOUR, S. H. & DEHGHANI, M. 2017. Review of cancer from perspective of molecular. *Journal of Cancer Research and Practice,* 4**,** 127-129.

HAYES, J. D., DINKOVA-KOSTOVA, A. T. & TEW, K. D. 2020. Oxidative stress in cancer. *Cancer Cell*.

HEIDARI-SORESHJANI, S., ASADI-SAMANI, M., YANG, Q. & SAEEDI-BOROUJENI, A. 2017. Phytotherapy of nephrotoxicity-induced by cancer drugs: an updated review. *Journal of nephropathology,* 6**,** 254.

HOES, M. F., GROTE BEVERBORG, N., KIJLSTRA, J. D., KUIPERS, J., SWINKELS, D. W., GIEPMANS, B. N., RODENBURG, R. J., VAN VELDHUISEN, D. J., DE BOER, R. A. & VAN DER MEER, P. 2018. Iron deficiency impairs contractility of human cardiomyocytes through decreased mitochondrial function. *European journal of heart failure,* 20**,** 910-919.

HONG, X.-L., LIU, L.-J., LU, W.-G. & WANG, X.-B. 2017. A vanadium (V) terpyridine complex: Synthesis, characterization, cytotoxicity *in vitro* and induction of apoptosis in cancer cells. *Transition Metal Chemistry,* 42**,** 459-467.

HOSOOKA, T. & OGAWA, W. 2016. A novel role for the cell cycle regulatory complex cyclin D1–CDK 4 in gluconeogenesis. *Journal of diabetes investigation,* 7**,** 27-28.

HUANG, Z., HUANG, Z., FENG, L., LUO, X., WU, P., CUI, L. & MAO, X. 2018. Modified cellulose by polyethyleneimine and ethylenediamine with induced Cu (II) and Pb (II) adsorption potentialities. *Carbohydrate polymers,* 202**,** 470-478.

HUSSAIN, T., TAN, B., YIN, Y., BLACHIER, F., TOSSOU, M. C. & RAHU, N. 2016. Oxidative stress and inflammation: what polyphenols can do for us? *Oxidative medicine and cellular longevity,* 2016.

HUSTEDT, N. & DUROCHER, D. 2017. The control of DNA repair by the cell cycle. *Nature cell biology,* 19**,** 1-9.

ICARD, P., FOURNEL, L., WU, Z., ALIFANO, M. & LINCET, H. 2019. Interconnection between metabolism and cell cycle in cancer. *Trends in biochemical sciences,* 44**,** 490-501.

ISLAM, M. O., BACCHETTI, T. & FERRETTI, G. 2019. Alterations of antioxidant enzymes and biomarkers of nitro-oxidative stress in tissues of bladder cancer. *Oxidative medicine and cellular longevity,* 2019.

JI, Z., HE, L., REGEV, A. & STRUHL, K. 2019. Inflammatory regulatory network mediated by the joint action of NF-kB, STAT3, and AP-1 factors is involved in many human cancers. *Proceedings of the National Academy of Sciences,* 116**,** 9453-9462.

JURISEVIC, M., ARSENIJEVIC, A., PANTIC, J., GAJOVIC, N., MILOVANOVIC, J., MILOVANOVIC, M., POLJAREVIC, J., SABO, T., VOJVODIC, D. & RADOSAVLJEVIC, G. D. 2018. The organic ester O, O'-diethyl-(S, S)-ethylenediamine-N, N'-di-2-(3-cyclohexyl) propanoate dihydrochloride attenuates murine breast cancer growth and metastasis. *Oncotarget,* 9**,** 28195.

KABAKOV, A. E. & GABAI, V. L. 2018. Cell death and survival assays. *Chaperones.* Springer.

KIJANSKA, M. & KELM, J. 2016. *In vitro* 3D spheroids and microtissues: ATP-based cell viability and toxicity assays. *Assay guidance manual [Internet]*.

KONTOGHIORGHES, G. J. & KONTOGHIORGHE, C. N. 2020. Iron and chelation in biochemistry and medicine: new approaches to controlling iron metabolism and treating related diseases. *Cells,* 9**,** 1456.

KUMAR, P., NAGARAJAN, A. & UCHIL, P. D. 2018. Analysis of cell viability by the lactate dehydrogenase assay. *Cold Spring Harbor Protocols,* 2018**,** pdb. prot095497.

KUPCHO, K., SHULTZ, J., HURST, R., HARTNETT, J., ZHOU, W., MACHLEIDT, T., GRAILER, J., WORZELLA, T., RISS, T. & LAZAR, D. 2019. A real-time, bioluminescent annexin V assay for the assessment of apoptosis. *Apoptosis,* 24**,** 184-197.

LEWIS, J., ALATTAR, A. A., AKERS, J., CARTER, B. S., HELLER, M. & CHEN, C. C. 2019. A pilot proof-of-principle analysis demonstrating dielectrophoresis (DEP) as a glioblastoma biomarker platform. *Scientific reports,* 9**,** 1-10.

LI, L. & WANG, H. 2016. Heterogeneity of liver cancer and personalized therapy. *Cancer letters,* 379**,** 191-197.

LI, S., TAN, H.-Y., WANG, N., ZHANG, Z.-J., LAO, L., WONG, C.-W. & FENG, Y. 2015. The role of oxidative stress and antioxidants in liver diseases. *International journal of molecular sciences,* 16**,** 26087-26124.

LICATA, A. 2016. Adverse drug reactions and organ damage: the liver. *European journal of internal medicine,* 28**,** 9-16.

LIMBOONREUNG, T., TUCHINDA, P. & CHONGTHAMMAKUN, S. 2020. Chrysoeriol mediates mitochondrial protection via PI3K/Akt pathway in MPP+ treated SH-SY5Y cells. *Neuroscience letters,* 714**,** 134545.

LIU, L., LIU, D., XIANG, C., DAI, W., LI, B. & ZHANG, M. 2020. Sesquiterpene lactones from Artemisia austroyunnanensis suppresses ROS production and reduces cytokines, iNOS and COX-2 levels via NF-KB pathway *in vitro*. *Natural product research,* 34**,** 1563-1566.

LOPEZ, J. & TAIT, S. 2015. Mitochondrial apoptosis: killing cancer using the enemy within. *British journal of cancer,* 112**,** 957-962.

LOUGHNEY, L., WEST, M., KEMP, G., GROCOTT, M. & JACK, S. 2016. Exercise intervention in people with cancer undergoing neoadjuvant cancer treatment and surgery: a systematic review. *European Journal of Surgical Oncology (EJSO),* 42**,** 28-38.

LV, L.-H., WAN, Y.-L., LIN, Y., ZHANG, W., YANG, M., LI, G.-L., LIN, H.-M., SHANG, C.-Z., CHEN, Y.-J. & MIN, J. 2012. Anticancer drugs cause release of exosomes with heat shock proteins from human hepatocellular carcinoma cells that elicit effective natural killer cell antitumor responses *in vitro*. *Journal of Biological Chemistry,* 287**,** 15874-15885.

MA, Y.-L., ZHANG, Y.-S., ZHANG, F., ZHANG, Y.-Y., THAKUR, K., ZHANG, J.-G. & WEI, Z.-J. 2019. Methyl protodioscin from Polygonatum sibiricum inhibits cervical cancer through cell cycle arrest and apoptosis induction. *Food and Chemical Toxicology,* 132**,** 110655.

MAHENDIRAN, D., KUMAR, R. S. & RAHIMAN, A. K. 2017. Heteroleptic silver (I) complexes with 2, 2′: 6′, 2 ″-terpyridines and naproxen: DNA interaction, EGFR/VEGFR2 kinase, growth inhibition and cell cycle arrest studies. *Materials science and engineering: C,* 76**,** 601-615.

MANIKANDAMATHAVAN, V., THANGARAJ, M., WEYHERMULLER, T., PARAMESWARI, R., PUNITHA, V., MURTHY, N. N. & NAIR, B. U. 2017. Novel mononuclear Cu (II) terpyridine complexes: Impact of fused ring thiophene and thiazole head groups towards DNA/BSA interaction, cleavage and antiproliferative activity on HepG2 and triple negative CAL-51 cell line. *European journal of medicinal chemistry,* 135**,** 434-446.

MARÍ, M., MORALES, A., COLELL, A., GARCÍA-RUIZ, C. & FERNÁNDEZ-CHECA, J. C. 2009. Mitochondrial glutathione, a key survival antioxidant. *Antioxidants & redox signaling,* 11**,** 2685-2700.

MATSUURA, K., CANFIELD, K., FENG, W. & KUROKAWA, M. 2016. Metabolic regulation of apoptosis in cancer. *International review of cell and molecular biology,* 327**,** 43-87.

MCCOMB, S., CHAN, P. K., GUINOT, A., HARTMANNSDOTTIR, H., JENNI, S., DOBAY, M. P., BOURQUIN, J.-P. & BORNHAUSER, B. C. 2019. Efficient apoptosis requires feedback amplification of upstream apoptotic signals by effector caspase-3 or-7. *Science advances,* 5**,** eaau9433.

MEVADA, S. T., ALDHULI, A. S., AL-RAWAS, A. H., AL-KHABORI, M. K., NAZIR, H., ZACHARIAH, M. & WALI, P. Y. 2014. Liver Enzymes Changes and Safety Profile of Deferasirox Iron Chelator in Omani Children with Thalassemia Major. American Society of Hematology Washington, DC.

MHLANGA, P., PERUMAL, P. O., SOMBORO, A. M., AMOAKO, D. G., KHUMALO, H. M. & KHAN, R. B. 2019. Mechanistic insights into oxidative stress and apoptosis mediated by tannic acid in human liver hepatocellular carcinoma cells. *International journal of molecular sciences,* 20**,** 6145.

MILLER, K. D., SIEGEL, R. L., LIN, C. C., MARIOTTO, A. B., KRAMER, J. L., ROWLAND, J. H., STEIN, K. D., ALTERI, R. & JEMAL, A. 2016. Cancer treatment and survivorship statistics, 2016. *CA: a cancer journal for clinicians,* 66**,** 271-289.

MIYAI, T., TOYONO, T., KITAMOTO, K., FUKUSHIMA, M., YOSHIDA, J., SHIRAKAWA, R., NAKAGAWA, S., JURKUNAS, U. V. & USUI, T. 2018. Endoplasmic reticulum stress decreases mitochondrial membrane potential and upregulates PARK2 expression in corneal endothelium. *Investigative Ophthalmology & Visual Science,* 59**,** 4436-4436.

MOHAN, J. 2019. *Fumonisin B2 induces mitochondrial stress and mitophagy in Hek293 cells.*

MOSMANN, T. 1983. Rapid colorimetric assay for cellular growth and survival: application to proliferation and cytotoxicity assays. *Journal of immunological methods,* 65**,** 55-63.

MPOSULA, S., AMOAKO, D. G., SOMBORO, A. M., ARHIN, I., KUMALO, H. M. & KHAN, R. B. 2021. Apoptosis-inducing effects of Terminalia phanerophlebia leaf extracts on human renal cells. *South African Journal of Botany,* 139**,** 273-280.

MUKERJEE, S., SAEEDAN, A. S., ANSARI, M. & SINGH, M. 2021. Polyunsaturated Fatty Acids Mediated Regulation of Membrane Biochemistry and Tumor Cell Membrane Integrity. *Membranes,* 11**,** 479.

MUNN, L. L. 2017. Cancer and inflammation. *Wiley Interdisciplinary Reviews: Systems Biology and Medicine,* 9**,** e1370.

MURATA, M. 2018. Inflammation and cancer. *Environmental health and preventive medicine,* 23**,** 1-8.

NAGURA-IKEDA, M., IMAI, K., TABATA, S., MIYOSHI, K., MURAHARA, N., MIZUNO, T., HORIUCHI, M., KATO, K., IMOTO, Y. & IWATA, M. 2020. Clinical evaluation of self-collected saliva by quantitative reverse transcription-PCR (RT-qPCR), direct RT-qPCR, reverse transcription–loop-mediated isothermal amplification, and a rapid antigen test to diagnose COVID-19. *Journal of clinical microbiology,* 58**,** e01438-20.

NING, J., WANG, W., GE, G., CHU, P., LONG, F., YANG, Y., PENG, Y., FENG, L., MA, X. & JAMES, T. D. 2019. Target Enzyme-Activated Two-Photon Fluorescent Probes: A Case

Study of CYP3A4 Using a Two-Dimensional Design Strategy. *Angewandte Chemie,* 131**,** 10064-10068.

O'DONNELL, J. S., HOEFSMIT, E. P., SMYTH, M. J., BLANK, C. U. & TENG, M. W. 2019. The promise of neoadjuvant immunotherapy and surgery for cancer treatment. *Clinical Cancer Research,* 25**,** 5743-5751.

ORTEGA-ALONSO, A. & ANDRADE, R. J. 2018. Chronic liver injury induced by drugs and toxins. *Journal of digestive diseases,* 19**,** 514-521.

OTTO, T. & SICINSKI, P. 2017. Cell cycle proteins as promising targets in cancer therapy. *Nature Reviews Cancer,* 17**,** 93.

PARHAMIFAR, L., ANDERSEN, H. & MOGHIMI, S. M. 2019. Lactate dehydrogenase assay for assessment of polycation cytotoxicity. *Nanotechnology for Nucleic Acid Delivery.* Springer.

PASCUA-MAESTRO, R., CORRALIZA-GOMEZ, M., DIEZ-HERMANO, S., PEREZ-SEGURADO, C., GANFORNINA, M. D. & SANCHEZ, D. 2018. The MTT-formazan assay: Complementary technical approaches and *in vivo* validation in Drosophila larvae. *Acta histochemica,* 120**,** 179-186.

PEOPLES, J. N., SARAF, A., GHAZAL, N., PHAM, T. T. & KWONG, J. Q. 2019. Mitochondrial dysfunction and oxidative stress in heart disease. *Experimental & molecular medicine,* 51**,** 1-13.

PERUMAL, P. O., MHLANGA, P., SOMBORO, A. M., AMOAKO, D. G., KHUMALO, H. M. & KHAN, R. M. 2019. Cytoproliferative and Anti-Oxidant Effects Induced by Tannic Acid in Human Embryonic Kidney (Hek-293) Cells. *Biomolecules,* 9**,** 767.

PETRICK, J. L. & MCGLYNN, K. A. 2019. The changing epidemiology of primary liver cancer. *Current epidemiology reports,* 6**,** 104-111.

PFEFFER, C. M. & SINGH, A. T. 2018. Apoptosis: a target for anticancer therapy. *International journal of molecular sciences,* 19**,** 448.

POPOV, I. A., DAVIS, B. L., MUKUNDAN, R., BATISTA, E. R. & YANG, P. 2019. Catalyst-inspired charge carriers for high energy density redox flow batteries. *Frontiers in Physics,* 6**,** 141.

PUCHKOV, P. A., SHMENDEL, E. V., ANDREEVA, V. D., MOROZOVA, N. G., ZENKOVA, M. A. & MASLOV, M. A. 2018. 1, 28-Di [(cholest-5-en-3β-yl) disulfanyl]-4, 25-dioxo-3, 8, 12, 17, 21, 26-hexaazaoctacosane tetrahydrochloride.

RAI, Y., PATHAK, R., KUMARI, N., SAH, D. K., PANDEY, S., KALRA, N., SONI, R., DWARAKANATH, B. & BHATT, A. N. 2018. Mitochondrial biogenesis and metabolic hyperactivation limits the application of MTT assay in the estimation of radiation induced growth inhibition. *Scientific reports,* 8**,** 1-15.

REDZA-DUTORDOIR, M. & AVERILL-BATES, D. A. 2021. Interactions between reactive oxygen species and autophagy special issue: Death mechanisms in cellular homeostasis. *Biochimica et Biophysica Acta (BBA)-Molecular Cell Research***,** 119041.

RISS, T., NILES, A., MORAVEC, R., KARASSINA, N. & VIDUGIRIENE, J. 2019. Cytotoxicity assays: *in vitro* methods to measure dead cells. *Assay Guidance Manual [Internet]*.

RISS, T. L., MORAVEC, R. A., NILES, A. L., DUELLMAN, S., BENINK, H. A., WORZELLA, T. J. & MINOR, L. 2016. Cell viability assays. *Assay Guidance Manual [Internet]*.

SANTOS, M. L. C., DE BRITO, B. B., DA SILVA, F. A. F., DOS SANTOS BOTELHO, A. C. & DE MELO, F. F. 2020. Nephrotoxicity in cancer treatment: An overview. *World journal of clinical oncology,* 11**,** 190.

SANTOS, S., SILVA, A. M., MATOS, M., MONTEIRO, S. M. & ÁLVARO, A. R. 2016. Copper induced apoptosis in Caco-2 and Hep-G2 cells: Expression of caspases 3, 8 and 9, AIF and p53. *Comparative Biochemistry and Physiology Part C: Toxicology & Pharmacology,* 185**,** 138-146.

ŠARIĆ MUSTAPIĆ, D., DEBELJAK, Ž., MALEŠ, Ž. & BOJIĆ, M. 2018. The inhibitory effect of flavonoid aglycones on the metabolic activity of CYP3A4 enzyme. *Molecules,* 23**,** 2553.

SATYO, L., AMOAKO, D. G., SOMBORO, A. M., SOSIBO, S. C., KUMALO, H. M., MHLONGO, N. N. & KHAN, R. B. 2020. Molecular insights into Di (2-Picolyl) amine–induced cytotoxicity and apoptosis in human kidney (HEK293) cells. *International journal of toxicology,* 39**,** 341-351.

SEDLACKOVA, L. & KOROLCHUK, V. I. 2019. Mitochondrial quality control as a key determinant of cell survival. *Biochimica et Biophysica Acta (BBA)-Molecular Cell Research,* 1866**,** 575-587.

SEVRIOUKOVA, I. F. & POULOS, T. L. 2017. Structural basis for regiospecific midazolam oxidation by human cytochrome P450 3A4. *Proceedings of the National Academy of Sciences,* 114**,** 486-491.

SHARMA, R. & PANDITA, A. 2020. Chelation in Metal Intoxication. *Journal of Critical Reviews,* 7**,** 828-832.

SHUNMUGAM, L. 2016. *Moringa oleifera crude aqueous leaf extract induces apoptosis in human hepatocellular carcinoma cells via the upregulation of NF-kB and IL-6/STAT3 pathway.*

SIBIYA, T. 2018. *Fumonisin B1 induced antioxidant response in C57BL/6 male mice brain.*

SIES, H. 2015. Oxidative stress: a concept in redox biology and medicine. *Redox biology,* 4**,** 180-183.

SIES, H., BERNDT, C. & JONES, D. P. 2017. Oxidative stress. *Annual review of biochemistry,* 86**,** 715-748.

SIMON, K. 2016. Colorectal cancer development and advances in screening. *Clinical interventions in aging,* 11**,** 967.

SU, L.-J., ZHANG, J.-H., GOMEZ, H., MURUGAN, R., HONG, X., XU, D., JIANG, F. & PENG, Z.-Y. 2019. Reactive oxygen species-induced lipid peroxidation in apoptosis, autophagy, and ferroptosis. *Oxidative medicine and cellular longevity,* 2019.

SU, Z., YANG, Z., XU, Y., CHEN, Y. & YU, Q. 2015. Apoptosis, autophagy, necroptosis, and cancer metastasis. *Molecular cancer,* 14**,** 48.

SUN, J., LIU, F., YU, W., JIANG, Q., HU, J., LIU, Y., WANG, F. & LIU, X. 2019. Highly sensitive glutathione assay and intracellular imaging with functionalized semiconductor quantum dots. *Nanoscale,* 11**,** 5014-5020.

SUN, S.-C. 2017. The non-canonical NF-κB pathway in immunity and inflammation. *Nature Reviews Immunology,* 17**,** 545.

TAABAZUING, C. Y., OKONDO, M. C. & BACHOVCHIN, D. A. 2017. Pyroptosis and apoptosis pathways engage in bidirectional crosstalk in monocytes and macrophages. *Cell chemical biology,* 24**,** 507-514. e4.

TACCONE-GALLUCCI, M., MANCA-DI-VILLAHERMOSA, S., BATTISTINI, L., STUFFLER, R. G., TEDESCO, M. & MACCARRONE, M. 2006. N-3 PUFAs reduce oxidative stress in ESRD patients on maintenance HD by inhibiting 5-lipoxygenase activity. *Kidney Int,* 69**,** 1450-4.

TANAKA, A., YAMAMOTO, A., MUROTA, K., TSUJIUCHI, T., IWAMORI, M. & FUKUSHIMA, N. 2017. Polyunsaturated fatty acids induce ovarian cancer cell death through ROS-dependent MAP kinase activation. *Biochemical and biophysical research communications,* 493**,** 468-473.

TILOKANI, L., NAGASHIMA, S., PAUPE, V. & PRUDENT, J. 2018. Mitochondrial dynamics: overview of molecular mechanisms. *Essays in biochemistry,* 62**,** 341-360.

TORNESELLO, A. L., BUONAGURO, L., TORNESELLO, M. L. & BUONAGURO, F. M. 2017. New insights in the design of bioactive peptides and chelating agents for imaging and therapy in oncology. *Molecules,* 22**,** 1282.

ÜNAL, E., AKATA, D. & KARCAALTINCABA, M. Liver function assessment by magnetic resonance imaging. Seminars in Ultrasound, CT and MRI, 2016. Elsevier, 549-560.

VALERY, P. C., LAVERSANNE, M., CLARK, P. J., PETRICK, J. L., MCGLYNN, K. A. & BRAY, F. 2018. Projections of primary liver cancer to 2030 in 30 countries worldwide. *Hepatology,* 67**,** 600-611.

WANG, P., HENNING, S. M. & HEBER, D. 2010. Limitations of MTT and MTS-based assays for measurement of antiproliferative activity of green tea polyphenols. *PloS one,* 5**,** e10202.

WOOD, M. R., BERNAL, I. & LALANCETTE, R. A. 2017. The hydrochloride hydrates of pentylone and dibutylone and the hydrochloride salt of ephylone: the structures of three novel designer cathinones. *Structural Chemistry,* 28**,** 1369-1376.

XU, H.-H., DENG, H.-H., LIN, X.-Q., WU, Y.-Y., LIN, X.-L., PENG, H.-P., LIU, A.-L., XIA, X.-H. & CHEN, W. 2017. Colorimetric glutathione assay based on the peroxidase-like activity of a nanocomposite consisting of platinum nanoparticles and graphene oxide. *Microchimica Acta,* 184**,** 3945-3951.

YALCIN, T. E., ILBASMIS-TAMER, S. & TAKKA, S. 2020. Antitumor activity of gemcitabine hydrochloride loaded lipid polymer hybrid nanoparticles (LPHNs): *in vitro* and *in vivo*. *International journal of pharmaceutics,* 580**,** 119246.

YOON, Y.-S., BYUN, H.-O., CHO, H., KIM, B.-K. & YOON, G. 2003. Complex II defect via down-regulation of iron-sulfur subunit induces mitochondrial dysfunction and cell cycle delay in iron chelation-induced senescence-associated growth arrest. *Journal of Biological Chemistry,* 278**,** 51577-51586.

YU, Y., GUTIERREZ, E., KOVACEVIC, Z., SALETTA, F., OBEIDY, P., SURYO RAHMANTO, Y. & R RICHARDSON, D. 2012. Iron chelators for the treatment of cancer. *Current medicinal chemistry,* 19**,** 2689-2702.

ZAHEDIFARD, M., FARAJ, F. L., PAYDAR, M., LOOI, C. Y., HAJREZAEI, M., HASANPOURGHADI, M., KAMALIDEHGHAN, B., MAJID, N. A., ALI, H. M. & ABDULLA, M. A. 2015. Synthesis, characterization and apoptotic activity of quinazolinone Schiff base derivatives toward MCF-7 cells via intrinsic and extrinsic apoptosis pathways. *Scientific reports,* 5**,** 11544.

ZHOU, S.-F., XUE, C. C., YU, X.-Q., LI, C. & WANG, G. 2007. Clinically important drug interactions potentially involving mechanism-based inhibition of cytochrome P450 3A4 and the role of therapeutic drug monitoring. *Therapeutic drug monitoring,* 29**,** 687-710.

ZHU, W., YANG, B., FU, H., MA, L., LIU, T., CHAI, R., ZHENG, Z., ZHANG, Q. & LI, G. 2015. Flavone inhibits nitric oxide synthase (NOS) activity, nitric oxide production and protein S-nitrosylation in breast cancer cells. *Biochemical and biophysical research communications,* 458**,** 590-595.

APPENDICES

APPENDIX A

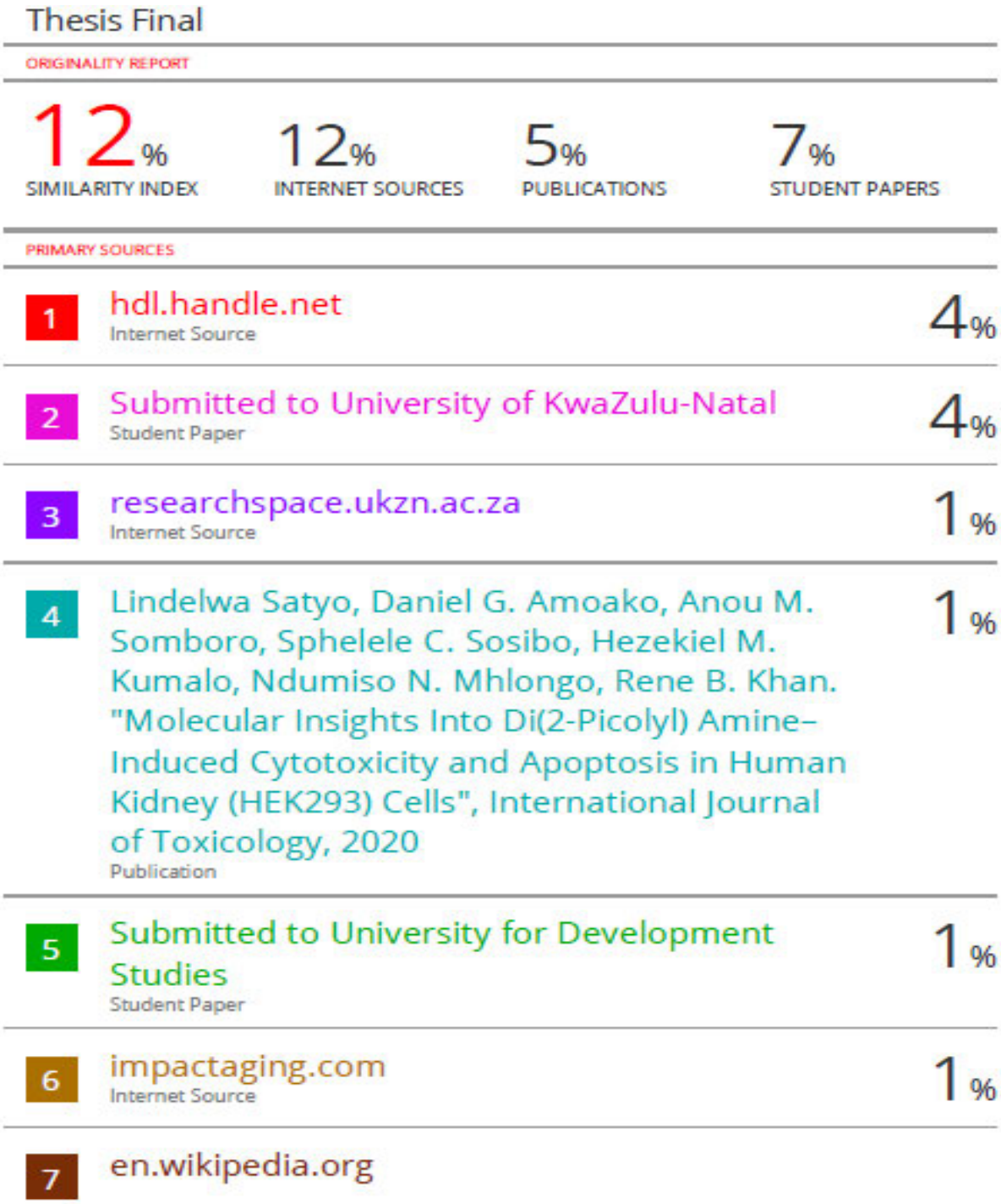

Thesis Final

ORIGINALITY REPORT

12%	12%	5%	7%
SIMILARITY INDEX	INTERNET SOURCES	PUBLICATIONS	STUDENT PAPERS

PRIMARY SOURCES

1	hdl.handle.net Internet Source	4%
2	Submitted to University of KwaZulu-Natal Student Paper	4%
3	researchspace.ukzn.ac.za Internet Source	1%
4	Lindelwa Satyo, Daniel G. Amoako, Anou M. Somboro, Sphelele C. Sosibo, Hezekiel M. Kumalo, Ndumiso N. Mhlongo, Rene B. Khan. "Molecular Insights Into Di(2-Picolyl) Amine–Induced Cytotoxicity and Apoptosis in Human Kidney (HEK293) Cells", International Journal of Toxicology, 2020 Publication	1%
5	Submitted to University for Development Studies Student Paper	1%
6	impactaging.com Internet Source	1%
7	en.wikipedia.org	

Figure 1: Turnitin report

APPENDIX B

HepG2 cells were treated with a range of H2pmen concentrations (0 – 1000 µg/ml) over a 24h period. The MTT assay revealed a dose-dependent decrease in HepG2 cells viability and an IC_{20} of 71 µg/ml and an IC_{50} of 209 µg/ml was determined (Appendix Table 1).

Table 1: The determination of the IC_{50} using the cell viability (MTT) assay.

H2pmen Concentration (µg/ml)	**Average Absorbance**	**% Viability**	**Log[H2pmen]**
0	3,295	100	
25	2,751333	83	1,39794
50	2,545	77	1,69897
100	1,886	57	2,00000
250	0,463	14	2,39794
500	0,136	4	2,69897
750	0,064	2	2,875061
1000	0,076	2	3,00000

APPENDIX C

Table 1: The determination of the nitrates and nitrites standard reference curve

Nitrite Standard Concentrations (µM)	**OD1**	**OD2**	**Average OD**
0	-0,044	-0,044	-0,044
25	0,094	0,102	0,098
50	0,227	0,237	0,232
75	0,259	0,344	0,3015
100	0,401	0,482	0,4415
125	0,635	0,562	0,5985
150	0,667	0,689	0,678
175	0,71	0,745	0,7275
200	0,783	0,891	0,837

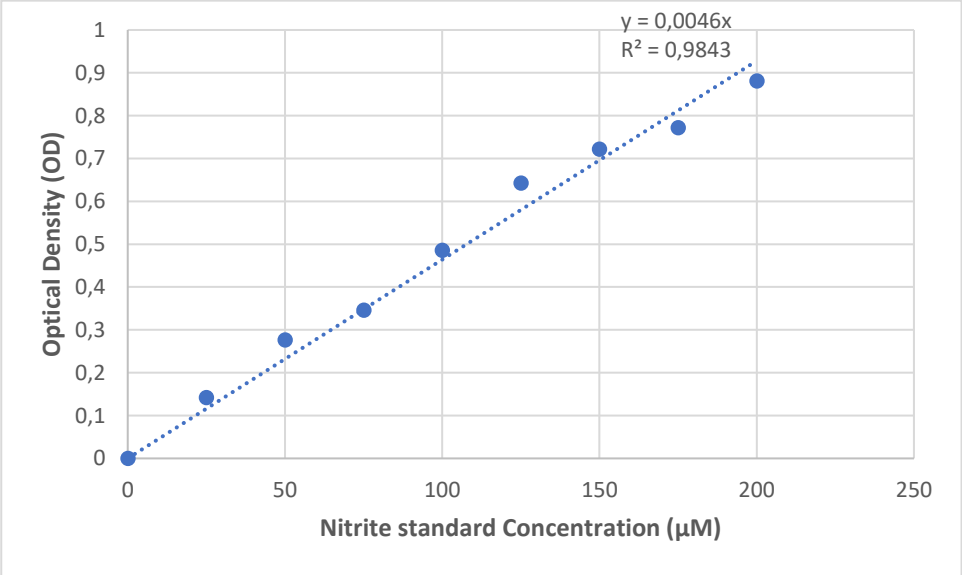

Figure 1: Nitrates and nitrites Standard reference curve used to determine nitrates and nitrites concentration in samples.

APPENDIX D

Table 1: Protein Quantification and Standardisation using Bovine Serum Albumin (BSA).

Protein Standard(mg/ml)	OD1	OD2	Average OD
0	0,069	0,075	0,072
0,2	0,133	0,136	0,1345
0,4	0,188	0,193	0,1905
0,6	0,218	0,219	0,2185
0,8	0,277	0,281	0,279
1	0,274	0,344	0,309

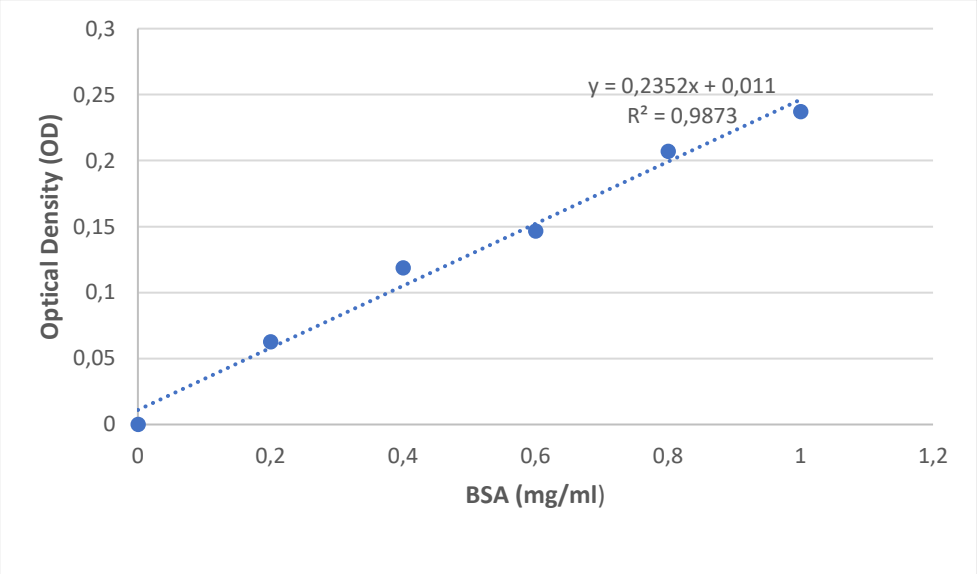

Figure 1: Standard curve using a range of known BSA concentrations. Equation of the straight line was used for determination of sample protein concentrations using the bicinchoninic acid assay.

Table 2: Standardisation of protein samples to 1.5 mg/ml using standard curve of BSA concentrations.

Samples	**Average OD**	**Protein (mg/ml)**	**C2 (mg/ml)**	**V2 (µl)**	**V1 (µl)**
Control		4,987245	1.5	150	45,115088
IC_{20}		2,808248	1.5	150	80,121129
IC_{50}		2,183248	1.5	150	103,057463

APPENDIX E

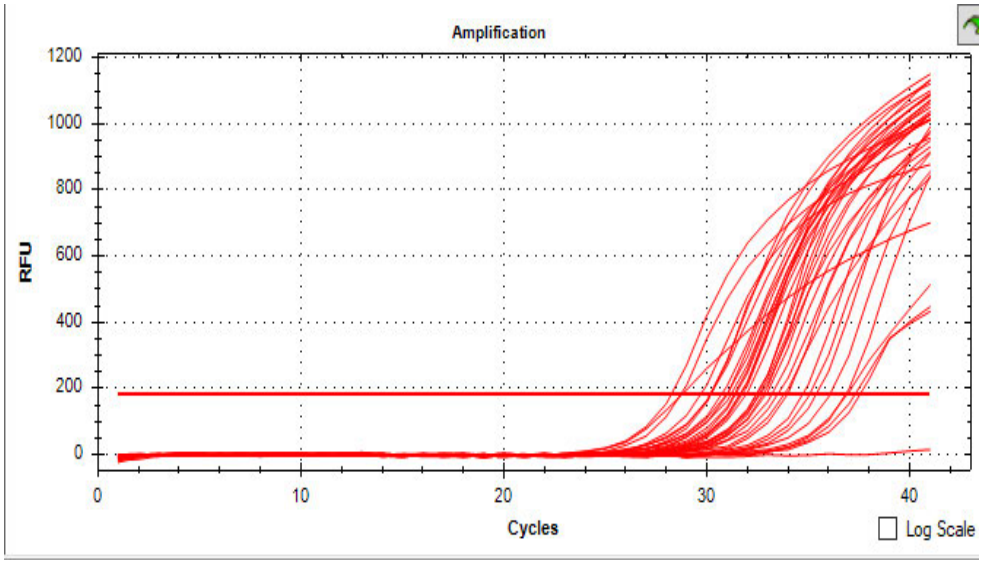

Figure 1: The gene amplification of Nrf2

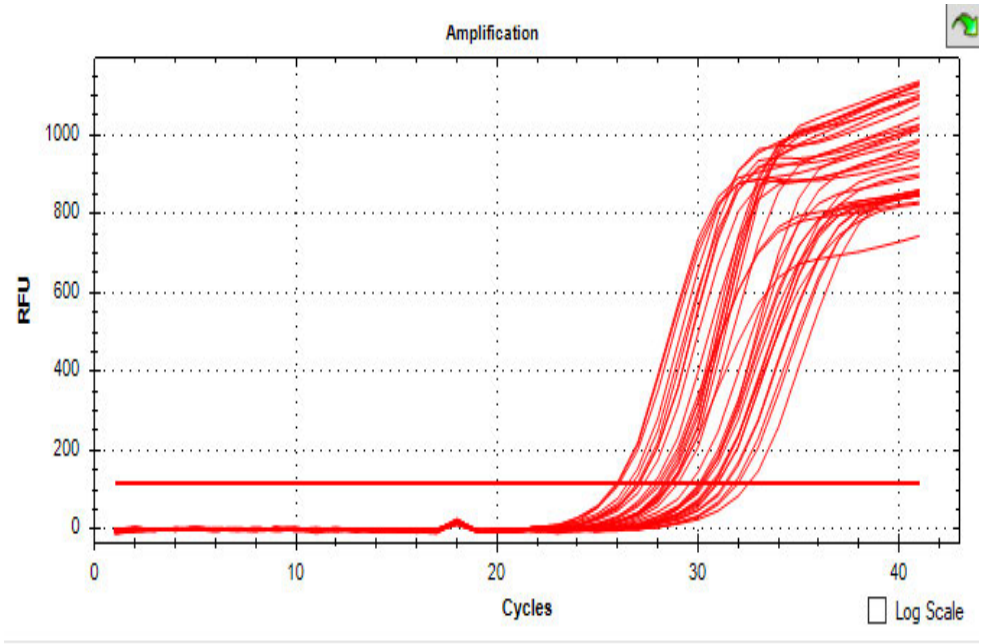

Figure 2: The gene amplification of *p53*

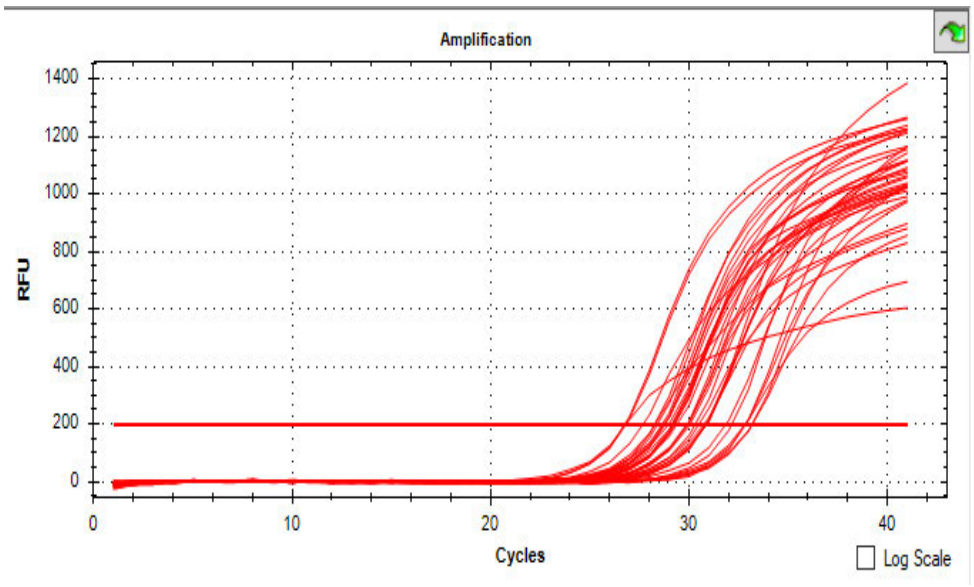

Figure 3: The gene amplification of *NF-κB*

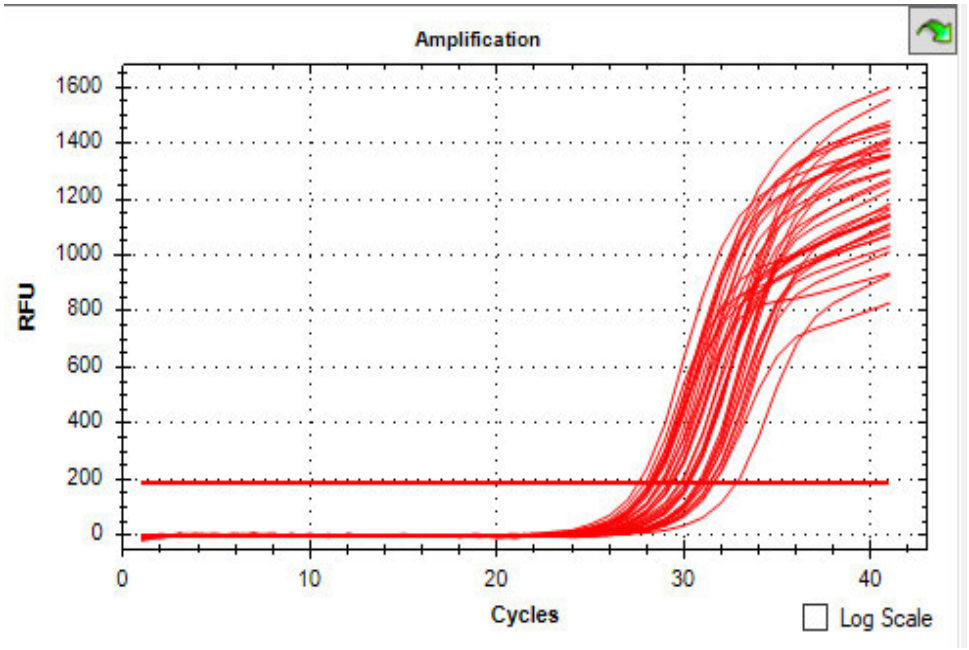

Figure 4: The gene amplification of *NF-κB*

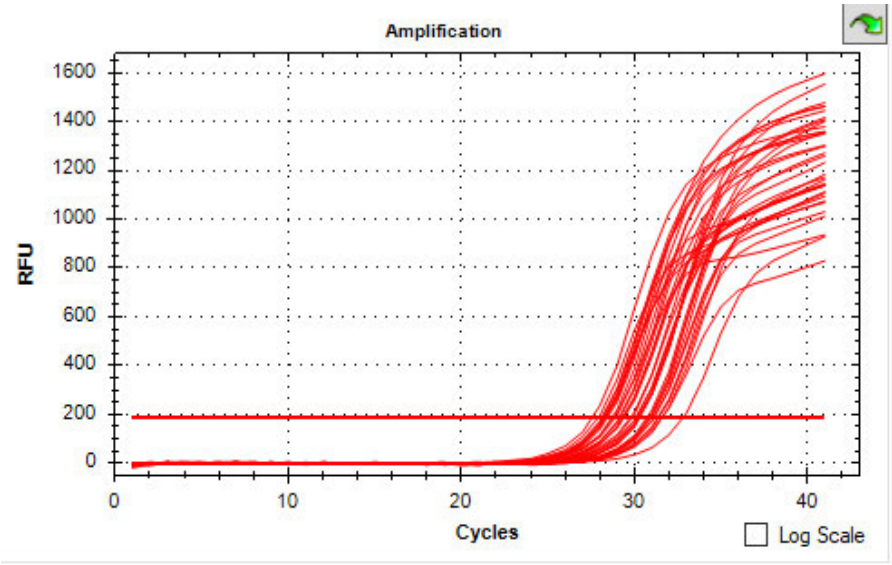

Figure 5: The gene amplification of *GPx*

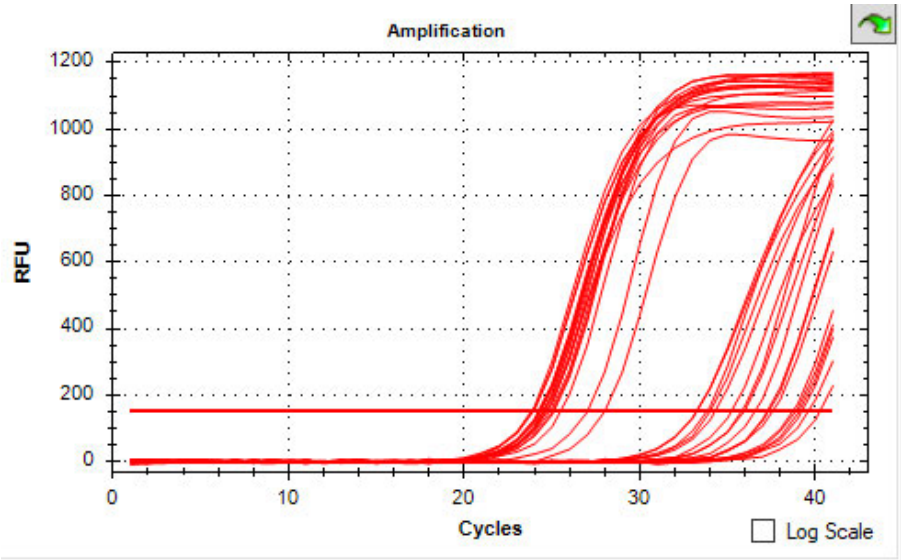

Figure 5: The gene amplification of *OGG1*

.